# Label-free functional imaging of cell viability response to disruptive agents in 3D spheroids using optical coherence tomography

By

Madison G. Woo

Sc.B., Brown University, 2017

Thesis

Submitted in partial fulfillment of the requirements for the
Degree of Master of Science in Biomedical Engineering at Brown University

PROVIDENCE, RHODE ISLAND

MAY 2020

This thesis by Madison G. Woo is accepted in its present form by
the Center of Biomedical Engineering as satisfying the thesis
requirement for the degree of Master of Science.

Date_____ _____

Dr. Jonghwan Lee, Advisor

Recommended to the Graduate Council

Date_____ _____

Dr. Marissa Gray, Reader

Date_____ _____

Dr. Diane Hoffman-Kim, Reader

Approved by the Graduate Council

Date_____ _____

Dr. Marissa Gray, Biomedical Engineering
Master's Program Director

## Acknowledgements

First off, I would like to thank Dr. Jonghwan Lee for providing me with the opportunity to take part in such exciting research and for being an exceptional advisor. I have learned so much over the past year and am deeply grateful for all the experiences and knowledge I have gained and can carry with me after Brown.

To Dr. Diane Hoffman-Kim, thank you for collaborating with our lab, providing guidance on this research, and for being a part of my thesis committee. To Dr. Marissa Gray, thank you for being a supportive advisor throughout my graduate education as well as being a part of my thesis committee.

I would also like to extend my sincerest gratitude to the remainder of the Lee Lab, and especially to a select few. Thank you to Ahbid Zein-Sabatto for not only teaching me how to use the OCT system and preparing my sample gels and assays, but also for your patience and mentorship throughout my incessant questions and trouble-shooting challenges. I'd also like to thank Adrian Bico and Ramisa Fariha for your help and camaraderie, especially during our overnight experiments.

Lastly, I am so appreciative just to have been able to continue my education in an environment where I'm surrounded by such inquisitive and incredibly driven scholars. The research being conducted at Brown continues to inspire me, so even with the small impact my research may have, I am overjoyed to have contributed to a greater effort to help improve people's lives and health through science and research.

# Table of Contents

# List of Figures

# 1. Background

According to the American Cancer Society, there will be approximately 1.76 million new cancer cases in the United States for 2019[1], with a future global burden projected to reach nearly 28 million new cases in 2040[2]. Although an estimate, a rise in the prevalence of risk factors such as smoking and poor diet and exercise habits may increase this number even more. Cancer itself is not a single penetrable disease: it is made up of a diversified plethora of diseases, each arising from genetic variations within a cell and leading to rampant, malignant growth. Not only is cancer characterized by the endless renewal and spread of abnormal cells, but the heterogeneity continues to increase throughout carcinogenesis as greater dysregulation and varied cell populations leads to a myriad of genotypes and phenotypic expressions. This breakdown serves as the biological backdrop to the physical, emotional, and financial toll afflicted on those with cancer. With time, and motivated by a high prevalence and burden, comes the propensity for scientific discovery and technological advancements; however, since President Nixon's announcement of the "war on cancer" in 1971, much is still to be realized about the disease and effective cures. Cancer treatment can take several forms and is often a combination strategy involving chemotherapeutic agents. Since the landmark discovery of methotrexate as the first successful chemotherapy for a solid tumor (treatment of choriocarcinoma) in 1953[3], there are now over 150 Food and Drug Administration (FDA)-approved anticancer drugs[4] that make up the armamentarium of chemotherapy treatment. The increase in drugs available is also reflected in adjuvant chemotherapy treatment with other cancer interventions. Yet despite its extensive use in cancer treatments, the need for effective drugs is still widely relevant with respect to improved patient outcomes and averting resistance.

Traditional drug selection relies on consulting empirical evidence of previous clinical studies and chemotherapy sensitivity and resistance assays (CSRAs) to anticipate which drug

would be most responsive in a particular patient based on their diagnosis, health, and treatment preferences among other factors. Genomic testing and improvements in assay technology have become a prominent focus in cancer research; however, despite the growing tools for improving drug suggestion strategies, further evidence-based methods are necessary in guiding optimal treatments for improved patient outcomes. As an emerging model in cancer research and healthcare overall, precision medicine takes an individualized approach to discern more reliable treatment options. Moreover, the research conducted in genomics and in vitro models has contributed to oncology studies vastly, but still requires further testing prior to clinical application. Upon validation, these improvements in technology could greatly lend to the efficacy of cancer treatment: a refined approach to drug selection rationale enabled by precision medicine must take an integrative approach to combine prior knowledge of cancer vulnerabilities, coupled with static, individual tumor genomic analysis, to functionally test drug synergy and effectiveness using in vitro tumor spheroids.

## 1.1 Potential of precision medicine to fill the gap

Chemotherapy aims to destroy rapidly growing malignant cells in the body through the administration of cytotoxic drugs; however, this combative form of treatment is at the expense of damaging viable cells as well as ensuing detrimental health effects and financial burden without certainty of the outcome. As one of the most common treatments, chemotherapy can be used as a combination therapy of several drugs or alongside other interventions such as surgery or radiology as an adjuvant or neoadjuvant. A review study was conducted in 2004 to investigate the contribution of cytotoxic chemotherapy on adult patient survival for 22 major cancers[5]. Of the total randomized clinical trials that met the study's criteria, only 2.1% attributed a five-year patient survival benefit solely to adjuvant chemotherapy. Although there may be several confounding factors going into a systemic review that cannot be accounted for in such a

heterogenous disease, the core observation still resonates over a decade later with the present reality. As scientific research and clinical efforts continue to trend towards insightful discoveries, still only a select group of patients are receiving the appropriate treatment of anticancer drugs. Many others who have already underwent first-line chemotherapy may be experiencing drug resistance and in dire need of a modified, effective regimen. The widespread use of chemotherapy has undermined the need for a change in candidate drug selection process, and ultimately, effective chemotherapies that improve patient outcomes.

Among the dozens of anticancer drug options, treatment selection is traditionally guided via empiric therapy or assays. CSRAs are conducted in vitro to assess whether tumor cell growth is inhibited when subjected to a drug or panel of drugs. The theoretical utility of CSRAs has led to an aggregate of developed tests used extensively over the past half century to rationalize drug regimen choices. Reviews of the clinical literature to determine the utility of assay-guided treatment in standard oncology practice found insufficient evidence in recommending CSRAs, relative to empiric treatment[6,7,8]. When comparing the percentage of tumor reduction, higher response rates were observed in most assay-guided treatment, but findings were not entirely significant as nine of the 11 studies were not randomized. Furthermore, many first-generation studies rely on retrospective, uncontrolled, or nonrandomized methods and exclusively use traditional anticancer agents. With a lack of substantial evidence providing definitive evaluation of whether testing outcomes may correlate to improved patient outcomes, the clinical limitations underscore an unmet need for a reliable method for cancer treatment selection.

The recent promise of individualized solutions ubiquitous across the healthcare industry has naturally prompted the alignment of precision medicine with the long withstanding gap between prescribed drug regimens and positive outcomes. Precision medicine aims to identify and implement the most effective approach tailored to the patient's biology, environment, and

lifestyle. It would account for person-to-person variability and in practice, standardize the individualization of treatment and prevention strategies. Its intent specific to oncology is to identify the ideal drug regimen that will maximize tumor reduction or eradicate the cancer on an individual patient basis. It has created a buzz amongst the lay press and narratives in the news, and most predominantly amongst the national government. A 2016 government backed initiative of $215 million[9] towards the precision medicine budget has set high expectations for relevant outcomes, with worldwide importance as China is planning to invest the equivalent of nearly $10 billion USD[10] towards the effort. As the body of evidence continues to build for precision medicine and especially the use of genomics in cancer-related studies, it's positioned at becoming the purported cancer treatment tool.

Early successes have acted as drivers in fueling momentum towards cancer research in an effort to fully tap the power of precision oncology. One primary example is imatinib for the treatment of chronic myeloid leukemia[11]. This chemotherapeutic is a tyrosine kinase inhibitor that can work for patients bearing a particular chromosomal translocation. This type of cancer treatment works to hinder tumor growth through interfering with specific mutation-driven abnormal proteins involved in malignant tissue growth. The validation of imatinib evoked the shift in cancer treatment towards a more realized, targeted approach. Further studies of imatinib demonstrated its efficacy in treating gastrointestinal stromal tumors[12]. A formerly intractable cancer, the breakthrough drug discovery reinforced the utility of targeted therapies towards widespread application into other areas of disease. Yet, a study in 2015 found that less than 10% of patients have received mutation-guided therapies that are clinically validated and United States FDA- approved[13]. Continued progress in clinical research is critical to determining genetic targets for treatment while considerable investigation is needed prior to employing precision oncology.

## 1.2 Adoption and limitations of genomic testing-based suggestions

Advances in genomics and bioinformatics have contributed to the next-generation sequencing capabilities used in cancer research. A review of all the cancer clinical trials registered on ClinicalTrials.gov reported an over 5-fold increase from 2005 to 2013 in studies requiring enrollment of either the presence or absence of a genomic alteration[14]. By leveraging baseline sequencing information, genomics aims to establish the initial tumor conditions and relevant mutations. In this approach, drug suggestion is fundamentally based on identifying the somatic mutations dictating tumorigenesis in a patient. With that information, a drug would be recommended to target specific alterations, controlling the malignancy with unprecedented results and ultimately improving patient outcomes.

Such a shift in precision oncology to include genetic biomarkers has reflected the implementation of genomics into a more mutation-centric paradigm[15] for guiding chemotherapy selection. An integral study published in 2002 used gene expression for breast cancer prognosis[16]. A DNA microarray analysis was conducted on primary breast cancer tumors of 117 young patients to establish a predictive gene signature that indicated a poor prognosis profile. Such an approach is still seen today in the routine screening and stratification of patients who present that particular breast cancer gene signature. In the years following the discovery of imatinib and cancer genome sequencing, many papers have been published identifying driver mutations with proposed gene targets for treatment. Some of which have positively identified somatic mutations that were clinically responsive to drug therapy. A notable few include the mutations of EGFR in lung cancer[17], BRAF in melanoma[18], and HER2 in breast cancer[19].

Detecting potentially actionable mutations has propagated a substantial amount of genomic data. In spite of this knowledge and aforementioned success, identifying actionable mutations does not necessarily correlate with efficacious therapies. Amongst prevailing

endorsement, there is a limited body of supporting evidence backing the optimism for genomic testing-guided drug rationale. Despite a remarkable increase in genetic mutation insight, cancer treatment capabilities using genomics has yet to align accordingly.

A major obstacle hindering its use is the impalpable genotype-phenotype relationship. The limited understanding of how genetic alterations manifest into tumor phenotypes is further compounded by its nonlinearity. In other words, different phenotypic expressions can be observed in people with the same mutation[20], and vice versa. Additionally, the initial factors, complex interactions, and evolving architecture of signaling pathways all contribute to the overwhelming cancer picture. As observed in the numerous studies proposing mutations, genome-based therapy methods start with tumor genotyping to establish the initial tumor factors. Despite increasingly identified mutations, objective evidence of clinical improvement by matching chemotherapy based on those mutations is scarce[21]. Simply finding genetic variants in malignant tissue is inadequate at curating a multifactorial cancer system, making it incredibly difficult at its core to address anticancer drug selection exclusively with genomics. Compared to conventional physician's choice, the SHIVA trials (Molecularly targeted therapy based on tumour molecular profiling versus conventional therapy for advanced cancer) found no significant improvement in progression-free survival of cancer patients treated exclusively by a targeted mutation approach[22]. By assessing patient outcome as the primary end point, the study underscores the fundamental purpose behind cancer treatment research, and how genomic-based therapy has yet to come to fruition on.

Additional shortcomings of genomics-based therapy are inherent in its narrow reach. The routine testing priority for driver mutations reduces the scope of prospective clinical trials to a small subset of genes and involves only a few cancer types – approximately 50% of such studies involved either breast, lung or skin cancer[14]. Due to the limited cohort involved in clinical testing,

only a small group of patients may benefit (see [21] for perspective). For the group receiving a targeted therapy, as highlighted in the SHIVA trials, patient outcomes are observed similar at best to traditional regimens. Scientific publications acknowledging these limitations counteract with the need to aggregate genomic data and streamline reporting architecture into a comprehensive database in order to reveal more synergistic insight[23,24]. Seeing as the overarching approach has yet to have a strong bearing on clinical outcomes, even with integrative data analysis, an objective evaluation of genomics-testing based therapy is necessary in determining its legitimacy in routine oncology. For genomic information to significantly improve clinical outcomes of chemotherapy, it may have to be used complementary with other approaches.

### 1.3 Functional testing may enhance the clinical utility of precision medicine

Given the immense expectations for precision medicine , it is critical to determine what opportunities for improvement are available to effectively change the projection of targeted therapies towards effective anticancer drug suggestion. As initiatives continue to push genomics research in hopes of clinically relevant results, a shift in approach is necessitated in order to expect more appealing outcomes. Functional testing alongside next-generation genome sequencing capabilities may support this critical change. In general, functional testing in oncology involves any investigation with malignancies that have a perturbation incorporated to gain insight into guiding rationale drug selection by comparing the results before and after treatment.

Functional methods do not rely on genetic indicators as a basis for testing criteria, allowing for a greater proportion of patient inclusion and overall diversity in patient profiles that can be studied. An investigation published in 2018 found that 769 vulnerabilities were detected using RNA interference amongst 501 various cell lines, of which less than seven percent had a predictive genetic biomarker[25]. Since functional testing does not rely on prior knowledge of the

underlying mutation mechanism or drug-target interaction, use of this approach would complement genetic sequencing when vulnerability characterization is not yet clear. A multi-diagnostic approach (**Fig. 1**) demonstrated that genomic shortcomings in predictive value could be overcome with functional testing of patient-derived tumor organoids using high-throughput drug screening[26]. In this study, functional testing-based drug recommendations using patient-derived xenograft models outperformed standard chemotherapy suggestions. The drug sensitivities ex vivo could also be related back to the genomic information in a reverse analysis approach for additional understanding.

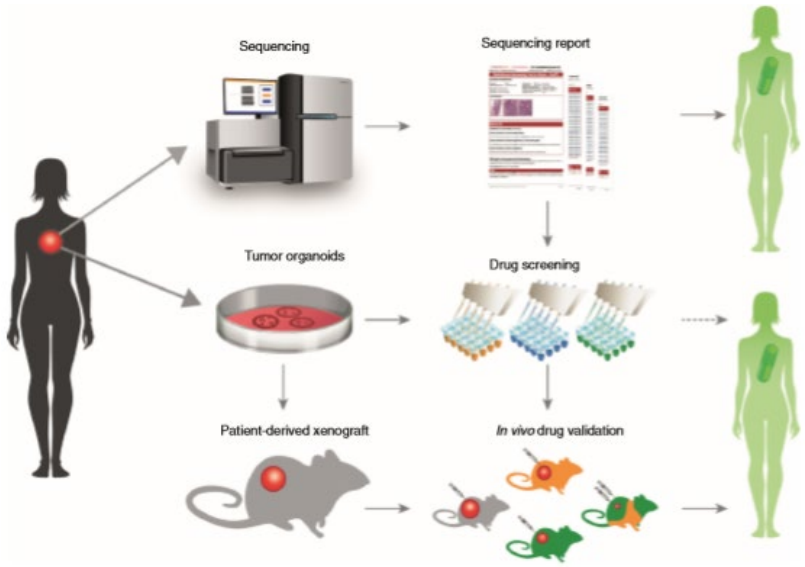


**Figure 1**. A multi-diagnostic approach to precision medicine for cancer treatment selection. Patient tumor tissue biopsies are used for sequencing to generate genomic profile reports. Patient derived organoids (PDOs) are used to perform in vitro functional testing of drugs and can also be used in patient-derived xenografts (PDXs) to validate drug effectiveness in an animal model. The genomic profile, functional testing and in vivo animal validation can be used collectively to guide iterative drug screens from initial candidates to the appropriate drug and dose (or combination regimen) for chemotherapy drug treatment. Reprinted from Pauli et al., 2017.

Coupled with genomics, enhancement of individualized drug suggestions may become more possible with the inclusion of functional testing into the precision medicine paradigm. As

more chemotherapy agents are being added to the armamentarium of anticancer drugs, increased drug combinations for treatment are being introduced, as well as unknown or unintended side-effects. Being able to functionally test these iterative, multi-drug regimens and observe end points that directly reflect perturbation outcomes is a distinct advantage that further enhances utility for a patient-specific objective.

Especially when combined with the genetic testing, functional testing overcomes the analysis of sheerly the initial condition by introducing a perturbation to generate desirable results that otherwise would be challenging to tease out from static analysis of initial conditions. To address a rare and aggressive form of cancer, a study implemented a computational-experimental platform to identify synergistic drug combinations tailored to individual cancer patients[27]. The platform made use of baseline genomic profiles for in silico prioritization of 24 out 23,653 possible pairwise drug combinations. Of the 24 drug combinations, 42% experimentally showed synergy in patient-derived ex vivo samples. By using a functional approach coupled with genome data, the study successfully predicted distinct synergistic drug combinations for varying resistance patterns in each of the patient samples. Granted the study does not report on drug efficacy or address patient outcomes, it still provides a framework of how validating this method could be proven beneficial in clinical settings.

Despite extensive use in scientific research, functional testing has yet to be incorporated into routine practice. Direct evidence is needed in order to confirm its clinical utility and validate its benefit to patients. Recent advances in functional screening technology including methods for tumor manipulation could help overcome the limitations of traditional CSRAs. Once further testing has been conducted to validate these next-generation developments, their employment in functional testing could assist in driving predictive, translational results.

## 1.4 Advancements in tumor culturing methods

The omnipresence of two-dimensional (2D) in vitro cell cultures in research has solidified its use as a valuable tool for scientific testing and discovery. Although breakthroughs have been made using 2D cultures, the model is still far from ideal in augmenting tissue environments. By building upon pre-existing technology, advancements in tumor cultivation methods such as three-dimensional (3D) tissue models have been especially compelling for cancer research initiatives. A traditional 2D cell culture relies on adherence to a flat disk to physically support the planar growth of cells, whereas 3D cultures allow for multi-directional cell growth and interaction. Considerable differences are apparent between 2D and 3D cultures including cell-cell interactions, cellular mechanisms, and nutrient access[28] which can have a substantial impact on the modeling accuracy of the samples.

Despite its frequent use in the past to screen anticancer drugs with CSRAs, there are several considerations when determining the relevance of 2D cultures. Conventional 2D cell lines can exhibit uncontrolled growth profiles that are both genotypically and phenotypically different from the original tumor. These deviations can cause changes in mutation and expression profile, induce rapid growth, increase drug sensitivity**Error! Bookmark not defined.** and alter other factors essential in functional tumor models. This could explain the considerable clinical testing failures of novel agents when 2D preclinical studies demonstrated otherwise. An inability to recapitulate the heterogeneity of the complex in vivo tumor environment with a 2D sample has made the exploration of improved culture models all the more imperative.

Fortunately, some of these limitations can now be overcome with advancements in 3D cell culture technology. and most prospectively through spheroids and patient-derived organoids (PDOs). An increasing amount of evidence has shown that 3D cultures exhibit tumor origin features and functional cell line characteristics that more closely align with the derived tumor

sample. Such attributes include cell differentiation, histoarchitecture, and heterogeneity[29], and cellular interactions, hypoxia, and drug interactions[30], respectively. More studies are validating 3D spheroids as an improvement upon 2D cultures and their ability to express morphological, biomechanical, genotypic, and other cellular features as observed in the origin tumor[31,32]. Since these multicellular spheroids are being governed by factors akin to what is observed in vivo, they present a more reliable model of heterogeneity and drug-resistance for high-throughput studies and critical assessment of bioactivity.

In order to determine the most rational drug selection on an interpatient basis, these spheroids can also be cultured from patient-explanted, organ-specific cells to form organoids. In a study using tumor biopsies from patients with metastatic colorectal cancer, PDOs were developed to test the culturing feasibility and genetic diversity of organoids relative to the original tumor sample[30]. Of the 14 PDO cultures, 10 of the cases were deemed successful. In comparing nearly 2,000 cancer related genes, 90% of the somatic mutations were shared between the organoid and patient biopsy. Together, these results suggest the translational capabilities of PDOs as an innovative tool for drug screening. Aside from colorectal cancer, a recently published article noted 11 other established organoid models for cancer[33], underscoring the versatility of PDOs in modeling various tumor subtypes with diverse mutations. Along with conclusive studies establishing characteristic alikeness between PDOs and the original patient tumor, these organoids may be able to address targeted treatment effectiveness by providing a robust, functional screening platform for drug responsiveness ex vivo. Vlachogiannis et al. took it a step further to compare drug screening results of PDOs with existing approaches[34]. Profiling of PDO genotypes and phenotypes confirmed high correspondence between the organoid and patient-derived tumor. Molecular profiling was also conducted and matched to drug screening results, suggesting the use of PDOs in finding tumor vulnerabilities for treatment suggestion.

As PDOs progressively become more utilized, it is critical to validate and establish methods for standardizing 3D tumor models; however, there are still several limitations that need to be addressed. Data reproducibility with spheroids is in question as the integrity of results from these 3D models is most ensured only when the cell culturing system is intensively controlled and monitored to dissociate any kind of bias from the study. Parameters such as spheroid volume and shape must be closely supervised as their variability within and across studies could affect the reproducibility of results[30,35,36]. A lack of immune cell interaction, vasculature, and hypoxia as observed in tumor microenvironments is not fully acknowledged in organoid models, requiring further progress in 3D models in order to accurately capture the features of malignant tissue. Another practical consideration is the time it takes for full maturation of organoid cultures. It can take weeks of in vitro culturing to acquire successful spheroids which in a time-dependent disease progression may not be practical in guiding treatment decision when a tumor is in its most aggressive form. Based on recent advances in 3D culture technology, challenges are being addressed and overcome, which will greatly contribute to precision medicine and its impact on anticancer drug therapy suggestion.

## 1.5 Employing 3D functional testing curbed by limitations in traditional assays

While validation of PDO models continues to favor 3D models over 2D cultures, the execution of traditional assays with 3D cultures will not be feasible or may yield unreliable results, at best. Assays such as fluorescence imaging, immunohistochemistry, and live/dead monitor physiological function using foreign reagents to stain tissue and determine cellular viability. The use of CSRAs has been optimized for 2D cultures and proven auspicious in gaining knowledge of anticancer treatment. For example, a study comparing outcomes of patients treated with a human tumor cloning assay (HTCA)-guided drug choice versus clinician's choice reported a higher in vivo response rate to drugs in assay-guided treatments i.e. 28% versus 11%[37].

However, for patients with a refractory form of the disease, there was no statistically significant difference in overall survival between the two treatment groups. The study did not validate improved patient outcomes despite the enhanced in vivo response rate and noted a potential patient selection bias. The limitations of the traditional assay and 2D culture used in this study may be overcome with the implementation of more relevant 3D cultures and functional testing approaches, which could also aid in more robust results.

In detail, traditional assays inherently rely on the addition of foreign stains to a 2D or fixed sample for viability assessment. Many limitations stem from trying to incorporate these labeling agents into 3D cultures, and the labels themselves. The addition of reagents to cell cultures often necessitates a single end point measurement of viability due to the introduction of a foreign, often toxic substance into the sample. Evaluation of viability from an end point measurement can yield meaningful data; however, it is incapable of paired tracking of longitudinal effects or repeated exposures pertinent in understanding an extended drug response profile.

In comparison to 2D cultures, 3D models can be subjected to penetration constraints when trying to use them in traditional assays. Drug penetration is a major component of drug testing in spheroids especially when necrotic regions and gradients are present and can impact drug resistance[38], making it imperative to assess the entirety of the spheroid as well as the core. Likewise, assays that rely on staining intuitively encounter complications when applying labeling agents to a 3D model as the reagent may not readily penetrate the core as it would with a monolayer of cells. Likewise, some traditional assays require the culture to be agitated and broken up in order for stain uptake, disallowing for regional spheroid analysis.

Spheroid cultures also present limitations in traditional assays that rely on cell count as it is impossible to assess the number of cells in a 3D sample over time. For example, the trypan blue

(TB) assay uses a dye exclusion test to distinguish stained dead cells from live cells as a means of assessing viability. A study examining the reproducibility in cell count using TB with both 2D and 3D cultures found an approximate 20% variability when measuring cell population density between two operators[39]. Additionally, the heterogeneity in cell types coupled with variable cell populations and spheroid shape introduces additional uncertainty that cannot be accounted for in traditional assays. Although heterogeneity makes for a more sophisticated in vitro model, the different cell types observed in 3D models makes it all the more difficult to ascertain cell type counts. Methods for quantifying proliferation rates often involve foreign stains and fluorescence to track specific cells, making it problematic to definitively measure multiple cell types in coculture spheroids.

Altogether, CSRAs present significant limitations in employing 3D cultures as it is challenging to observe longitudinal cell viability, assess the entire spheroid (including the core), and control for cell count and inter-spheroid variability. The limitations of conventional assays and their reliance on labeling reagents highlights the current lack in nondestructive methods for high-throughput evaluation of chemotherapy drugs using 3D cultures.

## 2. Introduction

Optical coherence tomography (OCT) makes use of the coherent property of light to image a sample in cross section which collectively generates a 3D voxel without the use of reagents or staining molecules. The non-invasive technology is capable of label-free, longitudinal, and volumetric imaging through biophotonics and light-matter interaction. Similar to sound waves in ultrasound, light directed at biological tissue is absorbed, reflected, transmitted, or scattered. These interactions can produce a natural imaging contrast between the different cellular components as well as the extracellular matrix (ECM) and surrounding tissue architecture within

a sample. Its clinical relevance has been established through OCT's dominance in ophthalmology as a main diagnostic tool for retinal disease and glaucoma. The structures and layers of the retina can be observed due to the reflectivity of the region, allowing for high-resolution subsurface images that were not obtainable to such a degree prior to the introduction of OCT.

Other areas of clinical development using OCT have been seen in dermatology, cardiology, gastroenterology, and more recently, oncology. Clinical applications such as visualization of stent deployment using intravascular imaging during cardiac procedures[40] and gastrointestinal endoscopies for the detection of Barrett's esophagus[41] are just two examples of the intraoperative and in vivo potential of OCT. Its label-free capabilities also place OCT imaging within the purview of primary technical goals that align with the *NIH's Precision Medicine Initiative* (which has since been changed to the *All of Us Research Program* since the initial announcement in 2015). The optical imaging platform offers a means of cellular viability assessment with high-throughput and longitudinal potential which could aid in optimized anticancer drug selection. As OCT continues to emerge as a useful imaging modality, its demonstrated congruity with functional and longitudinal assessment could serve as a vital avenue towards precision medicine in chemotherapy drug selection.

## 2.1 Biophotonics and the OCT system

OCT focuses on scattering events and largely depends on physical size and shape of the objects encountered within a media as opposed to chemical composition or other aspects that typically govern other optical imaging techniques. A basic OCT system is based on a Michelson-type interferometer to observe the scattering interactions in biological tissue that in turn can produce high-resolution images. Light is emitted from a source beam wherein it is split by a beam splitter and directed towards a reference mirror arm and tissue sample arm. The light directed along the reference arm will be reflected off a mirror and sent to a detector. The light sent to the

sample arm will interact with the tissue sample before being redirected to the detector. A schematic of the setup and light paths are shown in **Figure 2** below. The interference pattern of the recombined light paths is observed at the detector as an OCT signal that is representative of the optical properties of the sample. By varying the position of the reference arm, light can scan throughout the depth of the sample allowing for 3D imaging. In order to localize such small-scale samples, broadband light is used for its finite coherence length allowing for interference fringe data to be reconstructed into a sharp image.

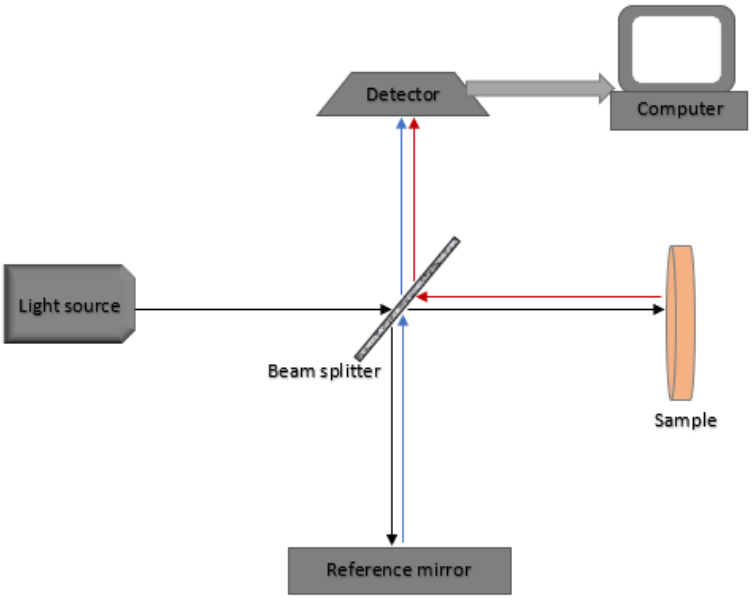


**Figure 2**. A simplified OCT system based on a Michelson interferometer. Its main components are labeled and light paths are represented by arrows. The incident light, reflected sample arm, and reflected reference arm light paths are illustrated by the black, red, and blue colored arrows, respectively.

OCT scanning parameters are all built upon a single light beam. An A-scan is a 1D array along a single axis. Multiple A-scans of varying depths along an axis collectively form a B-scan. Taking all the B-scan slices together then form a volumetric scan, or voxel. The optical system generally has a micrometer-scale lateral and axial resolution, a maximum imaging depth of 1-2 mm[42], and high temporal resolution[43]. With label-free soft tissue contrast, OCT technology offers a highly relevant imaging modality for 3D cultures with promising features that make its clinical

relevance all the more appealing. As innovation continues to broaden OCT's applications, cell-by-cell tracking of drug response longitudinally and high-throughput screening of dose-response curves are two very pertinent techniques being developed.

OCT imaging can be differentiated into several different types such as time-domain OCT (TD-OCT) and spectral domain OCT (SD-OCT). TD-OCT is a traditional approach that uses a mechanically moving reference arm to obtain the axial reflectivity pattern that reaches the detector. Conversely, SD-OCT has a fixed reference arm and uses a spectrometer instead of a detector. The interference pattern from the combined light paths undergoes a Fourier transformation, generating depth-resolved images. A review comparing SD-OCT to TD-OCT has shown SD-OCT to have superior sensitivity, decreased acquisition time, and greater axial resolution; however, spectral domain imaging has a noticeable signal drop-off with scanning depth[44]. Both systems have commercially available technology that is widely used and continues to serve as gold standard instruments for retinal imaging. After transforming retinal disease management from just observations to greater understanding and more reliable diagnosis, there is gaining popularity in OCT as researchers seek to employ the same technology in other clinical disease applications.

## 2.2 Leveraging scattering and motility

Spanning a vast array of modalities, medical imaging is utilized in all aspects of tumor detection and management and therefore plays a significant role in clinical decision making. Primary medical imaging systems–x-ray, computed tomography (CT), magnetic resonance imaging (MRI), ultrasound, and optical imaging–aim to address tissue and cellular morphology, metabolism, and other functional and structural components of the sample being imaged. With a shift in cancer treatment towards targeted therapies specific to the patient's tumor, an imaging platform for label-free, high-through testing is all the more salient.

Electromagnetic radiation interacting with tissue is the basis of most medical imaging systems, but not all. Imaging technology can vary based on the physical mechanism of contrast, resolution, and imaging depth and contrast. At the higher end of the frequency spectrum, x-ray systems including CT scans have been used in skeletal surveys as well as for imaging other structures and abnormalities within the body. Despite a low cost and high temporal resolution and imaging depth relative to other modalities, x-ray technology is generally limited in observing a tumor due to its poor soft tissue contrast and inability to functionally image cellular activity. Unlike x-rays, MRI and ultrasound do not use radiation, and instead are based upon principles of magnetic dipoles and sound waves for contrast, respectively. The clinical use of MRI was first examined in breast cancer over 35 years ago[45], and has since been positioned alongside ultrasound and mammography as MRI technology continues to improve and evolve to meet clinical needs[46]. With similar millimeter spatial resolutions, MRI and ultrasound are capable of imaging beyond anatomical structures to examine physiology, but do not have the sensitivity needed to obtain biochemical and biological information. Increased development of exogenous tracers continues to shape medical imaging capabilities, showing promising results for improved molecular imaging but aren't necessarily advantageous enhancements to in vitro diagnostics where label-free, non-destructive imaging is more apropos.

In the middle of the frequency spectrum are optical imaging systems such as OCT. The physical principle behind OCT not only allows for high-resolution soft tissue contrast without the use of labeling agents, but it also serves as the basis for viability-linked changes in optical properties of a sample. The different components that make up tissue such as the ECM, cells, and the intracellular organelles, all contribute to the back-scattering light profile that reaches the detector. The nucleus and mitochondria are noted specifically for being strong scatters[47] and likewise, have been repeatedly shown to exhibit a scattering profile characteristic of living cells[48].

A study using ovarian tumor spheroids attributed strong light scattering to densely packed cells with large nuclei present[49].

The cell death process can follow multiple pathways with distinctive morphological changes that differ from the architecture of live cell architecture[50]. Two extensively researched pathways include apoptosis and necrosis. Apoptosis is characterized by a cell-programmed suicide process wherein the cell undergoes shrinkage, chromatin condensation, and blebbing leading to fragmentation into apoptotic bodies. In contrast, necrotic death results from an increased cell volume due to cytoplasmic and organelle swelling, causing the cell to rupture and leak intracellular components. The morphological transformation undergone during the cell death cascade could cause changes in organelle distribution within a tissue sample, intuitively leading to changes in the optical scattering profile, potentially with distinction between apoptosis and necrosis.

In addition to the optical scattering profile, intracellular motility (ICM) has also been investigated as an indication of cellular viability. One of the earlier studies exploring volumetric imaging of the anticancer drug response qualitatively reported a decrease in ICM over time post-drug administration, demonstrating that the drugs ability to suppress cellular activity may be observed optically[51]. A different study using chemotherapeutic agents to assess viability observed a more erratic speckle intensity 24 hours after treatment compared to the untreated group, attributing the significant increase in ICM to the morphological processes associated with apoptosis[52]. Further compounding the complexity, cells undergoing necrosis have been shown to exhibit a decreased light scattering profile[53]. Although readily observable changes in scattering and motility have been noted and linked to cell death morphology and subsequent viability, most have focused primarily on qualitative reports. These studies generally adhere to healthy, live cells having a greater scattering effect and more noise relative to dead cells, but not all. Inconsistencies

in signal patterns and conflicting results across studies may be attributed to varying stages of the cell death process and require further investigation.

Other studies have employed various OCT-based metrics in an effort to better differentiate between changes in cell state. These studies deployed techniques including speckle decorrelation rate, phase fluctuations, spheroid geometry, and attenuation coefficients to assess cell viability[54,55,56,57]. The noted research warrants varied approaches and novel findings, but results are often confined by relative measurements and limited in their experimental contributions outside of the individual studies because of system-specific dependencies. Additionally, qualitative assessments and non-standardized metrics put repeatability and consistency in question, especially when there can be considerable variation in spheroid tissue development[30]. Nevertheless, changes in viability can be observed with OCT imaging through the intrinsic optical contrast in light interacting with biological tissue. When limitations in standard unit metrics and result reproducibility are addressed, the application of OCT imaging for cellular viability will be even closer to enhancing functional testing in chemotherapy drug suggestion.

## 2.3 Rising innovations in cell viability assessment

As researchers continue to improve upon existing optical technology and test methods, innovation in OCT imaging has led to a need to better understand how changes in the OCT signal are associated with specific cell mechanisms underlying viability. Longitudinal assessment enabled by label-free OCT imaging has the potential to guide cellular viability studies of assessing repeat, combination regimen, and time-dependent dosing effects in predicting drug responsiveness. All of which to be carried out through a functional testing approach in guiding anticancer drug suggestion. Conventional assays that use a tissue biopsy or culture inherently rely on fixation and staining for observing cellular viability and are unable to assess drug responses over time, neglecting valuable time-varying response feedback. In order to make this valuable

insight accessible, several promising research objectives are aiming to improve upon present barriers in OCT imaging to better validate viability mechanisms and report on changes through standard-unit metrics.

Reporting standard-unit measurements coupled with multi-metric analysis allows for a more comprehensive, technically sound OCT imaging platform for assessing viability within and across studies. Furthermore, cell death mechanisms can be more thoroughly investigated by exploring changes in multiple parameters as opposed to a single relative-change measurement. This is particularly important for studying the effects of different drugs believed to trigger a specific cell death cascade.

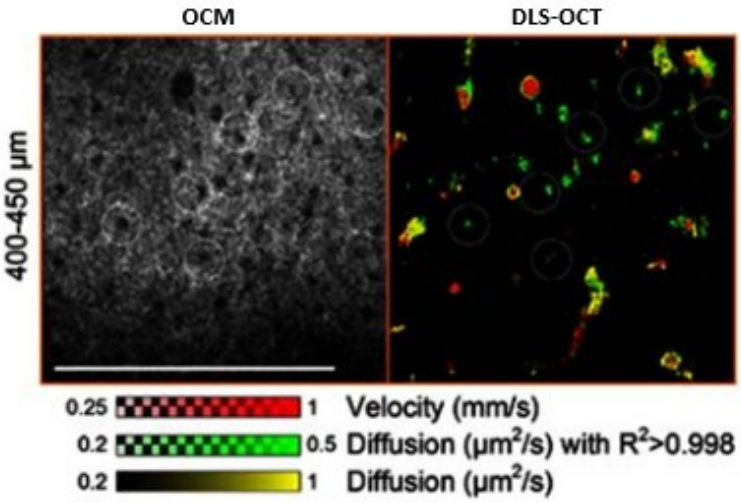


**Figure 3.** Imaging the diffusion coefficient using DLS-OCT. Higher diffusion coefficients (indicated in green) were highly correlated with neuronal cell bodies as a of result greater ICM in comparison to the less dynamic surrounding tissue. Encircled dark spots are used to spatially correlate cell bodies in the optical coherence microscopy image (OCM) to the DLS-OCT image. Adapted from Lee et al., 2013.

One such approach has been developed to overcome the aforementioned challenges – dynamic light scattering OCT (DLS-OCT). DLS-OCT captures particle flow and velocity within a voxel through volumetric mapping of the diffusion coefficient. The recent innovation by Lee et al. accurately measures the diffusion coefficient within a voxel as well as other relevant metrics[58].

This capability is especially critical to imaging biological systems where variable particle dynamics are contained within small-scale samples such as a spheroid. An initial feasibility study used SD-OCT to image the rodent brain in vivo while simultaneously mapping blood flow velocity and ICM (**Fig. 3**)[59]. Regions of high diffusion were attributed to the ICM of organelles within the neuronal somas, where nuclei identification was postulated as areas of less motility.

## 2.4 Unanswered questions guide study objectives

Optical imaging studies are investigating various metrics to better understand chemotoxicity and changes in viability but have been met with inconsistent findings. Relative-change metrics, longitudinal assessment, and various disruptive agents have been used in the absence of a clear understanding of the mechanisms that link between cellular viability and optical metrics. Although ideal, a mutually exclusive relationship between a specific drug and cell-line interaction inducing a certain change in OCT signal is not probable. Instead, a multi-metric approach to quantify cellular dynamics could be used in conjunction with drug selectivity and assays that can clarify underlying processes.

A recent study by Yang et al. looked at changes in two ICM-specific metrics using cell-lines from two breast cancer subtypes[60]. Both cell lines were exposed to two different inhibitors, demonstrating a cell-line specific metric output that was dependent on the inhibiting agent's mechanism. A similar study observed the effects of toxic agents on the intracellular kinetic energy and cross-sectional area of organoids, noting significant time- and toxicant-dependent changes in viability-linked metrics[61]. Despite these informative studies, there's still no definitive consensus on viability-based signal changes. Therefore, a systematic drug choice paired with a particular tumor cell line approach is needed to more aptly elicit a particular cellular process that could be further understood with an end point assay. In this way, a network of viability

manipulations (i.e. disruptive drugs or agents) could be coupled with a targeted cellular response that would in turn alter OCT metrics in a more anticipatory way.

By choosing disruptive agents with minimally targeted cell processes and "confirmatory" viability assays, the drug–cell death mechanism–OCT signal output relationship will be most linear and better understood, given the vast interactions possible. Likewise, study objectives were established based on this functional testing paradigm. A preliminary investigation using HepG2 spheroids treated with varying concentration of ethanol was conducted to establish the feasibility of our OCT system for high-throughput functional testing, and to guide future studies. Since the byproducts of ethanol metabolism contribute to tissue damage, it was used to ensure cell death.

Following this initial study, neurospheroids were used with two different metabolism inhibiting agents to further investigate viability-linked changes in OCT signal. The Warburg effect[62] was taken into consideration for the secondary study as metabolic plasticity is characteristic of cancer cells in order to meet the high energy demands of rapid proliferation. In order to modulate energy production and thus cell viability, two different metabolic inhibitors were chosen to target ATP synthesis—oligomycin A and 2-deoxy-d-glucose (2-DG) to selectively disrupt mitochondrial respiration and glycolysis, respectively. Longitudinal, multi-metric tracking of investigational OCT measurements was used to establish a better picture of the biological backdrop to OCT signal changes, as explained in the next section. A live/dead and ATP assay were used in parallel to further probe end point viability. Acknowledging that using the same cell line or drug between the two studies could have aided in more comparative analysis between the two, different cell line and drugs were used as a result of changes in lab research direction, available resources, and research timetables.

## 2.5 Investigational OCT metrics

To address unanswered questions, several key OCT metrics are being investigated and include the spheroid geometry, intensity, decorrelation, attenuation coefficient, and diffusion coefficient, among others. The present thesis focuses on four metric groups: spheroid geometry, intensity, decorrelation, and normalized decorrelation. Each group produces several sub-metrics, so the total number of metrics that were tracked as part of the neurospheroid cell viability study was 555, as listed in **Table 1**. Individual metrics are explained in detail in the following sections.

**Table 1**. Metric groups tracked as part of the thesis include spheroid geometry, intensity, decorrelation, and normalized decorrelation, and are subdivided into several more metrics as listed. The abbreviations w, s, b, and c refer to the whole spheroid, shell, body, and core, respectively. The t or b listed before a w, s, b, or c refers to the top or bottom of half of the spheroid, respectively.

| Metric | Region | Total |
|---|---|---|
| **Spheroid Geometry** | | |
| Volume | w, s, b, c, tw, ts, tb, tc, bw, bs, bb, bc | 12 |
| Area | w | 1 |
| Surface area-to-volume ratio (SATVR) | w | 1 |
| Surface Roughness (SR) | w | 1 |
| **Intensity** | | |
| Intensity | w, s, b, c, tw, ts, tb, tc, bw, bs, bb, bc | 12 |
| Intensity Coefficient of Variation (CoV) | w, s, b, c, tw, ts, tb, tc, bw, bs, bb, bc | 12 |
| **Decorrelation** | | |
| Decorrelation | w, s, b, c, tw, ts, tb, tc, bw, bs, bb, bc | 36* |
| Decorrelation CoV | w, s, b, c, tw, ts, tb, tc, bw, bs, bb, bc | 36* |
| **Normalized Decorrelation, ND** | | |
| Universal fitting-based ND | w, s, b, c, tw, ts, tb, tc, bw, bs, bb, bc | 36* |
| Universal fitting-based ND CoV | w, s, b, c, tw, ts, tb, tc, bw, bs, bb, bc | 36* |
| Fitting coefficient D1-based ND | w, s, b, c, tw, ts, tb, tc, bw, bs, bb, bc | 36* |
| Fitting coefficient D1-based ND CoV | w, s, b, c, tw, ts, tb, tc, bw, bs, bb, bc | 36* |
| Fitting coefficient D2-based ND | w, s, b, c, tw, ts, tb, tc, bw, bs, bb, bc | 36* |
| Fitting coefficient D2-based ND CoV | w, s, b, c, tw, ts, tb, tc, bw, bs, bb, bc | 36* |
| Autocorrelation-based ND, Decay | w, s, b, c, tw, ts, tb, tc, bw, bs, bb, bc | 12 |
| Autocorrelation-based ND, Decay CoV | w, s, b, c, tw, ts, tb, tc, bw, bs, bb, bc | 12 |
| Autocorrelation-based ND, DopplerAbs | w, s, b, c, tw, ts, tb, tc, bw, bs, bb, bc | 12 |
| Autocorrelation-based ND, DopplerAbs CoV | w, s, b, c, tw, ts, tb, tc, bw, bs, bb, bc | 12 |
| Autocorrelation-based ND, Doppler | w, s, b, c, tw, ts, tb, tc, bw, bs, bb, bc | 12 |
| Autocorrelation-based ND, Doppler CoV | w, s, b, c, tw, ts, tb, tc, bw, bs, bb, bc | 12 |
| Autocorrelation-based ND, ComplexShift | w, s, b, c, tw, ts, tb, tc, bw, bs, bb, bc | 12 |
| Autocorrelation-based ND, ComplexShift CoV | w, s, b, c, tw, ts, tb, tc, bw, bs, bb, bc | 12 |
| Autocorrelation-based ND, $2^{nd}$ Decay | w, s, b, c, tw, ts, tb, tc, bw, bs, bb, bc | 12 |
| Autocorrelation-based ND, $2^{nd}$ Decay CoV | w, s, b, c, tw, ts, tb, tc, bw, bs, bb, bc | 12 |
| Autocorrelation-based ND, $2^{nd}$ Shift | w, s, b, c, tw, ts, tb, tc, bw, bs, bb, bc | 12 |
| Autocorrelation-based ND, $2^{nd}$ Shift CoV | w, s, b, c, tw, ts, tb, tc, bw, bs, bb, bc | 12 |

* Applied to a B-scan time delay of 10, 20 and 30 ms

### 2.5.1 Spheroid geometry

The physical geometry of a spheroid (e.g. diameter, surface area, volume) can be used to indirectly assess viability changes in tumor spheroid growth. As tissue undergoes cell death processes as a result of some sort of viability manipulation, changes in the spheroid volume could morphologically change, resulting in a less spherically intact shape with fragmentation and dispersion. Cells that are thriving and continuing to proliferate may result in a positive change in volume with a more intact shape. Additionally, spheroid's surface area-to-volume ratio (SATVR) can be used to quantify overall changes in morphology over time. Due to inherent spheroid heterogeneity and aspherical shapes, individual dimensions are not used for reliable assessment. However, by using a ratio or clearly defined adjusted ratio, the variance between samples can be reduced. Additionally, surface roughness (SR) can be calculated as a metric independent of spheroid size.

### 2.5.2 Intensity

Intensity can be defined as the amount of light energy transferred perpendicular to a given area. Within an OCT system, this means quantifying the backscattered light that reaches the detector/spectrometer. Light rays stray from the initial straight-line path as they propagate through and cross between different mediums by scattering, absorbing, reflecting, and transmitting. Areas of higher reflectivity and backscattered light will have greater intensity, in turn appearing as brighter spots on an OCT image and vice versa. The intensity will attenuate at increasing imaging depths and areas of absorption. Photons are also influenced by the size and distribution of particles – densely packed media will result in more interactions and increased scattering events, resulting in a greater potential for reflectivity and thus higher intensity. Cell death via apoptosis is one such example where nuclear condensation and cell shrinkage could

increase the density and backscattered light, resulting in a higher intensity region on the OCT image. The swelling and membrane rupturing characteristic of necrosis would decrease intensity as organelles are displaced throughout a larger volume.

### 2.5.3 Attenuation coefficient

The attenuation coefficient describes the fraction of light that gets transmitted per unit thickness through a medium relative to the full incident ray. The metric considers the total radiant flux loss from both absorption and scattering events (i.e. the absorption coefficient and scattering coefficient) and is reported in standard units of the inverse meter, or $m^{-1}$. The metric shows how quickly light intensity reduces as it passes through tissue; however, at increasing imaging depths, the attenuation coefficient may also be influenced by the confocal effect. Quantitative analysis of the attenuation coefficient can be used to characterize and differentiate tissue. For example, a higher coefficient would signify increased absorption or densely packed regions whereas a lower coefficient would result from relatively unobstructed transmittance through a sample.

### 2.5.4 Decorrelation

Decorrelation measures the OCT speckle signal that results from sensitivity to movement within a biological sample. As successive slices are acquired during the imaging process, the minute change in time between the B-scans can capture the dynamics or lack thereof within the tissue. For instance, a static particle or cell that does not exhibit any motion would have no decorrelation such as the sphere in **Figure 4** with no direction arrow. Conversely, particles that actively move between and within the OCT voxel or resolution volume will all contribute to the overall decorrelation.

Changes in ICM as a result of viability can also impact the speckle signal. Cells undergo various structural transformations throughout the cell death process, resulting in physical motion

and displacement of cellular components in the extracellular space. The early stages of apoptosis are one such example of how particle movement during the fragmentation of cytoplasm and nuclei can increase decorrelation. The cell death processes that drive decorrelation changes may differ with those driving intensity changes. The OCT decorrelation signal, however, tends to be larger in nature when the intensity is higher. The decorrelation is typically defined by a difference between two complex-valued OCT signals; thus, even when a particle movement generates an identical Doppler shift in the phase of the OCT signal, the difference in the complex plane becomes larger when the magnitudes of the OCT signal is larger.

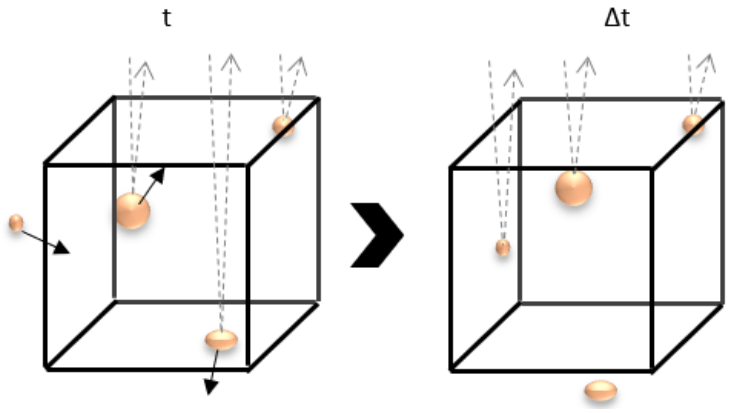


**Figure 4.** A schematic of particle dynamics. Particle movement can occur within and across a voxel during small changes in time, resulting in decorrelation. The spheres represent particles, the black arrows signify the direction it is moving in, and grey dashed lines represent the reflected light off the particles at locations within the voxel for a given time and change in time (Δt).

### 2.5.5 Normalized decorrelation

Due to the nature of OCT, decorrelation tends to inherently increase when intensity increases, and in a seemingly non-linear manner. Therefore, any observed changes in decorrelation may result from the coupling effect of these two metrics, and not necessarily a result of just motility. In order to extract normalized decorrelation, two different approaches are being investigated since the novelty of this metric makes the optimal method unknown at this

point. As such, a detailed explanation of the associated math and how they relate to the conclusiveness of the results cannot be provided until further investigation warrants complete understanding of the metric's relationship to the dynamics in a sample.

The first approach is based on the observed saturation of decorrelation as a function of intensity and is modeled using sigmoid functions. Specifically, this fitting-based approach uses a hyperbolic tangent function with an offset to reflect when the intensity-decorrelation curve does not cross the origin. The function is fitted to data that involves all spheroids and is applied to a set reference timepoint in a "universal fitting-based normalized decorrelation". As another fitting-based approach, two different test decorrelation values were used in a hyperbolic tangent fitting of individual spheroids and are assessed as fitting coefficients D1 and D2.

The other approach provides normalized decorrelation based on the autocorrelation function to understand if and how the decay, $2^{nd}$ decay, complex shift, $2^{nd}$ shift, doppler, and absolute doppler align with the different dynamics being captured. These measurements theoretically quantify different random and translational components of movement being captured in the sample. Of note, these two approaches were investigated in the main cell viability study using neurospheroids whereas a logarithmic fitting-based approach was used in the feasibility study with HepG2 spheroids. However, since the formerly discussed approaches have since replaced the logarithmic strategy, the latter methodology will not be explained in further detail.

### 2.5.6 Diffusion coefficient

The diffusion coefficient is a constant proportion of flux to the concentration gradient. In OCT imaging, this can be subdivided into the particles that are static, flowing or diffusing, and entering/exiting the volumetric field of view (FOV) that collectively make up the overall diffusion coefficient. Expressed in terms of area per time, or $m^2s^{-1}$, the diffusion coefficient can convey the cellular dynamics within a tissue. Intuitively, viable cells will exhibit a higher

diffusion coefficient relative to its ambient surrounding because of ICM. Necrotic cells will have a diffusion coefficient similar to the extracellular space as they are no longer viable and wholly contained within a membrane. Both decorrelation and diffusion coefficient can measure ICM, but by differing means. Decorrelation is recorded with relative-change metrics whereas the diffusion coefficient uses DLS-OCT to facilitate a rapid scanning protocol to quantify a standard unit metric.

# 3. Feasibility Study using HepG2 Spheroids Treated with Ethanol

## 3.1 Abstract

To explore the feasibility that our OCT system is capable of longitudinal, multi-metric assessment of signal changes associated with cellular viability, HepG2 spheroids were subjected to varying doses of ethanol and changes in investigational metrics were tracked longitudinally. Significant time-dependent changes were observed in the OCT signal at varying doses of ethanol. In particular, there was a decrease in intensity at lower concentrations, whereas the higher ethanol concentration resulted in a significant increase in intensity, decorrelation, and normalized decorrelation. Further investigation into cell morphology throughout apoptosis and necrosis, along with more selective drug and cell line choices will help aid in elucidating a more anticipated OCT signal response that could more aptly be caused by fluctuations in cellular viability.

## 3.2 Methods

### 3.2.1 HepG2 spheroid culturing

Human hepatocellular carcinoma HepG2 cells (ATCC, Manassas, VA) were used to culture human liver tumor spheroids. HepG2 cells were trypsinized and seeded onto an agarose

microgel at a density of 2000 cells per well. Microgels were made by pouring molten agarose over a MicroTissues mold with 96, 400 uM diameter pegs (#24-96 Small Spheroids, MicroTissues, Providence, RI). HepG2 spheroids cultured in the microgels were maintained in Eagle's Minimum Essential Medium (MT1009CV, Corning, Corning, NY) supplemented with 10% fetal bovine serum (Thermo Fisher Scientific, Waltham, MA) and 1% penicillin-streptomycin (MP Biomedicals, Santa Ana, CA). Spheroids were incubated at 37°C in a 5% $CO_2$ environment. HepG2 spheroids were provided by the Morgan Lab (Brown University, Providence, RI) and cultured by Joshua Manning (Morgan Lab, Brown University).

### 3.2.2 Ethanol exposure

Spheroids were treated 72 hours after seeding with either 10%, 20%, or 30% ethanol (2.2 mM, 4.3 mM, and 6.5 mM, respectively), or media (sham group) in order to induce changes in cellular viability. 200-proof ethanol was premixed into a vial of medium to create stock solutions of the appropriate concentrations. At the start of the experiment, medium was carefully pipetted out of the well and replaced with the appropriate solution concentration and medium. Caution was taken to slowly pipette the treatment solution into the well and not directly over the gel to avoid dislodging spheroids or flipping the gel. Data was acquired at 10, 20, 30 and 40 minutes after drug treatment.

### 3.2.3 OCT imaging system and data acquisition

The SD-OCT system from Thorlabs (Thorlabs, Newton, NJ, USA) was used for 3D volumetric imaging in this study. The system uses a superluminescent diode light source to provide a bandwidth of 170 nm, a central wavelength of 1310 nm, and an axial resolution of 3.5 μm. An LSM03 lens (Thorlabs, Newton, NJ, USA) optimized for scanning systems was used in all experiments.

The plate was set on top of a heating pad that was placed on the platform base of the OCT system. The heating pad controlled the temperature so that the sample did not have to be moved to a separate incubator in between data acquisition time points. One of the plate wells was filled with water and a thermistor was placed inside. The pad was maintained at a constant temperature of approximately 45°C, resulting in a body (water well) temperature of approximately 36°C. With this setup, the LSM03 lens is pointed downwards towards the plate and aligned with the microgel being imaged, creating a "top down" imaging scheme. The SD-OCT system, generator, and other related hardware and wires are placed on or affixed to an optical table that is supported by legs which use pressurized air to isolate environmental vibrations (Thorlabs, Newton, NJ). This helps to isolate vibrations during image acquisition, minimizing the amount of noise and distortions associated with such movements.

The ThorImageOCT Software (Thorlabs, Newton, NJ) was used to visualize and focus the sample in real-time prior to data acquisition. After manual positioning of the SD-OCT directly underneath the gel of interest, the electronic z-axis translator (Thorlabs, Newton, NJ) was used to adjust the focal plane along the optical axis until the sample came into view and its surface aligned with the focal plane. The reference mirror distance was adjusted by turning the dial on the SD-OCT. When necessary, these steps were repeated until the image was optimally focused in 2D. A 3D scan was then recorded and cross-sectional XY slices were scrolled through to ensure all the desired, whole spheroids are cropped into the voxel in the subsequent data acquisition.

The custom Lee Lab app written in LabVIEW (National Instruments, Austin, TX, USA) was used for OCT volume data acquisition. Parameters were set prior to acquisition and are dependent upon the scanning protocol used. The preset "Angiogram" protocol was used to obtain the intensity and decorrelation data. The FOV was set to 512 x 512 x 1024 pixels in the x, y, z direction, respectively, which translates to an imaging volume of approximately 5 x 5 x 3 mm

being captured when the default objective lens LSM03 (Thorlabs) was used. The number of repeating B-scans was set to two with a time delay of approximately 6.43 ms between scans in order to measure the decorrelation. Raw data was acquired for each of the ethanol concentrations right after administration as well as 10, 20, 30 and 40 minutes after treatment. For these experiments, data was previously acquired by two former lab members - Itzel Aponte and Bruno Felalaga (Lee Lab, Brown University).

### 3.2.4 OCT data processing

Reconstruction of the OCT data and image analysis for investigational OCT metrics was carried out using Lee Lab codes in MATLAB (MathWorks, Natick, MA, USA). Reconstructing the raw data involved cropping the volume, determining optimal dispersion compensation, and averaging the volumes. Using the reconstructed data, generally 10-15 spheroids from the middle of each microgel were chosen for longitudinal analysis. The ellipsoidal region of interest (ROI) was traced around the outline of each spheroid using max intensity and max decorrelation plots in three different coordinate system views. The intensity and decorrelation are averaged for the whole ROI and account for the entire spheroid. The mean intensity, decorrelation, and normalized decorrelation values were calculated for each of the selected spheroids at every time point. The normalized decorrelation was also calculated to decouple intensity from decorrelation as it may skew metric results.

### 3.2.5 Statistical analysis

Investigational OCT metric results are presented as means ± standard error at each time point of the voxels within the chosen spheroids' ROIs' for three to seven biological replicates at each concentration (generally 10-15 spheroids per gel). The distribution of the data did not pass normality according to the Shapiro-Wilk Test nor did it demonstrate homogeneity of variance

according to Levene's Test, so Mood's median test was chosen for statistical analysis given its conservative nature. Additionally, a Bonferroni correction was used to account for the 3 comparisons, resulting in an adjustment of one third alpha. Longitudinal differences between time points were assessed using Mood's median test to compare each subsequent time point to the initial 10-minute measurement. Statistical analysis was used to assess if there were any significant time-dependent changes in metric measurements at each of the treatment concentrations.

## 3.3 Results

### 3.3.1 Results of metrics

A results table of the metrics with the mean, standard error (SE), and statistical significance for each concentration and time point can be found in **Table 2**.

**Table 2.** Results summary of intensity, decorrelation, and normalized decorrelation at 0%, 10%, 20%, and 30% ethanol. An adjustment of ⅓ alpha was used per Bonferroni's correction: *p≤ 0.0167.

| | | | Intensity | | | | Decorrelation | | | | Normalized Decorrelation | | | |
|---|---|---|---|---|---|---|---|---|---|---|---|---|---|---|
| | | | 10 min | 20 min | 30 min | 40 min | 10 min | 20 min | 30 min | 40 min | 10 min | 20 min | 30 min | 40 min |
| Ethanol | 0% | Mean | 0.134 | 0.118 | 0.104 | 0.094 | 0.149 | 0.155 | 0.137 | 0.135 | 0.999 | 1.323 | 0.948 | 0.944 |
| | | SE | 0.006 | 0.006 | 0.005 | 0.005 | 0.006 | 0.004 | 0.006 | 0.006 | 0.001 | 0.085 | 0.007 | 0.007 |
| | | P-value | | | * | * | | | | * | | | * | * |
| | 10% | Mean | 0.399 | 0.348 | 0.299 | 0.277 | 0.154 | 0.144 | 0.146 | 0.145 | 1.008 | 0.974 | 0.994 | 0.993 |
| | | SE | 0.038 | 0.032 | 0.026 | 0.024 | 0.006 | 0.004 | 0.004 | 0.004 | 0.002 | 0.011 | 0.013 | 0.015 |
| | | P-value | | | | | | | | | | * | | * |
| | 20% | Mean | 0.099 | 0.085 | 0.084 | 0.084 | 0.144 | 0.147 | 0.149 | 0.158 | 1.005 | 1.027 | 1.045 | 1.103 |
| | | SE | 0.005 | 0.004 | 0.003 | 0.003 | 0.004 | 0.005 | 0.006 | 0.007 | 0.002 | 0.013 | 0.022 | 0.033 |
| | | P-value | | * | | | | | | | | | | |
| | 30% | Mean | 0.098 | 0.104 | 0.111 | 0.137 | 0.146 | 0.154 | 0.155 | 0.179 | 1.009 | 1.069 | 1.067 | 1.216 |
| | | SE | 0.006 | 0.005 | 0.005 | 0.009 | 0.024 | 0.025 | 0.025 | 0.029 | 0.003 | 0.011 | 0.022 | 0.038 |
| | | P-value | | | | * | | | | * | | * | | * |

Since there were 21 experiments that contributed to the overall metric results, a visual summary table was created to highlight general tends in the individual biological replicates, collectively (**Table 3**). The experiments were overlaid into a single table where arrows and colors were used to signify significant changes in intensity, decorrelation, and normalized decorrelation. Of note, this was simply used as a research tool to see macro-level patterns and not meant to statistically

capture the data. Thorough statistical analysis and its interpretation are described in the following sections.

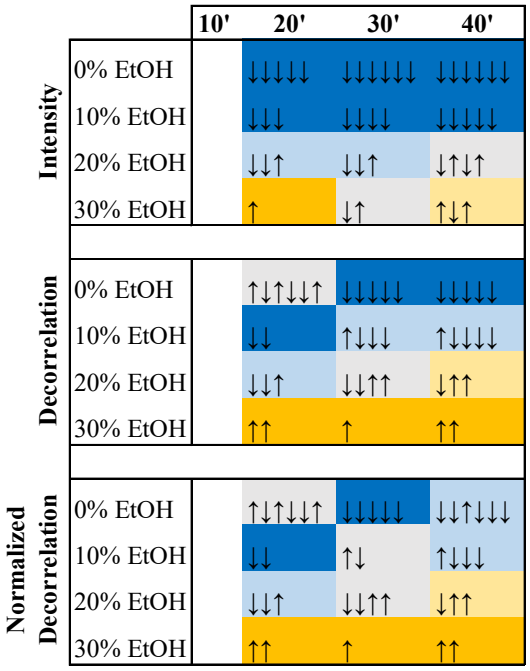


**Table 3.** Visual summary table of individual biological replicate outcomes. An arrow represents a statistically significant increase or decrease in intensity, decorrelation, or normalized decorrelation from one of the 21 analyses, and relative to the 10-minute value. A shade of blue, orange, or grey cell represents an overall decrease, increase, or split results, respectively. Note: used as a research tool, see following sections for thorough statistical analysis.

### 3.3.2 Intensity decreases at lower concentrations of ethanol

The effects of varying concentrations of ethanol treatment were tracked longitudinally from 10 to 40 minutes post-drug administration. The OCT intensity signal was plotted as a function of time for ethanol concentrations of 0% (7 replicates, total number of spheroids ns = 89), 10% ( 6 replicates, total ns = 74), 20% (5 replicates, total ns = 58), and 30% (3 replicates, ns = 37) (**Fig. 5**). Intensity consistently decreased from 10 minutes to 40 minutes for both 0% and 10% ethanol concentrations, with a significant decrease at 20 minutes and 30 minutes in the sham group. A modest yet significant decrease was also observed for 30% ethanol at 20 minutes.

A plot of the relative change in intensity clearly displayed the overall concentration-dependent change in intensity over time (**Fig. 5**). When looking at the results of the microgels independently (**Table 3**), the individual experiments showed a consistent decrease in intensity at

10% ethanol which aligns with the overall decrease in intensity at lower concentrations and within the sham group. Additionally, the signal became more irregular at 20% ethanol with greater fluctuations in the intensity signal over time.

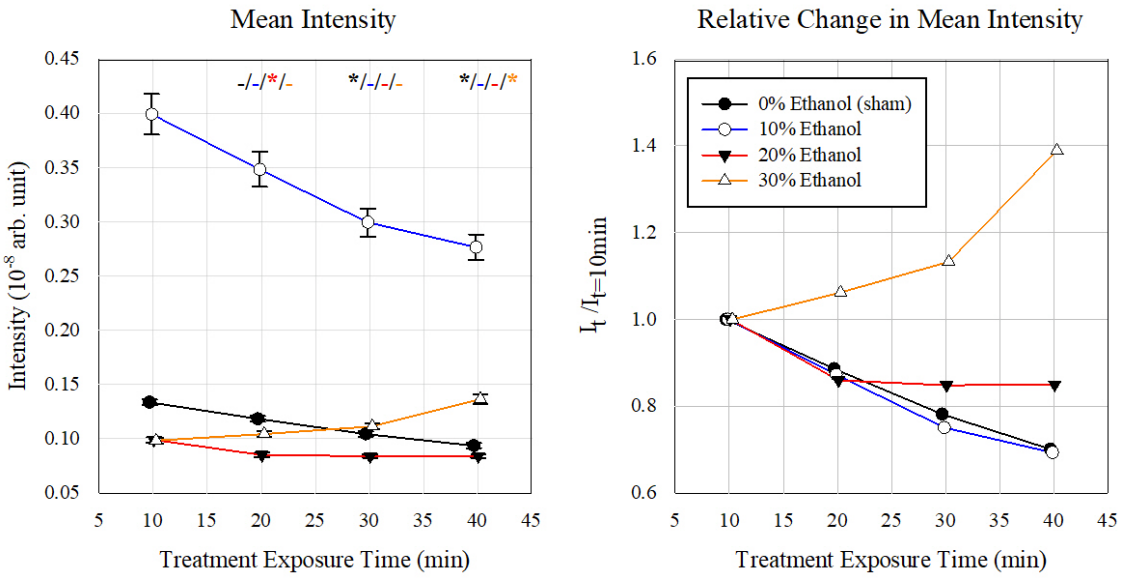


**Figure 5.** Mean and relative change in OCT intensity signal over time for all four concentrations of ethanol. *p≤0.0167.

### 3.3.3 Increase in intensity and decorrelation at highest concentration of ethanol

An increase in backscattered light was observed at the highest concentration of ethanol. At 30% ethanol, the intensity significantly increased at 40 minutes (**Fig. 5**). Decorrelation was more aberrant than the intensity signal; however, an increase was still observed for 30% ethanol between 10 minutes and 40 minutes (**Fig. 6**). A plot of the relative change in mean decorrelation clearly shows the significant increase in intensity at 30% ethanol concentration from 10 to 40 minutes.

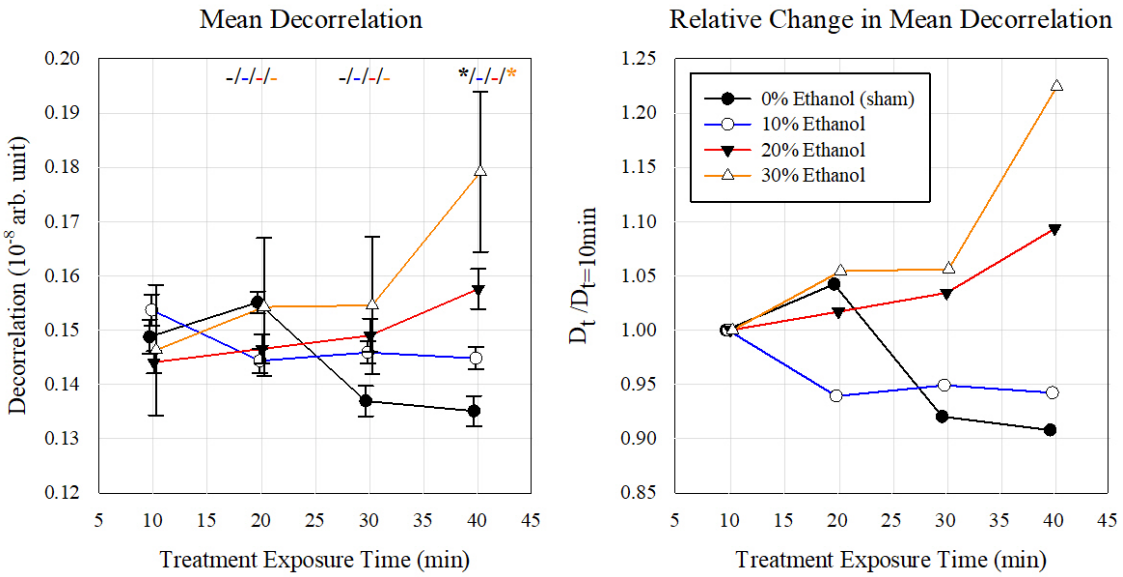


**Figure 6.** Mean and relative change in OCT speckle signal over time for all four concentrations of ethanol. *p≤0.0167.

### 3.3.4 Normalized decorrelation

After decoupling decorrelation from intensity, an increase in speckle signal was still observed for higher concentrations ethanol. There was a significant increase in normalized decorrelation for 30% ethanol at 20- and 40-minutes post-treatment exposure (**Fig. 7**).

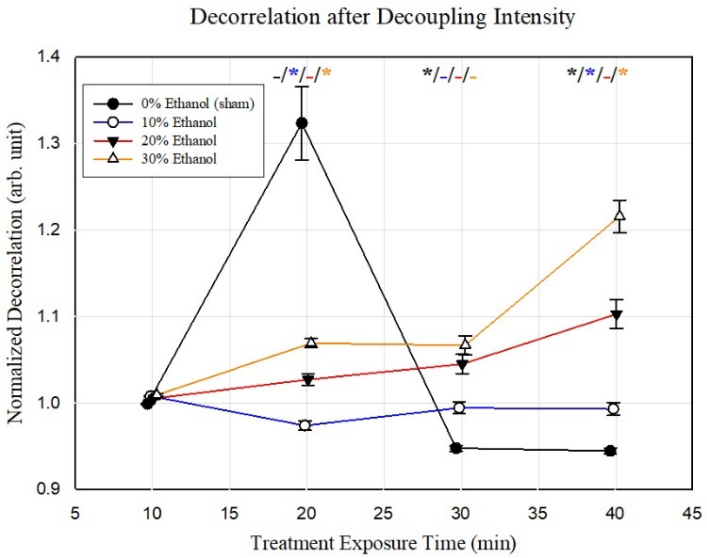


**Figure 7.** Normalized decorrelation for all four concentrations of ethanol over time. *p≤0.0167.

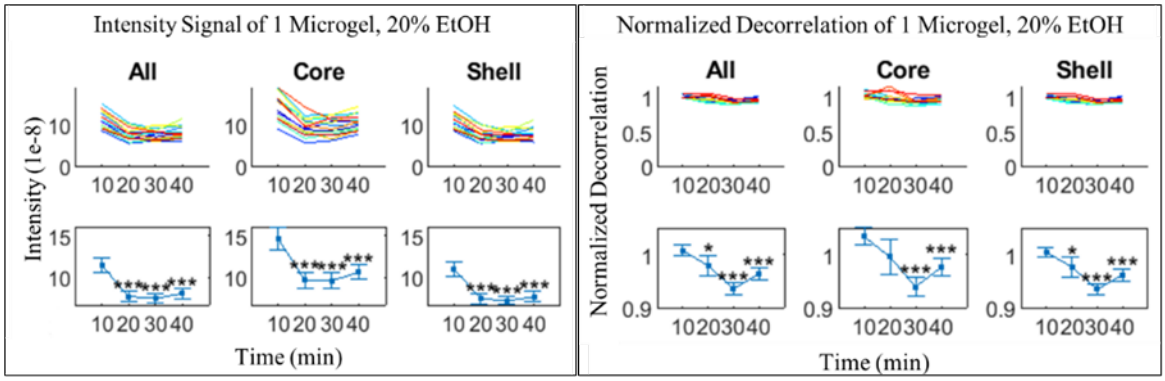


**Figure 8.** An example of U-shaped changes in the normalized decorrelation. This figure presents change in intensity (left) and normalized decorrelation (right) over time for 15 spheroids treated with 20% ethanol. The top row shows the values of all the spheroids and the bottom row is the mean value at each time point of all 15 spheroids.

Interestingly, some of the microgels presented a more U-shaped plot in which the normalized decorrelation would decrease from 20 to 30 min, followed by an increase in signal from 30 to 40min (**Fig. 8**).

### 3.4 Discussion

OCT uses the inherent differences in optical properties within biological tissue to act as a natural imaging contrast. Ethanol has been shown to disrupt the physical structure of cell membranes by disturbing the phospholipid bilayer, resulting in increased membrane fluidity[63]. Similarly, high levels of ethanol can solubilize membranes and denature proteins which contributes directly to the death of these cells[64]. The manifestation of these effects were observed in HepG2 spheroids subjected to varying concentrations of ethanol and tracked longitudinally using OCT metrics. Both dose- and time-dependent metric changes were observed, supporting the feasibility of our SD-OCT system to detect changes in cellular viability. However, discerning how intensity and decorrelation are associated with changes in viability warrants further

discussion of potential underlying biological mechanisms, as well as areas for continued development and future study designs.

At lower concentrations of ethanol, the intensity signal generally decreased over time whereas an increase in intensity was observed at the highest concentrations. This would align with what Castilla et al. reported in primary cultures of human and rat hepatocytes i.e. parameters associated with apoptosis and necrosis were altered dose-dependently after 24-hour ethanol exposure (0-10mM)[65]. Another study used fluorescence microscopy to conclude that there was an increase in apoptosis concomitant with a lower decree of necrosis 24 hours after ethanol treatment[66]. Combined, these studies suggest ethanol elicits dose-dependent changes in viability which can differentially trigger apoptotic and necrotic cell death pathways. This may correspond to the varying OCT signal changes observed in this study.

A decrease in intensity at lower concentrations may be attributed to several possible reasons. Most fundamentally, since the intensity decrease was predominantly observed in the 0% and 10% treatment groups, these cells may not have undergone the disruptive cell death process yet within the 40-minute imaging window. Another possible explanation is that acute treatment with low-dose ethanol has been shown to have a protective effect against necrosis via a reduction of reactive oxygen species (ROS) and basal lipid peroxidation[67,68]. In either case, viability-linked changes in intensity would be marginal relative to the control given cell death processes had not yet commenced or cytoprotective effects were induced.

The significant increase in intensity at the highest concentration of ethanol may be a signal of the cell death process underway. Parameters associated with apoptosis have been shown to increase with increasing concentrations of ethanol, while a higher concentration caused a sharp increase in LDH (an indicator of necrosis) in hepatocytes[65]. Cell shrinkage and chromatin condensation are characteristic of apoptosis and would thus increase the OCT intensity signal as

cells and their components replicate a more densely packed scattering media prior to the formation of apoptotic bodies. As cells undergo necrosis, swelling of the endoplasmic reticulum and mitochondria would result in more larger scatterers that could increase the light reflected back to the sensor.

Cell damage via peroxidation of membranes may have also contributed to the intensity signal. Cultured rat hepatocytes exhibited an increase in malondialdehyde (MDA, an index of lipid peroxidation) at higher concentrations of ethanol relative to the control. This may correspond to the increase in optical scattering as the byproducts of lipid peroxidation play an important role in apoptosis and stimulating the cascade of apoptotic death processes[68]. Therefore, an increase in intensity may be a response to the initiation of apoptosis and its effects on optical scattering prior to fully completed cell death. Another possible mechanism contributing to increased intensity is cell damage via acetaldehyde accumulation. In short,

In targeting ICM as an indicator of cellular viability, decorrelation and normalized decorrelation were measured. The significant increase in intensity and decorrelation at 30% ethanol may be attributed to how these two metrics are coupled together but may also be from an increase in intracellular movement and morphological changes during cell death. An increase in decorrelation may be caused by particle movement as organelles and cytoplasm fragment during apoptosis or leak out during necrosis; however, further investigation and assays would be critical in discerning what stage of injury the cells are at and when. An increase in normalized decorrelation reinforces the increase in speckle signal at stronger concentrations of ethanol.

A pivot in the normalized decorrelation plot as observed in **Figure 8** may signify where substantial cell death takes place (approximately 30 minutes post-treatment) i.e. fragmentation or leakage followed by dispersion of intracellular components, resulting in increased motility being measured. For that same microgel, a significant decrease in intensity was observed at 20 minutes,

followed by a minimal change in signal value from 20 to 40 minutes. This would make sense if a majority of the cell death process is carried out by 20 minutes, wherein an increase in ICM would signify the cellular components being fragmented or leaked into the extracellular matrix for apoptosis or necrosis, respectively. In turn, this would justify a plateau in intensity signal as the apoptotic bodies and leaked components become incorporated into and indistinguishable from the extracellular space.

The significant decrease in intensity in the sham treatment group was a major limitation in this feasibility study. Several reasons can be discussed, including spheroid shift, temperature controls, evaporation of media, and the natural tendencies of the HepG2 cell line. Upon further examination, the spheroids shifting outside of the focal plane may have greatly contributed to the decrease in intensity. The focal plane was set right before the first data point was acquired and was not re-focused for the remainder of the 40-minute imaging protocol such that at each 10-minute mark, images were captured without prior adjustment of the z translator. This was confirmed by the reports exported from the Lee Lab reconstruction code. Approximated “peak z values” at each time point compared to the initial time point for all the experiments resulted in an average change of 9, 19, and 26 voxels for 20, 30, and 40 minutes, respectively. This means the spheroids moved in the z-direction approximately 30, 60, and 90 μm, a non-negligible change that may justify the decreased intensity as spheroids shift out of the focal plane. Of note, even in a "healthy" control culture, there can still be some cell damage associated with a low level of necrotic death[65].

Also, there were several observations made during the data reconstruction and image analysis portion that may have weakened the rigorousness of data. Firstly, gaps in the experiment data disallowed for a more complete examination of each ethanol concentration. Second, poorly cropped voxels and blurry images made it difficult to trace spheroid ROIs. Spheroid shape

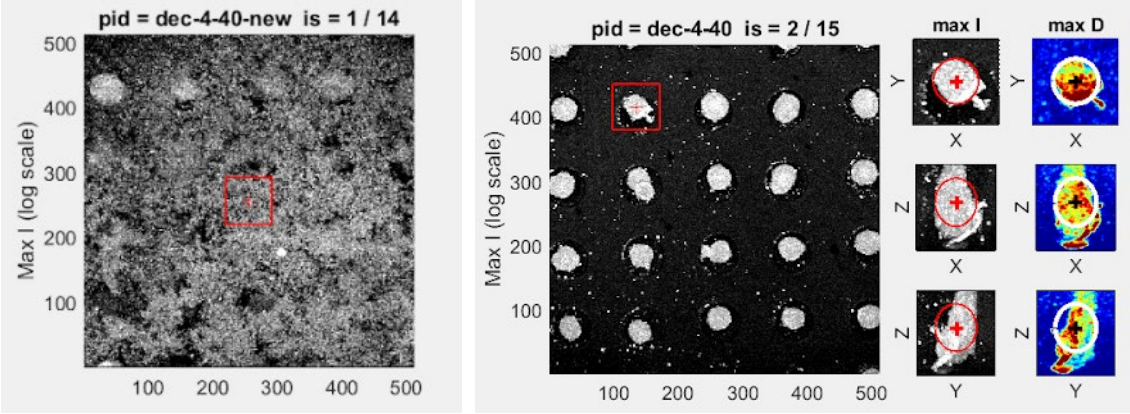


**Figure 9.** Examples of challenges faced during image analysis when selecting spheroid ROI. [eid = 180823, did = 0808_dec_4-40; eid = 180705, did = DLS_LSM03_dec_4-40]

heterogeneity and "floaters" (spheroids that begin to float or crawl out of the wells) also made it difficult to select ROIs (**Fig. 9**). Lastly, of the approximately 16 spheroids captured within the OCT FOV, sometimes as few as 5 of the spheroids were analyzed as result of these issues. Despite these challenges, it should not detract from the study results; instead, it must be highly scrutinized and used to guide technological improvements and protocols moving forward.

## 3.5 Conclusion

Advancements in optical technology and tissue culturing methods have augmented imaging 3D microtissues that more closely mimic the in vivo environment. The study validated the feasibility of OCT imaging as a functional testing platform for the measurement of viability-linked parameters. There were both dose- and time-dependent changes in intensity, decorrelation, and normalized decorrelation that may be associated with cell disruption from ethanol-induced apoptosis and necrosis. These observations were enabled by label-free tracking of multiple spheroids over time, thus supporting the capability of our OCT system as a potential means for high-throughput, longitudinal, and multi-metric assessment of viability-linked parameters. Further understanding of the underlying biophysiological mechanisms will reinforce the

interpretation of metric measurements once more selective cell line, drug, and assays are chosen in future studies, like what is described in the following section.

# 4. Cell Viability of Neurospheroids Treated with Metabolism Inhibitors

## 4.1 Abstract

Understanding how changes in OCT metrics are linked to underlying fluctuations in cellular viability is a critical step in validating the OCT imaging system for functional testing of anti-cancer drugs. Here, neurospheroids were treated with two different metabolism inhibitors to selectively target glycolysis and mitochondrial respiration. Significant time-dependent changes in viability-linked metrics were observed for both drugs, demonstrating the utility OCT could have in functional imaging for anticancer drug regimen selection.

## 4.2 Methods

### 4.2.1 Neurospheroid culturing

Primary cortical tissue was isolated from Charles River rats at postnatal day 1-3 (one female and one male for oligomycin A and 2-DG, respectively). The rats were wrapped in gauze and cling wrap and placed in a container of ice allowing for hypothermia induction without direct contact with the ice. Dissection scissors were used to decapitate the rat between the ears and shoulder. The brain was exposed, the cortex removed, and the tissue was immediately placed in a petri dish with a buffer solution of 49 mL Hibernate A (BrainBits LLC, Springfield, IL) supplemented with 1 mL B27 (Invitrogen, Carlsbad, CA) and 125 µL GlutaMAX (Invitrogen, Carlsbad, CA).

A modified cell isolation protocol from Dingle et al. was used[69]. Briefly, the cortex was cut up into smaller pieces before being placed in a fresh solution of 6 mg powdered papain

dissolved into 3 mL of Hibernate A with calcium chloride for 30 minutes at 30°C. The papain solution was removed, buffer was added, and a fire-polished Pasteur pipette was used to dissociate the tissue by triturating the mixture 20 times. The cell solution was passed through a 40 µM strainer and 3 mL of buffer was used to push through the remaining cells. The cell solution was centrifuged at 150 g for 5 minutes and the supernatant was carefully removed. This washing process was repeated using warmed media made up of Neurobasal A medium (Invitrogen, Carlsbad, CA) supplemented with Penicillin-Streptomycin (Invitrogen, Carlsbad, CA), GlutaMAX, and B27. The cells were resuspended in 5 mL of media, filtered through a 40 µM strainer (using 3 mL of media to push through the remaining cells), centrifuged at 150 g for 5 minutes, and supernatant was removed. The cells were resuspended in 5 mL of media, centrifuged at 150 g for 5 minutes, and supernatant was removed. The cells were resuspended one final time in 10 mL of media. 10 µL of the cell solution was pipetted into a small Eppendorf tube to assess cell viability following the Trypan Blue Exclusion Assay. For seeding, the cell solution was centrifuged one final time at 150 g for 5 minutes. Media was carefully pipetted out and the cell pellet was resuspended in the appropriate volume of media. Cells were seeded onto a 2% agarose microgel at a density of 4,000 cells per well.

To make the microgels, 4 g autoclaved agarose (Invitrogen, Carlsbad, CA) was mixed with 200 mL phosphate-buffered saline (PBS) to create a 2% agarose solution. The molten agarose was poured over a MicroTissues mold with 96, 400 uM diameter pegs (#24-96 Small Spheroids, MicroTissues, Providence, RI). The freshly made microgels were individually placed into the bottom of a 24-well glass bottom plate (Part No: P24G-1.5-13-F, MatTek, Ashland, MA) and equilibrated with 3 media changes over 48 hours. Prior to seeding, media was removed from the wells and 75 µL of the cortical tissue cell solution was dispensed directly over the microgel and allowed to settle and incubate for 40 minutes, with slight lateral agitation at the halfway

point. This was to ensure that the cell suspension aggregates into the concave wells. After incubation, 1 mL of media was pipetted to the sides of the of the 24-well plate, ensuring the microgel was completely covered by media and not floating in the well. The neurospheroids were incubated at 37°C in a 5% $CO_2$ environment, and the full volume of media was replaced every 3-4 days with fresh media. Neurospheroids were provided by the Hoffman-Kim Lab (Brown University, Providence, RI) and cultured by Aurora Washington and Rafael De Cruz (Hoffman-Kim Lab, Brown University).

### 4.2.2 Metabolism inhibitor exposure

Neurospheroids at 10 days in vitro (DIV) were treated with either oligomycin A (1 μM, 5 μM, and 10 μM) or 2-DG (5mM, 25mM, and 50mM) to selectively disrupt mitochondrial respiration or glycolysis, respectively. Powdered oligomycin A (5 mg) was reconstituted using 1 mL of dimethyl sulfoxide (DMSO). The solution was divided into 45 μL aliquots and diluted into media for a total volume of 4.5 mL working stock solution. Since 2-DG is not stable in water for more than a day, fresh batches of 2-DG were made prior to the start of each experiment. Powdered 2-DG (50 mg) was reconstituted using 1 mL of distilled (DI) water with a syringe filter, producing a 0.305 M stock solution.

A concentration 1.07 times the desired treatment concentration was used for both oligomycin A (1.07 μM, 5.35 μM, and 10.7 μM) and 2-DG (5.35 mM, 26.75 mM, and 53.5 mM) to account for media remaining in the equilibrated agarose gel after the remaining media was pipetted out of the well. Based on the corrected concentrations, the appropriate volumes of working stock solution, DMSO or DI water, and media were measured out and combined to a total volume of 1 mL. At the start of the experiment, media was carefully pipetted out of the well and replaced with the appropriate drug solution. Caution was taken to slowly pipette the treatment solution into the well and not directly over the gel to avoid dislodging spheroids or flipping the

gel. Pre-treatment data was acquired at DIV 10, along with 12 hours and 24 hours after drug administration.

### 4.2.3 Mini-incubator setup

A mini-incubator was developed and tested by Ahbid Zein-Sabatto (Lee Lab, Brown University). It was affixed to and elevated on an OCT platform positioned next to the SD-OCT in a "bottom up" imaging setup. The mini-incubator allows for longitudinal imaging of the plate by controlling the temperature and environment of the in vitro sample in between and during imaging sessions. This minimizes the amount of sample handling as the plate does not have to be moved to a separate housing throughout the entirety of the experiment.

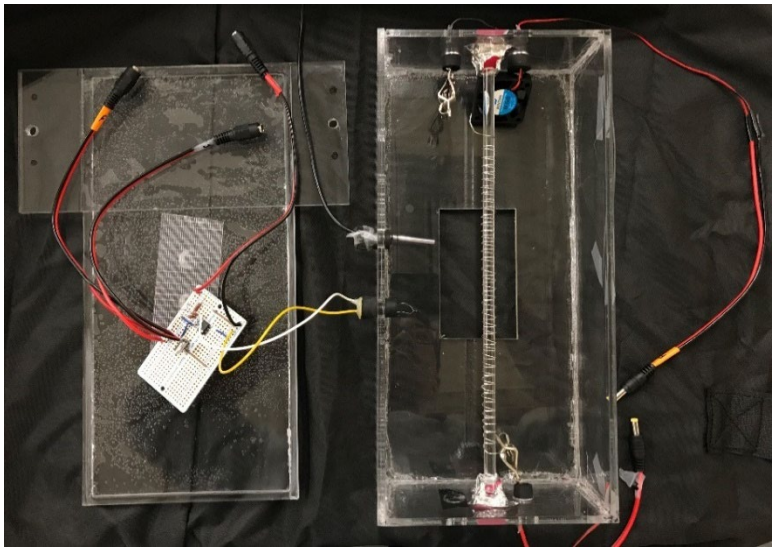

**Figure 10.** Mini-incubator used during and in between OCT imaging.

The mini-incubator was made using transparent acrylic panels sealed with acrylic cement to form an 33 x 16 x 8 cm rectangular container (**Fig. 10**). A rectangular cut out on the bottom of the box allows for bottom up imaging of the sample. The top of the box was made of an acrylic panel that can be pushed into place and sealed using two large rubber O-rings. A thermistor and temperature probe are inserted into the box to ensure a constant temperature reading inside the

mini-incubator of approximately 37±1°C. A nichrome coil affixed towards the top and spans the length of the box is used to heat the mini-incubator. A small fan inside the box periodically changes direction to ensure the heated air is constantly circulated throughout the inside the enclosure. A circuit board manages the temperature inside the incubator. Future iterations of the mini-incubator will allow for an air-tight seal with gas control, among other features.

### 4.2.4 OCT imaging system and data acquisition

The SD-OCT system from Thorlabs (Thorlabs, Newton, NJ, USA) was used for 3D volumetric imaging in this study. The system uses a superluminescent diode light source to provide a bandwidth of 170 nm, a central wavelength of 1310 nm, and an axial resolution of 3.5 µm. An LSM03 lens (Thorlabs, Newton, NJ, USA) optimized for scanning systems was used in all experiments.

**Figure 11**. SD-OCT imaging setup with mini-incubator. The mini-incubator was elevated above the SD-OCT using an OCT platform to allow for longitudinal, bottom up imaging of the sample plate.

The sample was placed inside the mini-incubator and aligned with the rectangular cutout window. With this setup, the SD-OCT is rotated so that the LSM03 lens is pointed upwards towards the plate and aligned with the microgel being imaged (**Fig. 11**). The SD-OCT system, generator, and other related hardware and wires are placed on or affixed to an optical table that is supported by legs which use pressurized air to isolate environmental vibrations (Thorlabs, Newton, NJ). This helps to isolate vibrations during image acquisition, minimizing the amount of noise and distortions associated with such movements.

The ThorImageOCT Software (Thorlabs, Newton, NJ) was used to visualize and focus the sample in real-time (**Fig. 12**) prior to data acquisition. After manual positioning of the SD-OCT directly underneath the gel of interest, the electronic z-axis translator (Thorlabs, Newton, NJ) was used to adjust the focal plane along the optical axis until the sample came into view and its surface aligned with the focal plane. The reference mirror distance was adjusted by turning the dial on the SD-OCT until spheroids were positioned in the real-time B-scan images at approximately 0.8 mm in the z-direction. When necessary, these steps were repeated until the image was optimally focused in 2D. A 3D scan was then recorded and cross-sectional XY slices were scrolled through to ensure all the desired, whole spheroids are cropped into the voxel in the subsequent data acquisition.

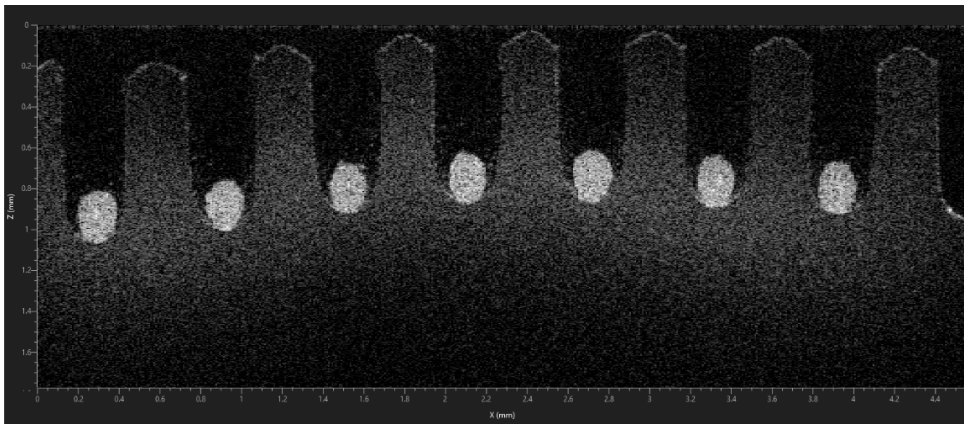


**Figure 12.** Real-time B-scan visual of neurospheroids in ThorImageOCT Software.

The custom Lee Lab app written in LabVIEW software (National Instruments, Austin, TX, USA) was used for OCT volume data acquisition. Parameters were set prior to acquisition and are dependent upon the scanning protocol used and the number of gels being imaged. The preset "Angiogram" protocol was used to obtain the geometry, intensity, and decorrelation data. The FOV was set to 512 x 512 x 1024 pixels in the x, y, z direction, respectively, which translates to an imaging volume of approximately 5 x 5 x 3 mm being captured. The number of repeating B-scans was set to four with a time delay of 10 ms between scans in order to measure the decorrelation. Specific to when 8 gels were being imaged (technical duplicates), the number of pixels in the y-direction was halved to 256 pixels when running the Angiogram protocol. This modification was made in consideration to the data size and how much additional time is needed to acquire and transfer such a larger amount. Data was acquired before treatment (pre-treatment) as well as 12 and 24 hours after the drug was administered.

### 4.2.5 OCT data processing

Reconstruction of the OCT data and image analysis for investigational OCT metrics was carried out using Lee Lab codes in MATLAB (MathWorks, Natick, MA, USA). Reconstructing the raw data involved cropping the volume, determining optimal dispersion compensation, and averaging the volumes. Using the reconstructed data, generally 10-20 spheroids from the middle of each microgel were chosen and segmented for longitudinal analysis. Individual spheroids were automatically segmented from the reconstructed intensity images. The geometry, intensity, and decorrelation-oriented metrics were then obtained as 3D maps. The mean metric values were measured for each of the selected spheroids and tracked longitudinally at 12 hours and 24 hours. Metrics for spheroid subregions of shell, body, and core were outputted by geometrically defining the boundaries using the distance from the spheroid surface and a ratio of voxel numbers. A

relationship of 1/2 to 3/8 to 1/8 of the voxels relative to the total number of voxels in the spheroid was used to define the spheroid shell, body, and core, respectively, as can be seen in the delineated subregions of spheroids shown in **Figure 13** below.

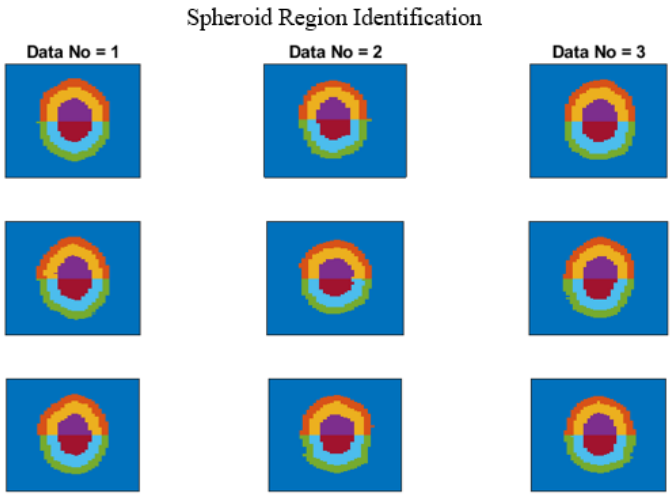


**Figure 13.** Subregions of sample spheroids are shown from top to bottom as top-shell (ts), top-body (tb), top-core (ts), bottom-core (bc), bottom-body (bb), and bottom-shell (bs) and are colored orange, yellow, purple, red, blue, and green, respectively.

### 4.2.6 Live/Dead assay

A live/dead assay was conducted to assess the cytotoxicity of varying concentrations of oligomycin A and 2-DG after 24 hours of treatment in neurospheroids. A LIVE/DEAD™ Viability/Cytotoxicity Kit, for mammalian cells #L3224 (Thermo Fisher Scientific, Waltham, MA), was used and the assay was carried out by Ahbid Zein-Sabatto per the manufacturer's protocol. The reagents calcein AM (4 mM) and ethidium homodimer-1 (2 mM) were diluted in SFM to a corrected concentration 1.07 times the desired concentration to account for SFM remaining in the equilibrated agarose gel after the remaining media was pipetted out of the well. A final concentration of 2.14 µM and 4.28 µM were used for calcein AM and ethidium homodimer-1, respectively. Briefly, the drug treatment solution was pipetted out of the well

followed by a wash using serum-free media (SFM) and 10 minutes of incubation. The washes were repeated for a total of three cycles. The reagent was pipetted into the wells and incubated for 30 minutes while being wrapped in tinfoil (to protect from light).

A Zeiss Axiovert 200M Fluorescence Microscope (Carl Zeiss, Oberkochen, Germany) was used for live/dead imaging of the labeled cells. Calcein AM dye has an excitation and emission wavelength of about 494 nm and 517 nm, respectively, and displays a bright green color under fluorescence signifying its incorporation into living cells. The filter was set to fluorescein isothiocyanate (FITC) for live imaging. In the presence of DNA, ethidium homodimer-1 has an excitation and emission wavelength of 528 nm and 617 nm, respectively, thereby entering cells with damaged membranes and displaying a vibrant red fluorescence in dead cells. The tetramethylrhodamine (TRITC) filter was used to capture dead cells. A 5x objective was used for all fluorescence imaging. Bright-field images were also acquired for qualitative assessment.

AxioVision software (Carl Zeiss, Oberkochen, Germany) was used to visualize and capture images. A preset "min/max" filter was applied to all images in AxioVision. ImageJ software (U.S. National Institutes of Health, Bethesda, MD) was used for brightness and contrast adjustments of the images. The same adjustments were applied to all the images for a single biological replicate in order to avoid introducing bias. Pixel analysis of the acquired fluorescence images was carried out using a custom code in MATLAB and averaged over 10 spheroids for each well. A global threshold was applied to the images to produce a more conservative calculation of metrics. Area was quantified by multiplying the number of pixels in a chosen ROI by a single pixel area (3 μm x 3 μm). The integrated density was calculated by multiplying the area by the average intensity.

### 4.2.7 ATP assay

An ATP assay was conducted 24 hours after neurospheroids were treated with varying concentrations of 2-DG. ATP is present in all metabolically active cells; however, when cells undergo apoptosis or necrosis, the amount of ATP is altered, therefore acting as a fundamental marker of cell viability. A luciferase reaction is the principle mechanism underlying this assay such that a luminescence signal is produced proportional to the amount of ATP in the sample.

A CellTiter-Glo® 3D Cell Viability Assay (Promega, Madison, WI) was used and carried out by Ahbid Zein-Sabatto per the manufacturer's protocol. Briefly, spheroids were carefully pipetted out of the microgel with 100 µL of media one-by-one and separated into individual wells of a 96-well clear bottom, white-walled plate #3610 (Corning, Corning, NY). 100 µL of the reagent was added using a pipette and the plate was mixed using a Titer Plate Shaker set to "3" for five minutes (Barnstead, Dubuque, IA). Cell lysis during the mixing step is critical for disaggregating the neurospheroid and liberating the cellular ATP from the sample. The plate was incubated for 25 minutes at room temperature. Luminescence was recorded using a BioTek Synergy H1 Hybrid microplate reader (BioTek, Winooski, VT). A single plate was run three times consecutively with the plate lid on and the average value from the three runs was used.

### 4.2.8 Statistical analysis

Investigational OCT metric results are presented as means ± standard error at each time point of the voxels within the automatically segmented spheroids, for one biological replicate for each drug. The distribution of the data did not pass normality according to the Shapiro-Wilk Test nor did it demonstrate homogeneity of variance according to Levene's Test, so Mood's median test was chosen for statistical analysis given its conservative nature. Additionally, a Bonferroni correction was used to account for the two comparisons, resulting in an adjustment of one-half

alpha. Longitudinal differences between time points were assessed using Mood's median test to compare each subsequent time point to the pre-treatment value. Statistical analysis was used to assess if there were any significant time-dependent changes in metric measurements at each of the treatment concentrations for both metabolism inhibitors.

## 4.3 Results

### 3.3.1 Results of metrics

A results table of the metrics with the mean, standard error (SE), and statistical significance for each concentration and time point can be found in **Table 4** below.

**Table 4.** Results summary tables of investigational OCT metrics for oligomycin A and 2-DG. An adjustment of ½ alpha was used per Bonferroni's correction: *p≤ 0.025.

| | | | Geometry | | | | | | | | | | | |
|---|---|---|---|---|---|---|---|---|---|---|---|---|---|---|
| | | | Volume | | | Area | | | AVR | | | SR | | |
| | | | Pre-t | 12 hr | 24 hr | Pre-t | 12 hr | 24 hr | Pre-t | 12 hr | 24 hr | Pre-t | 12 hr | 24 hr |
| Oligomycin A | 0 µM | Mean | 5.85E+06 | 5.74E+06 | 6.00E+06 | 1.86E+05 | 1.83E+05 | 1.88E+05 | 3.19E-02 | 3.20E-02 | 3.13E-02 | 1.09E+00 | 1.09E+00 | 1.08E+00 |
| | | SE | 1.12E+05 | 9.22E+04 | 1.12E+05 | 2.53E+03 | 2.02E+03 | 2.49E+03 | 1.90E-04 | 1.72E-04 | 1.71E-04 | 8.97E-04 | 8.56E-04 | 7.85E-04 |
| | | P-value | | | | | | | | | | | | * |
| | 1 µM | Mean | 6.18E+06 | 8.45E+06 | 8.79E+06 | 1.95E+05 | 2.44E+05 | 2.50E+05 | 3.16E-02 | 2.93E-02 | 2.87E-02 | 1.10E+00 | 1.11E+00 | 1.10E+00 |
| | | SE | 1.15E+05 | 4.66E+05 | 4.21E+05 | 2.76E+03 | 9.89E+03 | 9.31E+03 | 1.95E-04 | 5.34E-04 | 3.95E-04 | 1.89E-03 | 3.11E-03 | 3.35E-03 |
| | | P-value | | * | * | | * | * | | * | * | | * | |
| | 5 µM | Mean | 5.88E+06 | 9.54E+06 | 9.69E+06 | 1.87E+05 | 2.62E+05 | 2.64E+05 | 3.19E-02 | 2.75E-02 | 2.73E-02 | 1.09E+00 | 1.10E+00 | 1.10E+00 |
| | | SE | 1.61E+05 | 2.51E+05 | 2.86E+05 | 3.82E+03 | 4.55E+03 | 5.35E+03 | 2.94E-04 | 2.82E-04 | 2.63E-04 | 2.49E-03 | 1.12E-03 | 7.63E-04 |
| | | P-value | | * | * | | * | * | | * | * | | * | * |
| | 10 µM | Mean | 5.31E+06 | 1.00E+07 | 1.01E+07 | 1.73E+05 | 2.68E+05 | 2.72E+05 | 3.27E-02 | 2.68E-02 | 2.70E-02 | 1.09E+00 | 1.09E+00 | 1.10E+00 |
| | | SE | 9.16E+04 | 2.08E+05 | 2.07E+05 | 2.05E+03 | 3.92E+03 | 3.94E+03 | 1.89E-04 | 1.72E-04 | 1.85E-04 | 6.28E-04 | 8.26E-04 | 1.36E-03 |
| | | P-value | | * | * | | * | * | | * | * | | * | * |
| 2-Deoxy-D-Glucose (2-DG) | 0 mM | Mean | 5.14E+06 | 5.14E+06 | 5.18E+06 | 1.70E+05 | 1.71E+05 | 1.71E+05 | 3.33E-02 | 3.36E-02 | 3.32E-02 | 1.09E+00 | 1.09E+00 | 1.09E+00 |
| | | SE | 1.07E+05 | 1.65E+05 | 1.26E+05 | 2.45E+03 | 3.91E+03 | 2.77E+03 | 2.29E-04 | 4.40E-04 | 3.22E-04 | 6.52E-04 | 7.75E-04 | 1.32E-03 |
| | | P-value | | | | | | | | | | | | |
| | 5 mM | Mean | 6.71E+06 | 6.35E+06 | 7.16E+06 | 2.05E+05 | 1.97E+05 | 2.15E+05 | 3.07E-02 | 3.13E-02 | 3.04E-02 | 1.09E+00 | 1.09E+00 | 1.10E+00 |
| | | SE | 1.84E+05 | 2.39E+05 | 2.98E+05 | 3.97E+03 | 4.89E+03 | 6.07E+03 | 2.99E-04 | 5.12E-04 | 5.20E-04 | 2.20E-03 | 1.76E-03 | 1.45E-03 |
| | | P-value | | | | | | | | | | | | |
| | 25 mM | Mean | 5.45E+06 | 5.92E+06 | 6.87E+06 | 1.76E+05 | 1.86E+05 | 2.07E+05 | 3.27E-02 | 3.18E-02 | 3.04E-02 | 1.09E+00 | 1.09E+00 | 1.09E+00 |
| | | SE | 1.75E+05 | 1.83E+05 | 2.03E+05 | 3.85E+03 | 3.86E+03 | 4.11E+03 | 3.91E-04 | 3.50E-04 | 3.10E-04 | 4.28E-04 | 4.46E-04 | 5.62E-04 |
| | | P-value | | | * | | | * | | | * | | | * |
| | 50 mM | Mean | 6.39E+06 | 7.03E+06 | 7.63E+06 | 1.99E+05 | 2.12E+05 | 2.27E+05 | 3.12E-02 | 3.04E-02 | 3.01E-02 | 1.09E+00 | 1.09E+00 | 1.10E+00 |
| | | SE | 1.34E+05 | 1.50E+05 | 2.53E+05 | 2.77E+03 | 2.96E+03 | 4.78E+03 | 2.47E-04 | 2.69E-04 | 4.04E-04 | 1.28E-03 | 1.67E-03 | 1.48E-03 |
| | | P-value | | | * | | | * | | | | | | * |

| | | | Intensity | | | | | | | | | | | |
|---|---|---|---|---|---|---|---|---|---|---|---|---|---|---|
| | | | Whole | | | Shell | | | Body | | | Core | | |
| | | | Pre-t | 12 hr | 24 hr | Pre-t | 12 hr | 24 hr | Pre-t | 12 hr | 24 hr | Pre-t | 12 hr | 24 hr |
| Oligomycin A | 0 µM | Mean | 2.49E-07 | 2.62E-07 | 3.02E-07 | 1.30E-07 | 1.33E-07 | 1.65E-07 | 3.36E-07 | 3.53E-07 | 3.98E-07 | 4.61E-07 | 5.02E-07 | 5.58E-07 |
| | | SE | 1.41E-08 | 1.32E-08 | 1.09E-08 | 5.38E-09 | 5.09E-09 | 4.07E-09 | 2.03E-08 | 1.89E-08 | 1.54E-08 | 3.04E-08 | 2.89E-08 | 2.49E-08 |
| | | P-value | | | | | | * | | | | | | |
| | 1 µM | Mean | 3.43E-07 | 3.12E-07 | 3.25E-07 | 1.46E-07 | 1.17E-07 | 1.32E-07 | 5.05E-07 | 4.46E-07 | 4.53E-07 | 6.41E-07 | 6.90E-07 | 7.08E-07 |
| | | SE | 8.33E-09 | 2.17E-08 | 1.27E-08 | 2.34E-09 | 4.02E-09 | 3.67E-09 | 1.32E-08 | 3.43E-08 | 1.98E-08 | 1.90E-08 | 5.61E-08 | 3.23E-08 |
| | | P-value | | | | | * | | | | | | | |
| | 5 µM | Mean | 2.46E-07 | 2.81E-07 | 2.97E-07 | 1.20E-07 | 1.24E-07 | 1.43E-07 | 3.34E-07 | 3.80E-07 | 3.85E-07 | 4.80E-07 | 6.11E-07 | 6.42E-07 |
| | | SE | 1.26E-08 | 1.00E-08 | 1.43E-08 | 4.56E-09 | 1.85E-09 | 6.03E-09 | 1.88E-08 | 1.50E-08 | 1.85E-08 | 2.79E-08 | 2.90E-08 | 3.71E-08 |
| | | P-value | | * | | | | | | | | | * | * |
| | 10 µM | Mean | 3.50E-07 | 3.37E-07 | 3.26E-07 | 1.82E-07 | 1.74E-07 | 1.97E-07 | 4.68E-07 | 4.29E-07 | 3.96E-07 | 6.63E-07 | 7.15E-07 | 6.30E-07 |
| | | SE | 9.28E-09 | 7.79E-09 | 1.20E-08 | 3.81E-09 | 2.47E-09 | 7.13E-09 | 1.30E-08 | 1.10E-08 | 1.47E-08 | 2.14E-08 | 2.21E-08 | 2.69E-08 |
| | | P-value | | | | | | * | | | * | | | |
| 2-Deoxy-D-Glucose (2-DG) | 0 mM | Mean | 3.31E-07 | 2.56E-07 | 2.59E-07 | 1.57E-07 | 1.09E-07 | 1.20E-07 | 4.74E-07 | 3.69E-07 | 3.63E-07 | 5.90E-07 | 5.02E-07 | 4.95E-07 |
| | | SE | 1.42E-08 | 1.64E-08 | 9.88E-09 | 3.73E-09 | 3.78E-09 | 4.19E-09 | 2.38E-08 | 2.68E-08 | 1.44E-08 | 3.03E-08 | 3.87E-08 | 2.39E-08 |
| | | P-value | | | | | * | * | | | | | | |
| | 5 mM | Mean | 3.55E-07 | 3.26E-07 | 2.98E-07 | 1.60E-07 | 1.75E-07 | 1.50E-07 | 5.23E-07 | 4.61E-07 | 4.17E-07 | 6.32E-07 | 5.25E-07 | 5.26E-07 |
| | | SE | 1.94E-08 | 2.20E-08 | 1.44E-08 | 6.42E-09 | 8.87E-09 | 5.86E-09 | 3.14E-08 | 3.39E-08 | 2.29E-08 | 3.99E-08 | 4.01E-08 | 2.80E-08 |
| | | P-value | | | * | | | | | | * | | | * |
| | 25 mM | Mean | 3.05E-07 | 3.98E-07 | 3.13E-07 | 1.76E-07 | 2.42E-07 | 1.68E-07 | 4.13E-07 | 5.34E-07 | 4.19E-07 | 4.94E-07 | 6.14E-07 | 5.70E-07 |
| | | SE | 2.24E-08 | 6.61E-09 | 7.38E-09 | 1.35E-08 | 5.48E-09 | 2.65E-09 | 3.02E-08 | 8.87E-09 | 1.05E-08 | 3.62E-08 | 1.20E-08 | 1.84E-08 |
| | | P-value | | | | | * | | | | | | | |
| | 50 mM | Mean | 3.74E-07 | 3.65E-07 | 2.68E-07 | 1.84E-07 | 2.01E-07 | 1.40E-07 | 5.54E-07 | 5.20E-07 | 3.71E-07 | 5.91E-07 | 5.51E-07 | 4.67E-07 |
| | | SE | 1.00E-08 | 9.07E-09 | 1.09E-08 | 3.98E-09 | 4.06E-09 | 5.56E-09 | 1.62E-08 | 1.40E-08 | 1.71E-08 | 1.76E-08 | 1.63E-08 | 2.56E-08 |
| | | P-value | | | * | | | * | | | * | | | * |

| | | | Intensity CoV | | | | | | | | | | | |
|---|---|---|---|---|---|---|---|---|---|---|---|---|---|---|
| | | | Whole | | | Shell | | | Body | | | Core | | |
| | | | Pre-t | 12 hr | 24 hr | Pre-t | 12 hr | 24 hr | Pre-t | 12 hr | 24 hr | Pre-t | 12 hr | 24 hr |
| Oligomycin A | 0 µM | Mean | 6.70E-01 | 6.95E-01 | 6.79E-01 | 8.79E-01 | 8.95E-01 | 8.81E-01 | 3.59E-01 | 3.83E-01 | 3.91E-01 | 1.86E-01 | 1.91E-01 | 2.02E-01 |
| | | SE | 1.28E-02 | 1.37E-02 | 1.06E-02 | 1.91E-02 | 2.11E-02 | 1.69E-02 | 8.28E-03 | 1.11E-02 | 9.64E-03 | 4.11E-03 | 5.33E-03 | 4.57E-03 |
| | | P-value | | * | | | | | | * | | | | * |
| | 1 µM | Mean | 6.74E-01 | 7.42E-01 | 7.64E-01 | 6.66E-01 | 5.65E-01 | 8.29E-01 | 2.61E-01 | 3.23E-01 | 3.53E-01 | 1.89E-01 | 1.99E-01 | 2.06E-01 |
| | | SE | 6.96E-03 | 2.20E-02 | 1.25E-02 | 1.57E-02 | 2.45E-02 | 5.39E-02 | 1.12E-02 | 9.88E-03 | 1.02E-02 | 7.53E-03 | 7.04E-03 | 9.08E-03 |
| | | P-value | | | * | | * | * | | * | * | | | |
| | 5 µM | Mean | 7.26E-01 | 7.75E-01 | 7.84E-01 | 9.25E-01 | 8.85E-01 | 9.84E-01 | 4.04E-01 | 4.24E-01 | 4.58E-01 | 2.07E-01 | 2.30E-01 | 2.36E-01 |
| | | SE | 1.44E-02 | 1.53E-02 | 1.55E-02 | 1.94E-02 | 1.57E-02 | 5.62E-02 | 1.42E-02 | 1.19E-02 | 1.18E-02 | 1.20E-02 | 8.27E-03 | 6.82E-03 |
| | | P-value | | * | * | | | | | | * | | * | * |
| | 10 µM | Mean | 6.97E-01 | 7.75E-01 | 8.03E-01 | 9.16E-01 | 1.07E+00 | 1.25E+00 | 3.81E-01 | 4.37E-01 | 4.59E-01 | 1.93E-01 | 2.25E-01 | 2.35E-01 |
| | | SE | 6.70E-03 | 9.33E-03 | 1.98E-02 | 1.04E-02 | 3.01E-02 | 5.73E-02 | 6.57E-03 | 6.39E-03 | 1.02E-02 | 6.70E-03 | 5.92E-03 | 7.57E-03 |
| | | P-value | | * | * | | * | * | | * | * | | * | * |
| 2-Deoxy-D-Glucose (2-DG) | 0 mM | Mean | 6.78E-01 | 7.20E-01 | 6.98E-01 | 8.15E-01 | 8.32E-01 | 7.89E-01 | 3.30E-01 | 3.53E-01 | 3.51E-01 | 1.59E-01 | 1.62E-01 | 1.66E-01 |
| | | SE | 8.48E-03 | 1.33E-02 | 1.19E-02 | 3.27E-02 | 3.14E-02 | 3.88E-02 | 1.85E-02 | 1.84E-02 | 1.67E-02 | 5.01E-03 | 6.45E-03 | 4.91E-03 |
| | | P-value | | | | | | | | | | | | |
| | 5 mM | Mean | 6.66E-01 | 5.89E-01 | 6.26E-01 | 7.62E-01 | 6.89E-01 | 6.90E-01 | 2.94E-01 | 2.80E-01 | 2.96E-01 | 1.55E-01 | 1.81E-01 | 1.72E-01 |
| | | SE | 1.86E-02 | 2.44E-02 | 2.43E-02 | 4.75E-02 | 5.03E-02 | 5.20E-02 | 1.65E-02 | 2.15E-02 | 2.31E-02 | 5.73E-03 | 9.21E-03 | 6.00E-03 |
| | | P-value | | | | | | | | | | | | |
| | 25 mM | Mean | 6.49E-01 | 6.15E-01 | 6.56E-01 | 8.77E-01 | 8.41E-01 | 8.21E-01 | 3.69E-01 | 3.38E-01 | 3.62E-01 | 1.71E-01 | 1.93E-01 | 1.65E-01 |
| | | SE | 8.13E-03 | 6.50E-03 | 8.38E-03 | 1.24E-02 | 8.46E-03 | 9.50E-03 | 8.23E-03 | 5.12E-03 | 7.03E-03 | 6.47E-03 | 5.08E-03 | 4.34E-03 |
| | | P-value | | | | | * | * | | * | | | | |
| | 50 mM | Mean | 5.94E-01 | 5.53E-01 | 6.17E-01 | 6.31E-01 | 5.76E-01 | 7.40E-01 | 2.16E-01 | 2.41E-01 | 2.77E-01 | 1.56E-01 | 1.90E-01 | 1.63E-01 |
| | | SE | 8.26E-03 | 6.41E-03 | 2.37E-02 | 1.13E-02 | 7.97E-03 | 4.67E-02 | 1.03E-02 | 9.15E-03 | 1.38E-02 | 6.41E-03 | 6.22E-03 | 4.49E-03 |
| | | P-value | | * | | | * | | | | * | | * | |

| | | | Decorrelation, 10 ms | | | | | | | | | | | |
|---|---|---|---|---|---|---|---|---|---|---|---|---|---|---|
| | | | Whole | | | Shell | | | Body | | | Core | | |
| | | | Pre-t | 12 hr | 24 hr | Pre-t | 12 hr | 24 hr | Pre-t | 12 hr | 24 hr | Pre-t | 12 hr | 24 hr |
| Oligomycin A | 0 µM | Mean | 2.88E-08 | 3.21E-08 | 4.52E-08 | 2.71E-08 | 3.02E-08 | 4.56E-08 | 3.05E-08 | 3.39E-08 | 4.59E-08 | 3.09E-08 | 3.42E-08 | 4.17E-08 |
| | | SE | 3.97E-10 | 4.77E-10 | 1.16E-09 | 2.35E-10 | 3.47E-10 | 1.23E-09 | 5.42E-10 | 6.00E-10 | 1.27E-09 | 6.22E-10 | 6.74E-10 | 8.72E-10 |
| | | P-value | | * | * | | * | * | | * | * | | * | * |
| | 1 µM | Mean | 3.35E-08 | 6.90E-08 | 6.55E-08 | 3.07E-08 | 6.54E-08 | 6.26E-08 | 3.64E-08 | 7.34E-08 | 7.16E-08 | 3.62E-08 | 7.01E-08 | 5.89E-08 |
| | | SE | 2.39E-10 | 3.42E-09 | 1.83E-09 | 1.58E-10 | 2.75E-09 | 1.35E-09 | 3.31E-10 | 4.22E-09 | 2.55E-09 | 3.80E-10 | 4.00E-09 | 1.88E-09 |
| | | P-value | | * | * | | * | * | | * | * | | * | * |
| | 5 µM | Mean | 2.84E-08 | 5.85E-08 | 6.16E-08 | 2.66E-08 | 5.28E-08 | 5.82E-08 | 3.01E-08 | 6.35E-08 | 6.58E-08 | 3.05E-08 | 6.61E-08 | 6.20E-08 |
| | | SE | 2.69E-10 | 1.70E-09 | 2.29E-09 | 1.65E-10 | 1.32E-09 | 1.76E-09 | 3.84E-10 | 2.06E-09 | 3.01E-09 | 4.29E-10 | 2.34E-09 | 2.45E-09 |
| | | P-value | | * | * | | * | * | | * | * | | * | * |
| | 10 µM | Mean | 3.60E-08 | 8.91E-08 | 6.30E-08 | 3.34E-08 | 9.47E-08 | 5.94E-08 | 3.84E-08 | 8.64E-08 | 6.86E-08 | 3.90E-08 | 7.51E-08 | 6.07E-08 |
| | | SE | 4.60E-10 | 2.28E-09 | 1.58E-09 | 3.27E-10 | 2.67E-09 | 1.36E-09 | 6.15E-10 | 2.12E-09 | 1.96E-09 | 5.73E-10 | 1.66E-09 | 1.51E-09 |
| | | P-value | | * | * | | * | * | | * | * | | * | * |
| 2-Deoxy-D-Glucose (2-DG) | 0 mM | Mean | 3.19E-08 | 3.09E-08 | 3.51E-08 | 2.91E-08 | 2.82E-08 | 3.32E-08 | 3.45E-08 | 3.34E-08 | 3.72E-08 | 3.55E-08 | 3.46E-08 | 3.66E-08 |
| | | SE | 3.55E-10 | 6.33E-10 | 7.65E-10 | 1.99E-10 | 3.89E-10 | 8.12E-10 | 5.07E-10 | 8.63E-10 | 8.30E-10 | 5.65E-10 | 9.78E-10 | 6.11E-10 |
| | | P-value | | | * | | | * | | | | | | |
| | 5 mM | Mean | 3.30E-08 | 3.55E-08 | 4.52E-08 | 2.99E-08 | 3.15E-08 | 4.14E-08 | 3.60E-08 | 3.85E-08 | 4.80E-08 | 3.67E-08 | 4.26E-08 | 5.16E-08 |
| | | SE | 6.01E-10 | 8.67E-10 | 1.31E-09 | 3.63E-10 | 5.00E-10 | 9.81E-10 | 8.48E-10 | 1.15E-09 | 1.61E-09 | 9.27E-10 | 1.58E-09 | 2.16E-09 |
| | | P-value | | * | * | | * | * | | | * | | * | * |
| | 25 mM | Mean | 3.17E-08 | 4.45E-08 | 5.11E-08 | 2.97E-08 | 3.75E-08 | 5.35E-08 | 3.36E-08 | 4.91E-08 | 4.93E-08 | 3.40E-08 | 5.85E-08 | 4.65E-08 |
| | | SE | 5.10E-10 | 4.19E-10 | 1.62E-09 | 3.68E-10 | 2.96E-10 | 2.22E-09 | 6.47E-10 | 5.50E-10 | 1.18E-09 | 6.83E-10 | 9.39E-10 | 8.43E-10 |
| | | P-value | | * | * | | * | * | | * | * | | * | * |
| | 50 mM | Mean | 3.31E-08 | 4.91E-08 | 5.65E-08 | 3.02E-08 | 4.26E-08 | 6.27E-08 | 3.61E-08 | 5.31E-08 | 5.27E-08 | 3.56E-08 | 6.27E-08 | 4.33E-08 |
| | | SE | 3.78E-10 | 7.75E-10 | 2.31E-09 | 2.47E-10 | 8.54E-10 | 2.66E-09 | 5.16E-10 | 8.27E-10 | 2.39E-09 | 5.61E-10 | 1.25E-09 | 1.02E-09 |
| | | P-value | | * | * | | * | * | | * | * | | * | * |

| | | | Decorrelation CoV, 10 ms | | | | | | | | | | | |
|---|---|---|---|---|---|---|---|---|---|---|---|---|---|---|
| | | | Whole | | | Shell | | | Body | | | Core | | |
| | | | Pre-t | 12 hr | 24 hr | Pre-t | 12 hr | 24 hr | Pre-t | 12 hr | 24 hr | Pre-t | 12 hr | 24 hr |
| Oligomycin A | 0 µM | Mean | 1.09E-01 | 1.17E-01 | 2.93E-01 | 1.12E-01 | 1.22E-01 | 3.56E-01 | 7.10E-02 | 8.45E-02 | 2.17E-01 | 5.13E-02 | 6.91E-02 | 9.94E-02 |
| | | SE | 5.97E-03 | 5.31E-03 | 2.05E-02 | 5.70E-03 | 5.31E-03 | 2.30E-02 | 3.00E-03 | 3.38E-03 | 1.85E-02 | 1.76E-03 | 2.79E-03 | 4.43E-03 |
| | | P-value | | | * | | | * | | * | * | | * | * |
| | 1 µM | Mean | 1.15E-01 | 2.75E-01 | 2.91E-01 | 9.48E-02 | 3.32E-01 | 3.37E-01 | 6.37E-02 | 2.07E-01 | 2.37E-01 | 5.63E-02 | 1.57E-01 | 1.30E-01 |
| | | SE | 2.64E-03 | 1.63E-02 | 2.65E-02 | 2.16E-03 | 2.24E-02 | 3.12E-02 | 1.81E-03 | 1.16E-02 | 2.47E-02 | 1.77E-03 | 9.92E-03 | 1.03E-02 |
| | | P-value | | * | * | * | * | * | | * | * | | * | * |
| | 5 µM | Mean | 1.12E-01 | 2.14E-01 | 2.91E-01 | 1.13E-01 | 2.40E-01 | 3.66E-01 | 7.58E-02 | 1.44E-01 | 2.08E-01 | 5.20E-02 | 1.47E-01 | 1.51E-01 |
| | | SE | 5.78E-03 | 9.47E-03 | 3.08E-02 | 5.57E-03 | 1.28E-02 | 4.11E-02 | 4.02E-03 | 5.20E-03 | 2.27E-02 | 2.33E-03 | 5.95E-03 | 8.17E-03 |
| | | P-value | | * | * | | * | * | | * | * | | * | * |
| | 10 µM | Mean | 1.28E-01 | 7.25E-01 | 3.34E-01 | 1.32E-01 | 8.79E-01 | 4.05E-01 | 8.61E-02 | 4.75E-01 | 2.62E-01 | 6.06E-02 | 1.55E-01 | 1.57E-01 |
| | | SE | 6.59E-03 | 3.04E-02 | 1.68E-02 | 7.12E-03 | 3.40E-02 | 1.99E-02 | 6.31E-03 | 2.64E-02 | 1.60E-02 | 4.00E-03 | 4.22E-03 | 6.35E-03 |
| | | P-value | | * | * | | * | * | | * | * | | * | * |
| 2-Deoxy-D-Glucose (2-DG) | 0 mM | Mean | 1.29E-01 | 1.36E-01 | 1.32E-01 | 1.14E-01 | 1.14E-01 | 1.36E-01 | 7.83E-02 | 9.05E-02 | 9.74E-02 | 6.48E-02 | 9.23E-02 | 8.74E-02 |
| | | SE | 4.05E-03 | 8.01E-03 | 8.72E-03 | 4.59E-03 | 5.96E-03 | 1.15E-02 | 3.01E-03 | 5.46E-03 | 7.98E-03 | 2.21E-03 | 6.96E-03 | 3.50E-03 |
| | | P-value | | | | | | * | | | | | * | * |
| | 5 mM | Mean | 1.33E-01 | 1.76E-01 | 1.81E-01 | 1.11E-01 | 1.41E-01 | 1.72E-01 | 7.85E-02 | 1.12E-01 | 1.43E-01 | 7.04E-02 | 1.40E-01 | 1.35E-01 |
| | | SE | 7.60E-03 | 1.11E-02 | 1.01E-02 | 6.02E-03 | 1.01E-02 | 9.96E-03 | 3.57E-03 | 5.16E-03 | 6.96E-03 | 3.78E-03 | 8.90E-03 | 7.73E-03 |
| | | P-value | | * | * | | | * | | * | * | | * | * |
| | 25 mM | Mean | 1.15E-01 | 2.56E-01 | 3.44E-01 | 1.24E-01 | 2.26E-01 | 4.11E-01 | 7.39E-02 | 1.66E-01 | 2.12E-01 | 5.48E-02 | 1.57E-01 | 1.15E-01 |
| | | SE | 5.56E-03 | 5.37E-03 | 3.69E-02 | 6.73E-03 | 3.68E-03 | 4.32E-02 | 2.30E-03 | 4.21E-03 | 2.01E-02 | 2.02E-03 | 4.74E-03 | 4.22E-03 |
| | | P-value | | * | * | | * | * | | * | * | | * | * |
| | 50 mM | Mean | 1.24E-01 | 2.26E-01 | 5.77E-01 | 1.06E-01 | 1.90E-01 | 6.49E-01 | 7.13E-02 | 1.45E-01 | 4.00E-01 | 6.53E-02 | 1.39E-01 | 1.06E-01 |
| | | SE | 4.68E-03 | 5.83E-03 | 3.92E-02 | 3.44E-03 | 1.08E-02 | 3.89E-02 | 4.07E-03 | 3.62E-03 | 4.37E-02 | 4.00E-03 | 4.37E-03 | 5.70E-03 |
| | | P-value | | * | * | | * | * | | * | * | | * | * |

| | | | Decorrelation, 20 ms | | | | | | | | | | | |
|---|---|---|---|---|---|---|---|---|---|---|---|---|---|---|
| | | | Whole | | | Shell | | | Body | | | Core | | |
| | | | Pre-t | 12 hr | 24 hr | Pre-t | 12 hr | 24 hr | Pre-t | 12 hr | 24 hr | Pre-t | 12 hr | 24 hr |
| Oligomycin A | | Mean | 2.98E-08 | 3.33E-08 | 4.91E-08 | 2.76E-08 | 3.10E-08 | 4.96E-08 | 3.19E-08 | 3.55E-08 | 4.99E-08 | 3.24E-08 | 3.59E-08 | 4.44E-08 |
| | | SE | 4.87E-10 | 5.57E-10 | 1.38E-09 | 2.85E-10 | 4.04E-10 | 1.48E-09 | 6.67E-10 | 7.09E-10 | 1.49E-09 | 7.68E-10 | 7.66E-10 | 9.00E-10 |
| | 0 µM | P-value | | * | * | | * | * | | * | * | | * | * |
| | | Mean | 3.50E-08 | 7.94E-08 | 7.42E-08 | 3.15E-08 | 7.35E-08 | 7.00E-08 | 3.85E-08 | 8.61E-08 | 8.24E-08 | 3.82E-08 | 8.29E-08 | 6.66E-08 |
| | | SE | 2.76E-10 | 4.19E-09 | 2.25E-09 | 1.97E-10 | 3.26E-09 | 1.61E-09 | 3.79E-10 | 5.29E-09 | 3.18E-09 | 4.04E-10 | 5.09E-09 | 2.34E-09 |
| | 1 µM | P-value | | * | * | | * | * | | * | * | | * | * |
| | | Mean | 2.92E-08 | 6.64E-08 | 6.95E-08 | 2.70E-08 | 5.86E-08 | 6.51E-08 | 3.13E-08 | 7.32E-08 | 7.50E-08 | 3.17E-08 | 7.70E-08 | 7.06E-08 |
| | | SE | 3.41E-10 | 2.08E-09 | 2.81E-09 | 2.03E-10 | 1.60E-09 | 2.15E-09 | 4.90E-10 | 2.54E-09 | 3.72E-09 | 5.55E-10 | 2.91E-09 | 3.01E-09 |
| | 5 µM | P-value | | * | * | | * | * | | * | * | | * | * |
| | | Mean | 3.73E-08 | 1.04E-07 | 7.05E-08 | 3.42E-08 | 1.10E-07 | 6.58E-08 | 4.02E-08 | 1.00E-07 | 7.76E-08 | 4.09E-08 | 8.70E-08 | 6.83E-08 |
| | | SE | 5.88E-10 | 2.77E-09 | 1.88E-09 | 4.23E-10 | 3.22E-09 | 1.60E-09 | 7.84E-10 | 2.59E-09 | 2.35E-09 | 7.02E-10 | 2.08E-09 | 1.79E-09 |
| | 10 µM | P-value | | * | * | | * | * | | * | * | | * | * |
| 2-Deoxy-D-Glucose (2-DG) | | Mean | 3.31E-08 | 3.21E-08 | 3.70E-08 | 2.98E-08 | 2.88E-08 | 3.46E-08 | 3.62E-08 | 3.51E-08 | 3.96E-08 | 3.73E-08 | 3.64E-08 | 3.90E-08 |
| | | SE | 4.19E-10 | 7.25E-10 | 9.25E-10 | 2.31E-10 | 4.33E-10 | 9.69E-10 | 6.05E-10 | 9.98E-10 | 1.01E-09 | 6.64E-10 | 1.14E-09 | 7.52E-10 |
| | 0 mM | P-value | | | * | | | * | | | | | | |
| | | Mean | 3.42E-08 | 3.78E-08 | 4.97E-08 | 3.05E-08 | 3.28E-08 | 4.45E-08 | 3.76E-08 | 4.15E-08 | 5.36E-08 | 3.86E-08 | 4.67E-08 | 5.84E-08 |
| | | SE | 6.97E-10 | 1.04E-09 | 1.62E-09 | 4.04E-10 | 5.84E-10 | 1.16E-09 | 9.94E-10 | 1.39E-09 | 2.02E-09 | 1.10E-09 | 1.92E-09 | 2.75E-09 |
| | 5 mM | P-value | | * | * | | * | * | | * | * | | * | * |
| | | Mean | 3.27E-08 | 4.92E-08 | 5.66E-08 | 3.04E-08 | 4.02E-08 | 5.92E-08 | 3.50E-08 | 5.51E-08 | 5.47E-08 | 3.54E-08 | 6.72E-08 | 5.14E-08 |
| | | SE | 6.20E-10 | 6.15E-10 | 1.95E-09 | 4.50E-10 | 4.18E-10 | 2.66E-09 | 7.84E-10 | 8.11E-10 | 1.44E-09 | 8.32E-10 | 1.30E-09 | 1.03E-09 |
| | 25 mM | P-value | | * | * | | * | * | | * | * | | * | * |
| | | Mean | 3.43E-08 | 5.46E-08 | 6.36E-08 | 3.09E-08 | 4.61E-08 | 7.09E-08 | 3.78E-08 | 5.99E-08 | 5.93E-08 | 3.72E-08 | 7.25E-08 | 4.75E-08 |
| | | SE | 3.91E-10 | 9.39E-10 | 2.80E-09 | 2.59E-10 | 1.02E-09 | 3.21E-09 | 5.38E-10 | 1.04E-09 | 2.94E-09 | 5.42E-10 | 1.66E-09 | 1.24E-09 |
| | 50 mM | P-value | | * | * | | * | * | | * | * | | * | * |

| | | | Decorrelation CoV, 20 ms | | | | | | | | | | | |
|---|---|---|---|---|---|---|---|---|---|---|---|---|---|---|
| | | | Whole | | | Shell | | | Body | | | Core | | |
| | | | Pre-t | 12 hr | 24 hr | Pre-t | 12 hr | 24 hr | Pre-t | 12 hr | 24 hr | Pre-t | 12 hr | 24 hr |
| Oligomycin A | | Mean | 1.27E-01 | 1.36E-01 | 3.43E-01 | 1.32E-01 | 1.43E-01 | 4.17E-01 | 8.23E-02 | 9.66E-02 | 2.51E-01 | 5.71E-02 | 7.81E-02 | 1.12E-01 |
| | | SE | 7.06E-03 | 5.73E-03 | 2.32E-02 | 6.78E-03 | 5.93E-03 | 2.58E-02 | 3.47E-03 | 3.60E-03 | 2.11E-02 | 2.01E-03 | 2.67E-03 | 5.32E-03 |
| | 0 µM | P-value | | | * | | | * | | | * | | * | * |
| | | Mean | 1.34E-01 | 3.07E-01 | 3.26E-01 | 1.11E-01 | 3.74E-01 | 3.82E-01 | 7.31E-02 | 2.22E-01 | 2.59E-01 | 6.40E-02 | 1.77E-01 | 1.45E-01 |
| | | SE | 2.86E-03 | 1.78E-02 | 2.93E-02 | 2.44E-03 | 2.56E-02 | 3.52E-02 | 1.90E-03 | 1.19E-02 | 2.67E-02 | 2.11E-03 | 1.01E-02 | 1.15E-02 |
| | 1 µM | P-value | | * | * | | * | * | | * | * | | * | * |
| | | Mean | 1.29E-01 | 2.41E-01 | 3.28E-01 | 1.30E-01 | 2.71E-01 | 4.16E-01 | 8.71E-02 | 1.58E-01 | 2.31E-01 | 6.25E-02 | 1.62E-01 | 1.70E-01 |
| | | SE | 6.96E-03 | 9.85E-03 | 3.38E-02 | 6.82E-03 | 1.40E-02 | 4.55E-02 | 4.57E-03 | 5.46E-03 | 2.54E-02 | 3.32E-03 | 6.02E-03 | 8.52E-03 |
| | 5 µM | P-value | | * | * | | * | * | | * | * | | * | * |
| | | Mean | 1.48E-01 | 8.14E-01 | 3.61E-01 | 1.54E-01 | 9.91E-01 | 4.40E-01 | 9.86E-02 | 5.23E-01 | 2.80E-01 | 6.89E-02 | 1.71E-01 | 1.74E-01 |
| | | SE | 7.81E-03 | 3.20E-02 | 1.75E-02 | 8.72E-03 | 3.53E-02 | 2.06E-02 | 7.59E-03 | 2.86E-02 | 1.67E-02 | 4.64E-03 | 4.79E-03 | 6.97E-03 |
| | 10 µM | P-value | | * | * | | * | * | | * | * | | * | * |
| 2-Deoxy-D-Glucose (2-DG) | | Mean | 1.48E-01 | 1.56E-01 | 1.54E-01 | 1.32E-01 | 1.33E-01 | 1.59E-01 | 8.89E-02 | 1.02E-01 | 1.12E-01 | 7.18E-02 | 1.00E-01 | 1.00E-01 |
| | | SE | 4.74E-03 | 8.90E-03 | 1.03E-02 | 5.50E-03 | 7.07E-03 | 1.38E-02 | 3.85E-03 | 5.89E-03 | 9.37E-03 | 2.37E-03 | 7.43E-03 | 4.27E-03 |
| | 0 mM | P-value | | | | | | | | | | | * | * |
| | | Mean | 1.51E-01 | 2.04E-01 | 2.09E-01 | 1.28E-01 | 1.64E-01 | 1.94E-01 | 8.61E-02 | 1.29E-01 | 1.63E-01 | 7.79E-02 | 1.59E-01 | 1.54E-01 |
| | | SE | 8.38E-03 | 1.24E-02 | 1.17E-02 | 7.05E-03 | 1.18E-02 | 1.14E-02 | 3.40E-03 | 5.50E-03 | 7.93E-03 | 4.56E-03 | 1.01E-02 | 8.01E-03 |
| | 5 mM | P-value | | * | * | | | * | | * | * | | * | * |
| | | Mean | 1.32E-01 | 2.95E-01 | 3.91E-01 | 1.42E-01 | 2.65E-01 | 4.70E-01 | 8.34E-02 | 1.89E-01 | 2.34E-01 | 6.24E-02 | 1.72E-01 | 1.29E-01 |
| | | SE | 6.23E-03 | 6.30E-03 | 4.15E-02 | 7.68E-03 | 4.87E-03 | 4.88E-02 | 2.55E-03 | 4.75E-03 | 2.19E-02 | 2.45E-03 | 5.15E-03 | 4.48E-03 |
| | 25 mM | P-value | | * | * | | * | * | | * | * | | * | * |
| | | Mean | 1.37E-01 | 2.62E-01 | 6.64E-01 | 1.20E-01 | 2.20E-01 | 7.48E-01 | 7.46E-02 | 1.62E-01 | 4.52E-01 | 6.74E-02 | 1.55E-01 | 1.19E-01 |
| | | SE | 4.08E-03 | 6.84E-03 | 4.14E-02 | 3.49E-03 | 1.35E-02 | 4.07E-02 | 3.26E-03 | 3.92E-03 | 4.72E-02 | 2.41E-03 | 4.72E-03 | 6.21E-03 |
| | 50 mM | P-value | | * | * | | * | * | | * | * | | * | * |

| | | | Decorrelation, 30 ms | | | | | | | | | | | |
|---|---|---|---|---|---|---|---|---|---|---|---|---|---|---|
| | | | Whole | | | Shell | | | Body | | | Core | | |
| | | | Pre-t | 12 hr | 24 hr | Pre-t | 12 hr | 24 hr | Pre-t | 12 hr | 24 hr | Pre-t | 12 hr | 24 hr |
| Oligomycin A | | Mean | 2.64E-08 | 2.93E-08 | 4.38E-08 | 2.40E-08 | 2.68E-08 | 4.41E-08 | 2.87E-08 | 3.16E-08 | 4.47E-08 | 2.96E-08 | 3.21E-08 | 3.99E-08 |
| | | SE | 5.24E-10 | 5.72E-10 | 1.29E-09 | 3.05E-10 | 4.01E-10 | 1.36E-09 | 7.14E-10 | 7.40E-10 | 1.39E-09 | 8.46E-10 | 7.93E-10 | 8.95E-10 |
| | 0 µM | P-value | | * | * | | * | * | | | * | | | * |
| | | Mean | 3.10E-08 | 7.41E-08 | 6.79E-08 | 2.74E-08 | 6.65E-08 | 6.31E-08 | 3.47E-08 | 8.19E-08 | 7.63E-08 | 3.46E-08 | 8.11E-08 | 6.20E-08 |
| | | SE | 2.77E-10 | 3.92E-09 | 2.15E-09 | 1.82E-10 | 2.91E-09 | 1.51E-09 | 3.81E-10 | 5.05E-09 | 3.04E-09 | 5.02E-10 | 5.02E-09 | 2.34E-09 |
| | 1 µM | P-value | | * | * | | * | * | | * | * | | * | * |
| | | Mean | 2.54E-08 | 6.04E-08 | 6.30E-08 | 2.32E-08 | 5.24E-08 | 5.84E-08 | 2.74E-08 | 6.73E-08 | 6.84E-08 | 2.79E-08 | 7.15E-08 | 6.47E-08 |
| | | SE | 3.20E-10 | 1.99E-09 | 2.63E-09 | 2.02E-10 | 1.48E-09 | 2.00E-09 | 4.52E-10 | 2.45E-09 | 3.48E-09 | 5.15E-10 | 2.88E-09 | 2.88E-09 |
| | 5 µM | P-value | | * | * | | * | * | | * | * | | * | * |
| | | Mean | 3.26E-08 | 9.51E-08 | 6.40E-08 | 2.95E-08 | 1.01E-07 | 5.91E-08 | 3.56E-08 | 9.25E-08 | 7.08E-08 | 3.62E-08 | 8.10E-08 | 6.26E-08 |
| | | SE | 5.90E-10 | 2.59E-09 | 1.77E-09 | 4.19E-10 | 3.01E-09 | 1.48E-09 | 7.86E-10 | 2.43E-09 | 2.25E-09 | 7.26E-10 | 1.93E-09 | 1.68E-09 |
| | 10 µM | P-value | | * | * | | * | * | | * | * | | * | * |
| 2-Deoxy-D-Glucose (2-DG) | | Mean | 2.91E-08 | 2.82E-08 | 3.25E-08 | 2.57E-08 | 2.49E-08 | 3.00E-08 | 3.22E-08 | 3.13E-08 | 3.50E-08 | 3.33E-08 | 3.25E-08 | 3.48E-08 |
| | | SE | 4.05E-10 | 6.89E-10 | 8.76E-10 | 2.27E-10 | 4.07E-10 | 8.95E-10 | 5.85E-10 | 9.50E-10 | 9.79E-10 | 6.56E-10 | 1.11E-09 | 7.73E-10 |
| | 0 mM | P-value | | | * | | | * | | | | | | |
| | | Mean | 2.99E-08 | 3.37E-08 | 4.49E-08 | 2.63E-08 | 2.87E-08 | 3.95E-08 | 3.33E-08 | 3.74E-08 | 4.91E-08 | 3.43E-08 | 4.26E-08 | 5.43E-08 |
| | | SE | 6.82E-10 | 1.02E-09 | 1.58E-09 | 3.91E-10 | 5.67E-10 | 1.11E-09 | 9.68E-10 | 1.38E-09 | 1.98E-09 | 1.11E-09 | 1.90E-09 | 2.72E-09 |
| | 5 mM | P-value | | * | * | | * | * | | * | * | | * | * |
| | | Mean | 2.85E-08 | 4.63E-08 | 5.11E-08 | 2.62E-08 | 3.68E-08 | 5.30E-08 | 3.07E-08 | 5.28E-08 | 4.99E-08 | 3.12E-08 | 6.49E-08 | 4.74E-08 |
| | | SE | 6.23E-10 | 9.55E-10 | 1.86E-09 | 4.65E-10 | 6.50E-10 | 2.45E-09 | 7.76E-10 | 1.24E-09 | 1.43E-09 | 8.25E-10 | 1.66E-09 | 1.10E-09 |
| | 25 mM | P-value | | * | * | | * | * | | * | * | | * | * |
| | | Mean | 3.01E-08 | 5.02E-08 | 5.73E-08 | 2.69E-08 | 4.14E-08 | 6.36E-08 | 3.36E-08 | 5.58E-08 | 5.39E-08 | 3.29E-08 | 6.84E-08 | 4.28E-08 |
| | | SE | 3.77E-10 | 9.34E-10 | 2.58E-09 | 2.55E-10 | 9.70E-10 | 2.93E-09 | 5.10E-10 | 1.06E-09 | 2.72E-09 | 5.28E-10 | 1.67E-09 | 1.17E-09 |
| | 50 mM | P-value | | * | * | | * | * | | * | * | | * | * |

| | | | Decorrelation CoV, 30 ms | | | | | | | | | | | |
|---|---|---|---|---|---|---|---|---|---|---|---|---|---|---|
| | | | Whole | | | Shell | | | Body | | | Core | | |
| | | | Pre-t | 12 hr | 24 hr | Pre-t | 12 hr | 24 hr | Pre-t | 12 hr | 24 hr | Pre-t | 12 hr | 24 hr |
| Oligomycin A | 0 µM | Mean | 1.59E-01 | 1.63E-01 | 3.70E-01 | 1.63E-01 | 1.70E-01 | 4.52E-01 | 1.07E-01 | 1.18E-01 | 2.71E-01 | 7.92E-02 | 9.94E-02 | 1.28E-01 |
| | | SE | 7.74E-03 | 6.31E-03 | 2.39E-02 | 7.28E-03 | 6.39E-03 | 2.72E-02 | 3.81E-03 | 3.87E-03 | 2.07E-02 | 1.86E-03 | 3.05E-03 | 5.24E-03 |
| | | P-value | | | * | | | * | | | * | | * | * |
| | 1 µM | Mean | 1.62E-01 | 3.23E-01 | 3.47E-01 | 1.35E-01 | 3.94E-01 | 4.12E-01 | 9.66E-02 | 2.26E-01 | 2.70E-01 | 8.45E-02 | 1.86E-01 | 1.56E-01 |
| | | SE | 3.30E-03 | 1.71E-02 | 2.95E-02 | 2.77E-03 | 2.60E-02 | 3.57E-02 | 1.62E-03 | 1.11E-02 | 2.68E-02 | 2.11E-03 | 9.60E-03 | 1.12E-02 |
| | | P-value | | * | * | | * | * | | * | * | | * | * |
| | 5 µM | Mean | 1.55E-01 | 2.63E-01 | 3.48E-01 | 1.55E-01 | 2.95E-01 | 4.43E-01 | 1.10E-01 | 1.72E-01 | 2.44E-01 | 8.26E-02 | 1.70E-01 | 1.84E-01 |
| | | SE | 7.13E-03 | 1.01E-02 | 3.42E-02 | 7.77E-03 | 1.47E-02 | 4.67E-02 | 4.84E-03 | 4.83E-03 | 2.55E-02 | 3.80E-03 | 6.38E-03 | 9.09E-03 |
| | | P-value | | * | * | | * | * | | * | * | | * | * |
| | 10 µM | Mean | 1.74E-01 | 8.54E-01 | 3.79E-01 | 1.81E-01 | 1.05E+00 | 4.63E-01 | 1.21E-01 | 5.33E-01 | 2.94E-01 | 8.75E-02 | 1.83E-01 | 1.90E-01 |
| | | SE | 8.48E-03 | 3.41E-02 | 1.80E-02 | 9.38E-03 | 3.86E-02 | 2.15E-02 | 8.10E-03 | 2.86E-02 | 1.70E-02 | 4.32E-03 | 4.46E-03 | 6.74E-03 |
| | | P-value | | * | * | | * | * | | * | * | | * | * |
| 2-Deoxy-D-Glucose (2-DG) | 0 mM | Mean | 1.75E-01 | 1.84E-01 | 1.79E-01 | 1.59E-01 | 1.59E-01 | 1.82E-01 | 1.12E-01 | 1.25E-01 | 1.33E-01 | 9.42E-02 | 1.21E-01 | 1.22E-01 |
| | | SE | 5.44E-03 | 9.28E-03 | 9.99E-03 | 6.53E-03 | 7.47E-03 | 1.37E-02 | 4.14E-03 | 6.21E-03 | 9.19E-03 | 3.16E-03 | 7.07E-03 | 4.20E-03 |
| | | P-value | | | | | | | | | | | | * |
| | 5 mM | Mean | 1.74E-01 | 2.33E-01 | 2.36E-01 | 1.51E-01 | 1.90E-01 | 2.16E-01 | 1.06E-01 | 1.54E-01 | 1.83E-01 | 1.01E-01 | 1.80E-01 | 1.75E-01 |
| | | SE | 8.73E-03 | 1.30E-02 | 1.18E-02 | 7.48E-03 | 1.25E-02 | 1.18E-02 | 3.26E-03 | 5.95E-03 | 7.38E-03 | 4.64E-03 | 9.94E-03 | 7.94E-03 |
| | | P-value | | * | * | | | * | | * | * | | * | * |
| | 25 mM | Mean | 1.56E-01 | 3.29E-01 | 4.12E-01 | 1.68E-01 | 3.07E-01 | 5.01E-01 | 1.06E-01 | 2.10E-01 | 2.46E-01 | 8.44E-02 | 1.82E-01 | 1.46E-01 |
| | | SE | 6.20E-03 | 6.97E-03 | 4.13E-02 | 7.79E-03 | 6.99E-03 | 5.01E-02 | 2.63E-03 | 4.81E-03 | 2.10E-02 | 3.19E-03 | 4.96E-03 | 5.46E-03 |
| | | P-value | | * | * | | * | * | | * | * | | * | * |
| | 50 mM | Mean | 1.59E-01 | 2.90E-01 | 6.96E-01 | 1.42E-01 | 2.44E-01 | 7.91E-01 | 9.57E-02 | 1.79E-01 | 4.72E-01 | 8.98E-02 | 1.71E-01 | 1.35E-01 |
| | | SE | 3.78E-03 | 6.94E-03 | 4.12E-02 | 3.37E-03 | 1.42E-02 | 4.09E-02 | 2.95E-03 | 3.74E-03 | 4.58E-02 | 3.03E-03 | 4.72E-03 | 6.16E-03 |
| | | P-value | | * | * | | * | * | | * | * | | * | * |

| | | | ND, 10 ms (Fitting) | | | ND, 10 ms (Spheroid Fitting) | | | | | | | | |
|---|---|---|---|---|---|---|---|---|---|---|---|---|---|---|
| | | | - | | | Fca | | | FCb | | | FCc | | |
| | | | Pre-t | 12 hr | 24 hr | Pre-t | 12 hr | 24 hr | Pre-t | 12 hr | 24 hr | Pre-t | 12 hr | 24 hr |
| Oligomycin A | 0 µM | Mean | 3.16E-01 | 3.38E-01 | 3.56E-01 | 8.17E-01 | 9.15E-01 | 2.08E+01 | 2.27E+01 | 2.33E+01 | 1.10E+03 | 2.35E+00 | 2.63E+00 | 2.67E+00 |
| | | SE | 5.16E-03 | 3.53E-03 | 5.21E-03 | 6.18E-02 | 6.24E-02 | 8.47E+00 | 1.71E+00 | 2.09E+00 | 4.60E+02 | 7.82E-03 | 2.13E-02 | 1.96E-01 |
| | | P-value | | * | * | | | * | | | * | | * | * |
| | 1 µM | Mean | 1.89E-01 | 4.31E-01 | 4.02E-01 | 1.11E+00 | 7.68E+00 | 2.88E+01 | 3.91E+01 | 1.20E+02 | 5.89E+02 | 2.69E+00 | -5.01E-01 | 2.14E+00 |
| | | SE | 1.76E-03 | 8.21E-03 | 3.97E-03 | 3.28E-02 | 1.12E+00 | 2.36E+01 | 1.79E+00 | 1.11E+02 | 5.80E+02 | 1.12E-02 | 8.26E-01 | 2.44E-01 |
| | | P-value | | * | * | | * | * | | * | * | | * | * |
| | 5 µM | Mean | 3.33E-01 | 4.61E-01 | 4.56E-01 | 8.06E-01 | 4.32E+00 | 5.19E+00 | 2.22E+01 | 7.85E+00 | 6.59E+00 | 2.32E+00 | 2.10E+00 | 1.56E+00 |
| | | SE | 6.51E-03 | 4.91E-03 | 3.35E-03 | 5.06E-02 | 4.57E-01 | 3.92E-01 | 2.29E+00 | 5.46E-01 | 5.99E-01 | 1.12E-02 | 3.18E-01 | 1.18E-01 |
| | | P-value | | * | * | | * | * | | * | * | | | * |
| | 10 µM | Mean | 2.95E-01 | 5.12E-01 | 3.79E-01 | 1.19E+00 | 3.18E+02 | 1.61E+02 | 3.39E+01 | 4.35E+03 | 2.98E+03 | 2.85E+00 | 1.34E+00 | 2.97E+00 |
| | | SE | 3.30E-03 | 6.14E-03 | 2.14E-03 | 6.30E-02 | 1.17E+02 | 6.60E+01 | 1.65E+00 | 1.36E+03 | 1.23E+03 | 8.28E-03 | 8.37E-01 | 2.21E-01 |
| | | P-value | | * | * | | * | * | | | * | | | |
| 2-Deoxy-D-Glucose (2-DG) | 0 mM | Mean | 2.45E-01 | 3.17E-01 | 3.29E-01 | 1.20E+00 | 1.10E+00 | 5.20E-01 | 4.02E+01 | 2.89E+01 | 1.76E+01 | 2.50E+00 | 2.46E+00 | 3.26E+00 |
| | | SE | 1.59E-02 | 1.72E-02 | 1.46E-02 | 4.94E-02 | 8.24E-02 | 4.79E-01 | 2.13E+00 | 1.66E+00 | 1.94E+00 | 1.22E-02 | 2.25E-02 | 4.96E-01 |
| | | P-value | | | | | | * | | * | * | | | * |
| | 5 mM | Mean | 2.25E-01 | 2.18E-01 | 2.97E-01 | 2.59E+00 | 2.95E+00 | 2.11E+00 | 1.50E+02 | 8.13E+01 | 3.80E+01 | 2.57E+00 | 2.53E+00 | 3.26E+00 |
| | | SE | 1.50E-02 | 1.29E-02 | 1.97E-02 | 1.25E+00 | 1.02E+00 | 2.02E-01 | 1.04E+02 | 3.31E+01 | 7.29E+00 | 1.32E-02 | 2.14E-02 | 1.33E-01 |
| | | P-value | | | | | * | * | | | | | | * |
| | 25 mM | Mean | 3.09E-01 | 2.45E-01 | 3.71E-01 | 1.04E+00 | 3.36E+00 | 2.15E+00 | 3.10E+01 | 5.76E+01 | 4.04E+00 | 2.51E+00 | 2.66E+00 | 3.09E+00 |
| | | SE | 1.99E-02 | 5.90E-03 | 8.62E-03 | 6.81E-02 | 1.14E-01 | 9.21E-01 | 1.72E+00 | 2.21E+00 | 9.56E-01 | 5.53E-03 | 1.89E-02 | 8.72E-01 |
| | | P-value | | | | | * | | | * | * | | * | |
| | 50 mM | Mean | 1.51E-01 | 1.97E-01 | 3.60E-01 | 1.32E+00 | 3.06E+01 | 4.85E+02 | 4.61E+01 | 9.36E+02 | 3.57E+03 | 2.53E+00 | 3.41E+00 | -2.14E+02 |
| | | SE | 1.86E-03 | 2.40E-03 | 1.10E-02 | 7.43E-02 | 1.52E+01 | 2.28E+02 | 4.28E+00 | 4.77E+02 | 1.03E+03 | 2.54E-02 | 1.11E-01 | 2.09E+02 |
| | | P-value | | * | * | | * | | | * | | | * | * |

| | | | ND, 10 ms (Spheroid Fitting) | | | | | | | | | | | |
|---|---|---|---|---|---|---|---|---|---|---|---|---|---|---|
| | | | FCd1 | | | FCd2 | | | FCd3 | | | FCd4 | | |
| | | | Pre-t | 12 hr | 24 hr | Pre-t | 12 hr | 24 hr | Pre-t | 12 hr | 24 hr | Pre-t | 12 hr | 24 hr |
| Oligomycin A | 0 µM | Mean | 3.00E+00 | 3.34E+00 | 4.68E+00 | 3.14E+00 | 3.50E+00 | 4.77E+00 | 3.17E+00 | 3.53E+00 | 4.86E+00 | 3.17E+00 | 3.54E+00 | 4.94E+00 |
| | | SE | 3.96E-02 | 4.95E-02 | 1.28E-01 | 5.98E-02 | 6.80E-02 | 1.36E-01 | 6.48E-02 | 7.45E-02 | 1.52E-01 | 6.59E-02 | 7.66E-02 | 1.74E-01 |
| | | P-value | | * | * | | * | * | | * | * | | * | * |
| | 1 µM | Mean | 3.46E+00 | 7.33E+00 | 7.13E+00 | 3.72E+00 | 7.34E+00 | 7.24E+00 | 3.78E+00 | 7.34E+00 | 7.33E+00 | 3.79E+00 | 7.33E+00 | 7.42E+00 |
| | | SE | 2.18E-02 | 4.18E-01 | 2.50E-01 | 2.78E-02 | 4.18E-01 | 2.42E-01 | 3.10E-02 | 4.18E-01 | 2.63E-01 | 3.18E-02 | 4.19E-01 | 3.12E-01 |
| | | P-value | | * | * | | * | * | | * | * | | * | * |
| | 5 µM | Mean | 2.99E+00 | 6.41E+00 | 6.73E+00 | 3.11E+00 | 6.42E+00 | 6.74E+00 | 3.12E+00 | 6.42E+00 | 6.74E+00 | 3.13E+00 | 6.42E+00 | 6.74E+00 |
| | | SE | 3.00E-02 | 2.09E-01 | 3.15E-01 | 4.82E-02 | 2.09E-01 | 3.22E-01 | 5.26E-02 | 2.09E-01 | 3.22E-01 | 5.35E-02 | 2.09E-01 | 3.22E-01 |
| | | P-value | | * | * | | * | * | | * | * | | * | * |
| | 10 µM | Mean | 3.75E+00 | 9.44E+00 | 6.85E+00 | 3.98E+00 | 1.02E+01 | 7.38E+00 | 4.02E+00 | 1.10E+01 | 7.82E+00 | 4.03E+00 | 1.17E+01 | 8.22E+00 |
| | | SE | 5.18E-02 | 2.54E-01 | 2.02E-01 | 6.28E-02 | 3.16E-01 | 2.30E-01 | 6.50E-02 | 5.08E-01 | 3.28E-01 | 6.54E-02 | 7.36E-01 | 4.56E-01 |
| | | P-value | | * | * | | * | * | | * | * | | * | * |
| 2-Deoxy-D-Glucose (2-DG) | 0 mM | Mean | 3.23E+00 | 3.26E+00 | 3.68E+00 | 3.55E+00 | 3.49E+00 | 3.77E+00 | 3.66E+00 | 3.54E+00 | 3.78E+00 | 3.69E+00 | 3.55E+00 | 3.78E+00 |
| | | SE | 2.88E-02 | 6.29E-02 | 7.61E-02 | 4.19E-02 | 8.52E-02 | 7.49E-02 | 4.98E-02 | 9.27E-02 | 7.51E-02 | 5.37E-02 | 9.51E-02 | 7.51E-02 |
| | | P-value | | | * | | | | | | | | | |
| | 5 mM | Mean | 3.38E+00 | 3.69E+00 | 4.71E+00 | 3.73E+00 | 4.22E+00 | 5.09E+00 | 3.86E+00 | 4.44E+00 | 5.24E+00 | 3.91E+00 | 4.55E+00 | 5.31E+00 |
| | | SE | 4.93E-02 | 5.82E-02 | 1.30E-01 | 5.93E-02 | 9.30E-02 | 1.80E-01 | 6.73E-02 | 1.25E-01 | 2.11E-01 | 7.42E-02 | 1.62E-01 | 2.29E-01 |
| | | P-value | | * | * | | * | * | | | * | | * | * |
| | 25 mM | Mean | 3.32E+00 | 4.42E+00 | 5.23E+00 | 3.52E+00 | 5.38E+00 | 5.24E+00 | 3.55E+00 | 5.77E+00 | 5.24E+00 | 3.55E+00 | 5.91E+00 | 5.24E+00 |
| | | SE | 4.82E-02 | 4.02E-02 | 1.71E-01 | 6.41E-02 | 6.10E-02 | 1.70E-01 | 6.71E-02 | 8.24E-02 | 1.70E-01 | 6.76E-02 | 9.83E-02 | 1.70E-01 |
| | | P-value | | * | * | | * | * | | * | * | | * | * |
| | 50 mM | Mean | 3.36E+00 | 4.89E+00 | 5.70E+00 | 3.67E+00 | 5.87E+00 | 6.32E+00 | 3.77E+00 | 6.45E+00 | 6.95E+00 | 3.81E+00 | 6.81E+00 | 7.59E+00 |
| | | SE | 2.89E-02 | 5.31E-02 | 2.70E-01 | 5.31E-02 | 8.47E-02 | 5.11E-01 | 6.94E-02 | 1.34E-01 | 7.70E-01 | 7.87E-02 | 1.85E-01 | 1.03E+00 |
| | | P-value | | * | * | | * | * | | * | * | | * | * |

| | | | ND, 10 ms (Autocorrelation) | | | | | | | | | | | |
|---|---|---|---|---|---|---|---|---|---|---|---|---|---|---|
| | | | Decay | | | DopplerAbs | | | Doppler | | | ComplexShift | | |
| | | | Pre-t | 12 hr | 24 hr | Pre-t | 12 hr | 24 hr | Pre-t | 12 hr | 24 hr | Pre-t | 12 hr | 24 hr |
| Oligomycin A | 0 µM | Mean | 1.46E-01 | 1.54E-01 | 1.58E-01 | 3.14E+00 | 3.35E+00 | 3.15E+00 | -5.41E-03 | -4.46E-03 | -9.21E-04 | 3.07E-01 | 3.23E-01 | 3.22E-01 |
| | | SE | 1.19E-03 | 8.17E-04 | 1.49E-03 | 4.75E-02 | 3.81E-02 | 3.83E-02 | 3.47E-03 | 3.52E-03 | 2.26E-03 | 2.36E-03 | 1.73E-03 | 2.80E-03 |
| | | P-value | | * | * | | * | | | | | | * | * |
| | 1 µM | Mean | 1.21E-01 | 1.86E-01 | 1.81E-01 | 2.61E+00 | 2.97E+00 | 3.08E+00 | 1.78E-03 | -2.96E-03 | -2.01E-03 | 2.70E-01 | 3.52E-01 | 3.43E-01 |
| | | SE | 4.63E-04 | 2.29E-03 | 1.31E-03 | 3.51E-02 | 5.66E-02 | 5.02E-02 | 2.34E-03 | 3.57E-03 | 3.12E-03 | 1.72E-03 | 4.62E-03 | 3.23E-03 |
| | | P-value | | * | * | | * | * | | | | | * | * |
| | 5 µM | Mean | 1.53E-01 | 1.88E-01 | 1.86E-01 | 3.34E+00 | 3.21E+00 | 3.08E+00 | 5.15E-03 | -7.80E-04 | -1.80E-03 | 3.22E-01 | 3.52E-01 | 3.44E-01 |
| | | SE | 1.74E-03 | 1.58E-03 | 7.97E-04 | 6.28E-02 | 4.17E-02 | 4.82E-02 | 5.55E-03 | 2.92E-03 | 4.56E-03 | 3.54E-03 | 2.61E-03 | 2.26E-03 |
| | | P-value | | * | * | | * | * | | | | | * | * |
| | 10 µM | Mean | 1.40E-01 | 1.98E-01 | 1.65E-01 | 3.02E+00 | 3.23E+00 | 2.56E+00 | 5.88E-03 | 6.41E-04 | 8.72E-04 | 2.96E-01 | 3.64E-01 | 3.03E-01 |
| | | SE | 1.01E-03 | 1.64E-03 | 6.56E-04 | 4.14E-02 | 4.50E-02 | 2.74E-02 | 3.10E-03 | 2.48E-03 | 2.10E-03 | 2.42E-03 | 3.30E-03 | 1.60E-03 |
| | | P-value | | * | * | | * | * | | | | | * | |
| 2-Deoxy-D-Glucose (2-DG) | 0 mM | Mean | 1.31E-01 | 1.55E-01 | 1.56E-01 | 2.88E+00 | 3.37E+00 | 3.31E+00 | -1.15E-03 | -1.29E-03 | -6.27E-03 | 2.87E-01 | 3.27E-01 | 3.27E-01 |
| | | SE | 3.12E-03 | 2.84E-03 | 2.95E-03 | 6.78E-02 | 6.40E-02 | 8.63E-02 | 4.55E-03 | 3.08E-03 | 4.08E-03 | 4.50E-03 | 4.14E-03 | 5.64E-03 |
| | | P-value | | | * | | * | * | | | | | * | * |
| | 5 mM | Mean | 1.24E-01 | 1.21E-01 | 1.44E-01 | 2.61E+00 | 2.55E+00 | 2.84E+00 | -2.77E-03 | -6.99E-03 | 2.31E-03 | 2.69E-01 | 2.63E-01 | 2.98E-01 |
| | | SE | 3.82E-03 | 3.25E-03 | 5.42E-03 | 1.21E-01 | 1.00E-01 | 1.52E-01 | 3.03E-03 | 3.26E-03 | 2.20E-03 | 7.72E-03 | 6.04E-03 | 1.07E-02 |
| | | P-value | | | | | | | | | | | | |
| | 25 mM | Mean | 1.43E-01 | 1.24E-01 | 1.58E-01 | 3.11E+00 | 2.71E+00 | 3.12E+00 | 7.45E-04 | -9.86E-04 | 1.18E-03 | 3.02E-01 | 2.72E-01 | 3.21E-01 |
| | | SE | 5.85E-03 | 2.25E-03 | 2.31E-03 | 1.29E-01 | 7.32E-02 | 5.40E-02 | 2.92E-03 | 2.30E-03 | 3.29E-03 | 1.02E-02 | 5.04E-03 | 4.36E-03 |
| | | P-value | | | | | | | | | | | | |
| | 50 mM | Mean | 1.08E-01 | 1.18E-01 | 1.63E-01 | 2.46E+00 | 2.43E+00 | 2.99E+00 | 5.38E-04 | 8.26E-05 | -2.24E-03 | 2.52E-01 | 2.62E-01 | 3.24E-01 |
| | | SE | 7.64E-04 | 6.59E-04 | 3.21E-03 | 2.79E-02 | 3.52E-02 | 9.60E-02 | 1.55E-03 | 1.54E-03 | 2.14E-03 | 1.73E-03 | 1.70E-03 | 6.72E-03 |
| | | P-value | | * | * | | | * | | | | | | * |

| | | | ND, 10 ms (Autocorrelation) | | | | | |
|---|---|---|---|---|---|---|---|---|
| | | | 2ndDecay | | | 2ndShift | | |
| | | | Pre-t | 12 hr | 24 hr | Pre-t | 12 hr | 24 hr |
| Oligomycin A | 0 µM | Mean | -1.93E-02 | -2.04E-02 | -1.94E-02 | 2.69E-01 | 2.82E-01 | 2.85E-01 |
| | | SE | 2.54E-04 | 2.13E-04 | 2.06E-04 | 1.92E-03 | 1.23E-03 | 2.25E-03 |
| | | P-value | | * | | | * | * |
| | 1 µM | Mean | -1.52E-02 | -2.14E-02 | -2.16E-02 | 2.38E-01 | 3.16E-01 | 3.09E-01 |
| | | SE | 1.08E-04 | 2.37E-04 | 1.91E-04 | 1.17E-03 | 3.59E-03 | 2.36E-03 |
| | | P-value | | * | * | | * | * |
| | 5 µM | Mean | -2.05E-02 | -2.26E-02 | -2.23E-02 | 2.81E-01 | 3.17E-01 | 3.12E-01 |
| | | SE | 3.61E-04 | 1.68E-04 | 1.79E-04 | 2.94E-03 | 2.03E-03 | 1.59E-03 |
| | | P-value | | * | * | | * | * |
| | 10 µM | Mean | -1.83E-02 | -2.28E-02 | -2.02E-02 | 2.60E-01 | 3.30E-01 | 2.80E-01 |
| | | SE | 1.41E-04 | 1.77E-04 | 1.43E-04 | 1.81E-03 | 2.56E-03 | 1.17E-03 |
| | | P-value | | * | * | | * | * |
| 2-Deoxy-D-Glucose (2-DG) | 0 mM | Mean | -1.68E-02 | -2.02E-02 | -1.97E-02 | 2.51E-01 | 2.84E-01 | 2.86E-01 |
| | | SE | 5.03E-04 | 5.57E-04 | 3.50E-04 | 3.73E-03 | 3.39E-03 | 4.39E-03 |
| | | P-value | | | * | | * | * |
| | 5 mM | Mean | -1.63E-02 | -1.54E-02 | -1.72E-02 | 2.38E-01 | 2.36E-01 | 2.67E-01 |
| | | SE | 5.89E-04 | 4.94E-04 | 7.12E-04 | 5.75E-03 | 4.46E-03 | 8.19E-03 |
| | | P-value | | | | | | |
| | 25 mM | Mean | -1.90E-02 | -1.52E-02 | -1.91E-02 | 2.65E-01 | 2.41E-01 | 2.86E-01 |
| | | SE | 9.34E-04 | 2.94E-04 | 2.25E-04 | 8.46E-03 | 3.96E-03 | 3.42E-03 |
| | | P-value | | | | | | |
| | 50 mM | Mean | -1.36E-02 | -1.36E-02 | -1.92E-02 | 2.23E-01 | 2.36E-01 | 2.90E-01 |
| | | SE | 1.28E-04 | 1.12E-04 | 3.60E-04 | 1.33E-03 | 1.10E-03 | 4.41E-03 |
| | | P-value | | | * | | * | * |

### 4.3.2 Changes in spheroid geometry

The effects of varying concentrations of metabolism inhibitors were tracked longitudinally from pre-treatment to 12- and 24-hours post-drug administration. Neurospheroid geometry metrics of volume, surface area, and SATVR were plotted as a function of time for both oligomycin A (one technical replicate with spheroid number ns = 26, 15, 12, and 23 for 0 µM, 1 µM, 5 µM, and 10 µM treatment, respectively) and 2-DG (technical duplicates with total ns = 23, 18, 31, and 21 for 0 mM, 5 mM, 25 mM, and 50 mM treatment, respectively) (**Fig. 14**).

Oligomycin A (mitochondrial respiration inhibitor) significantly increased neurospheroid volume and surface area from pre-treatment to 12 and 24 hours after administration for drug treated groups. The 2-DG (glycolysis inhibitor) also resulted in a significant increase in volume

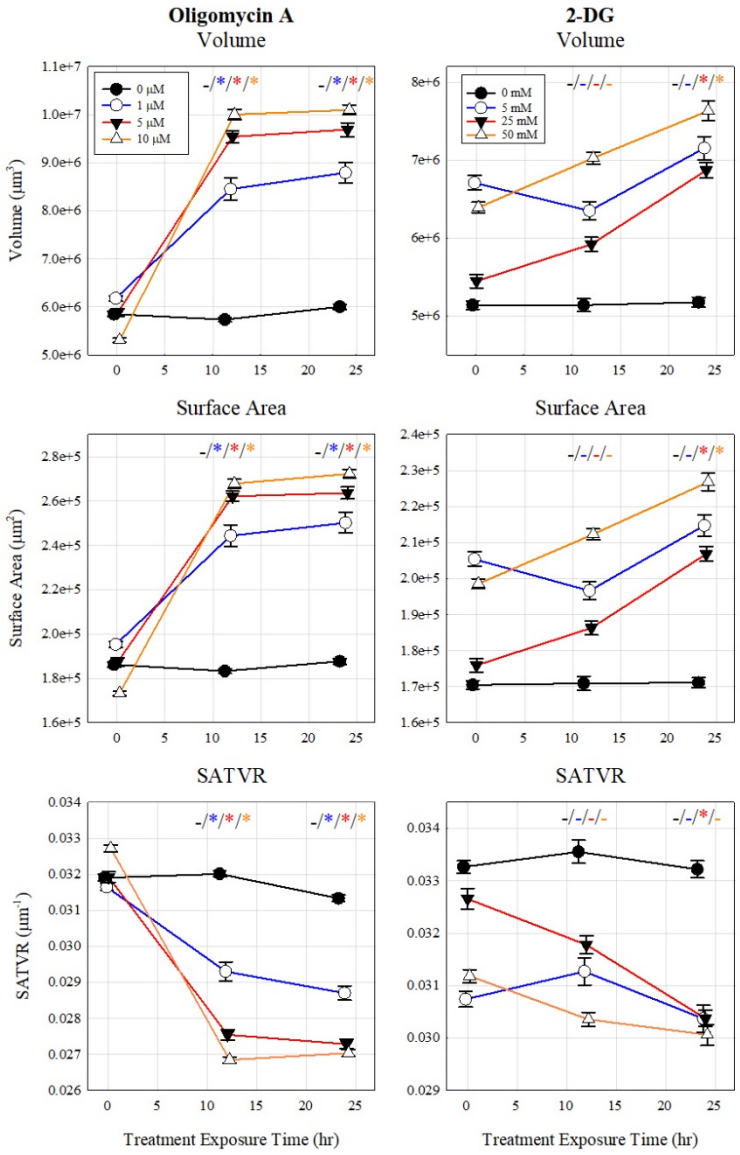


**Figure 14.** Spheroid geometry metrics over time for both metabolism inhibitors. *p≤ 0.025.

and surface area but much slower (i.e., only significant at 24 hours for higher drug treatment concentrations). The increase in volume at 24 hours was well correlated to the drug concentration. SATVR significantly decreased after 12 and 24 hours of exposure to all three oligomycin A treated groups. A decrease in SATVR was also observed longitudinally in 2-DG treated groups, but only significantly for 25 mM concentration after 24 hours of treatment exposure. The sham

group remained relatively consistent with the pre-treated measurement for volume, surface area, and SATVR.

### 4.3.3 Metabolism inhibitors increased SR

SATVR is designed to capture the surface roughness but may not be ideal for these purposes because it depends on the spheroid size and thus tends to be larger when the volume increases. It is unclear whether the decreased SATVR was due to the increased size or truly represented that the spheroid surfaces became smoother from the drug treatment. To address this limitation, we defined another metric, surface roughness (SR), as a size-independent area to volume ratio. Oligomycin A significantly increased SR for all three treated groups at 12 hours, and for 5 µM and 10 µM treated groups after 24 hours of exposure (**Fig. 15**). An increase in SR

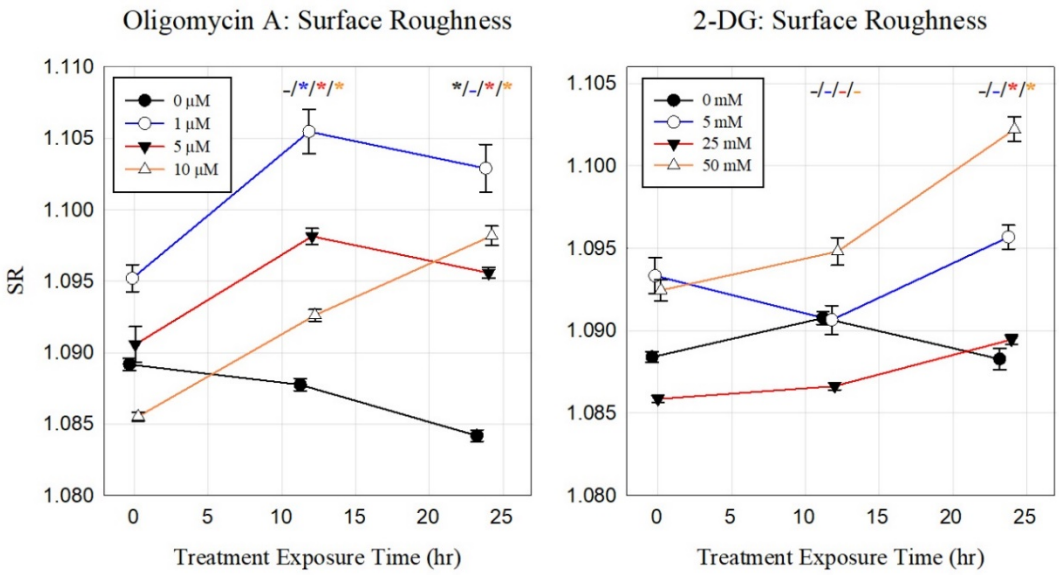


**Figure 15.** Neurospheroid SR over time for both metabolism inhibitors. *p≤ 0.025.

was also observed for neurospheroids treated with 2-DG, and significantly after 24 hours of exposure to 25 mM and 50 mM 2-DG. Inspection of the neurospheroid surface after being segmented in MATLAB provided visual evidence of this change as well as the increased volume

(**Fig. 16**). Indications of a dose-time-response relationship were observed for volume and SR, with an earlier onset of significant change for neurospheroids treated with oligomycin A (**Fig. 17**).

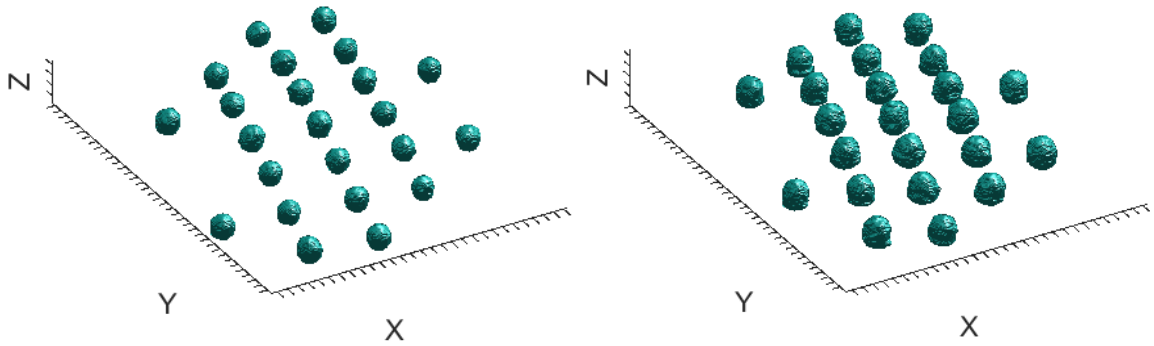


**Figure 16.** Top surface view of segmented neurospheroids acquired at pre-treatment (left) and 24 hours after exposure to 50 mM 2-DG (right).

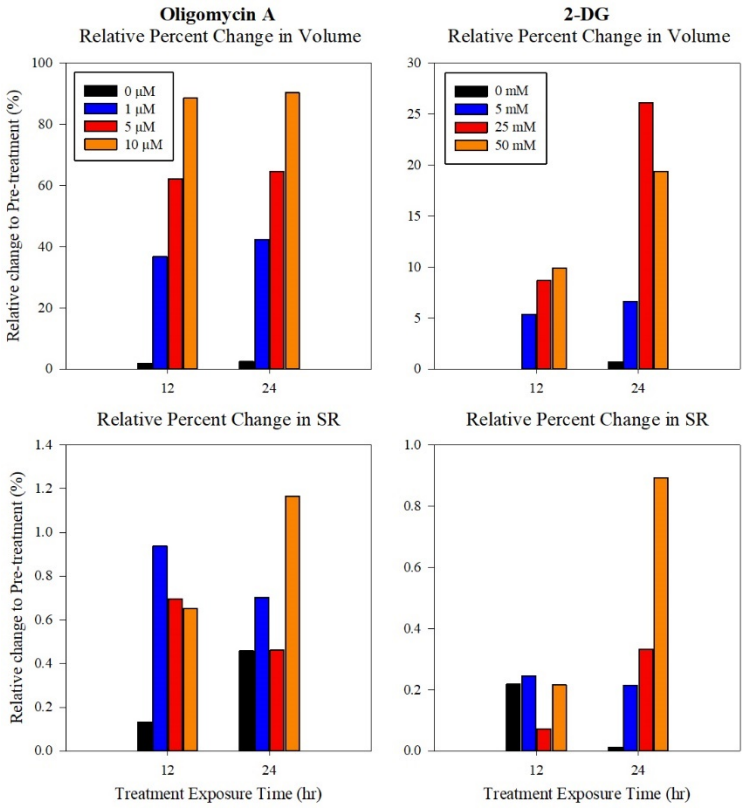


**Figure 17.** Neurospheroid volume and SR plotted as percentage change relative to pre-treatment for both metabolism inhibitors.

### 4.3.4 Diverging intensity signal

The mean intensity signal varied over time and for varying concentrations of both drugs (**Fig. 18**). A significant decrease was observed after 12 hours of exposure to 5 µM oligomycin A. Similarly, there was a significant decrease in intensity after 24 hours of exposure to 5 mM and 50 mM 2-DG. A plot of the relative change in intensity demonstrated a decrease in intensity after 24 hours for 1 µM and 10 µm oligomycin A, but interestingly, an increase for the sham and 5 µM

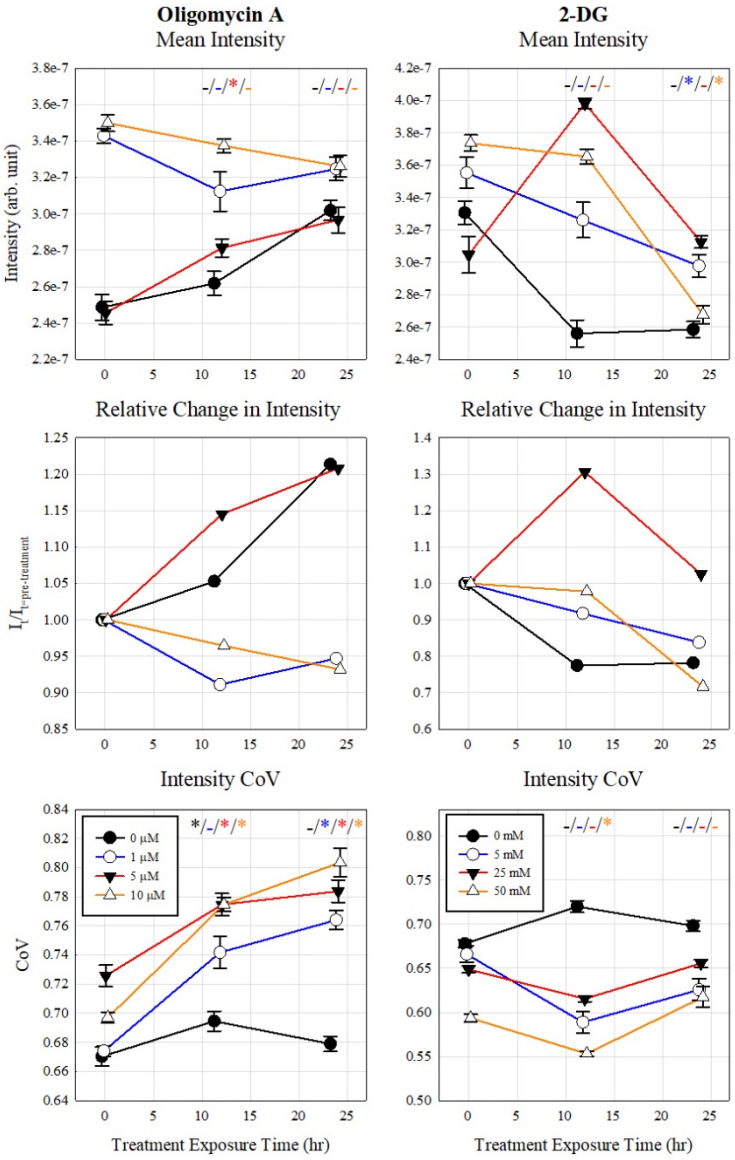


**Figure 18.** OCT intensity signal plotted as the mean value, relative change, and CoV over time for both metabolism inhibitors. *p≤ 0.025.

treated groups. Similarly, intensity decreased for the lower and higher concentration of 2-DG; however, the middle concentration (25 mM) peaked at 12 hours before returning back to a near pre-treatment level of intensity at 24 hours.

The coefficient of variation (CoV) significantly increased for neurospheroids treated with oligomycin A, demonstrating a decrease in signal homogeneity. However, the signal became more homogenous for 5 mM 2-DG after 12 hours of exposure. The aberrant signal neurospheroids treated with a mitochondrial respiration inhibitor was apparent in the dispersion of the intensity after treatment of 1 µM oligomycin A, which can also be differentiated by the distance from the surface of the spheroid (**Fig. 19**).

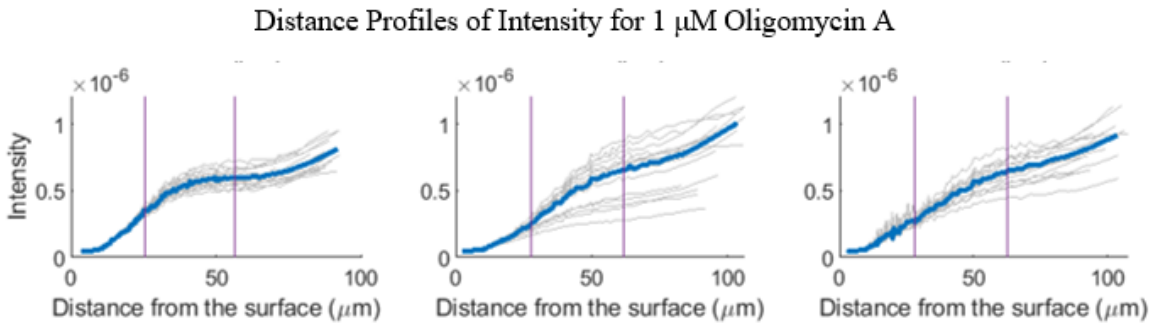


**Figure 19.** Distance profiles of the intensity signal for a single microgel of 1 µM oligomycin A, where x is the distance going inward from the surface of the spheroid and y is the intensity signal plotted for 15 spheroids (grey) and the mean intensity value of the whole gel (blue). The left, middle, and right are plots for pre-treatment, 12 hours, and 24 hours after treatment exposure, respectively.

### 4.3.5 Longitudinal increase in decorrelation

Decorrelation was assessed at three successive time points as there were four consecutive scans acquired for each B-scan. The time between scans can impact the sensitivity to which slow and fast-moving objects, as well as noise, ultimately contributed to the decorrelation. Therefore, the mean, relative change, and CoV of decorrelation was assessed for a 10 ms, 20 ms, and 30 ms B-scan delay time; however, the three decorrelation times resulted in nearly identical trends. In

this case, the time delay range had no impact on capturing a differentiated response in "slow" versus "faster" moving components within the intracellular space. For the purposes of this analysis, decorrelation at 10 ms between B-scans was used as the *representative* speckle signal for assessing neurospheroid decorrelation (**Fig. 20**).

Significant changes in decorrelation were observed for all groups with both metabolism inhibitors. A 10 ms B-scan delay was sufficient in detecting an increase in decorrelation after 12

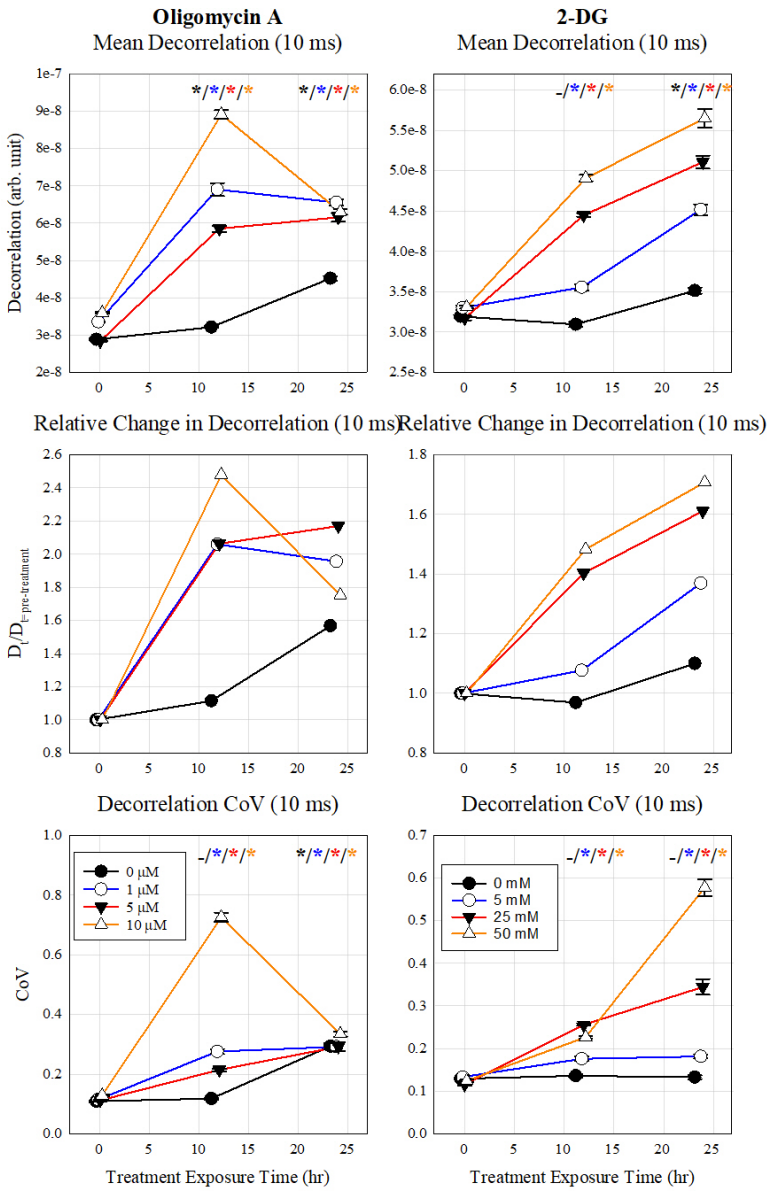


**Figure 20.** Decorrelation plotted as the mean value, relative change, and CoV over time for both metabolism inhibitors. *p≤ 0.025.

and 24 hours in both drugs, relative to pre-treatment. However, the oligomycin A treated cohort decreased after 12 hours whereas 2-DG continued to increase after 24 hours. When considering the general trend that the decorrelation tends to be larger in high-intensity signals, it was interesting to see that the decorrelation increased in all cases while the intensity only decreased in some cases (**Fig. 18**). This result suggests that the degree of intracellular motions truly became higher from both oligomycin A and 2-DG.

### 4.3.6 Neurospheroid subregions

The whole neurospheroid was sectioned off into regions based on its outer shell, body in the middle, and core in the center such that metric measurements were localized to each of the three subregions, as well as the entire spheroid.

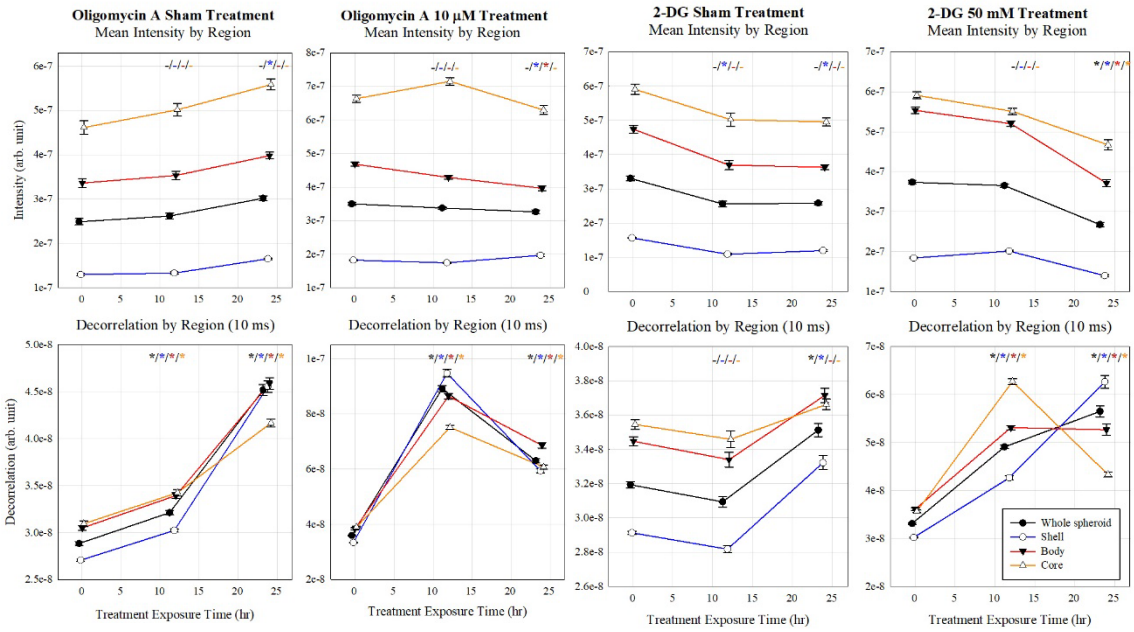


**Figure 21.** Mean OCT intensity and decorrelation (10 ms) speckle signal for 10 µM oligomycin A (left) and 50 mM 2-DG (right) by neurospheroid subregions. *p≤ 0.025.

Overall, the intensity was the highest in the core and lowest in the shell, but this region-specific trend was weaker for decorrelation. The changes for each subregion generally followed the trend of the changes in the whole spheroid for both intensity and decorrelation. However, between 12 and 24 hours of the 50 mM 2-DG group, the decorrelation of the core showed a decrease while all the other subregions increased. It is interesting to see the spheroid core exhibit an opposite response. This result can be clearly seen in the distance profile of decorrelation in **Figure 22**. The shell (short distance area) showed a large increase but the core (long distance area) decreased.

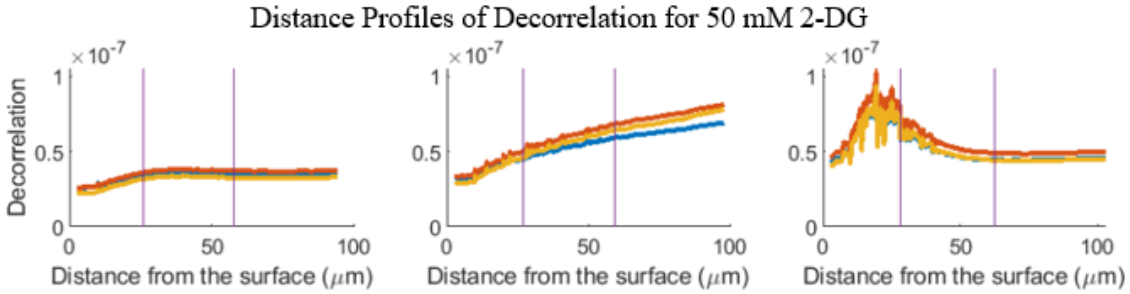


**Figure 22.** Distance profiles of decorrelation for a single microgel of 50 mM 2-DG, where x is the distance going inward from the surface of the spheroid and y is the decorrelation signal plotted for 12 spheroids at a decorrelation time of 10 ms (blue), 20 ms (orange), and 30 ms (yellow). The left, middle, and right are plots for pre-treatment, 12 hours, and 24 hours after treatment exposure, respectively.

### 4.3.7 Fitting-based normalized decorrelation reaffirms increase in dynamics

Decorrelation was mathematically decoupled from intensity to report the normalized decorrelation as a measurement that would more closely captured the true motility without any influence from the intensity signal. Since the optimal method for calculating this measurement is unknown at this point, two different approaches were used to extract the normalized decorrelation: fitting-based and autocorrelation-based. Results for each of the methodological approaches to capturing normalized decorrelation are shown in the figures below. However, given

the novelty of this parameter, the conclusiveness of the results is dependent on further investigation and understanding of the intensity-decorrelation relationship as well as how closely these mathematical approaches account for this coupling effect.

The universal fitting-based (**Fig. 23**) and fitting coefficient D1 and D2-based (**Fig. 24**) approaches to normalized decorrelation resulted in significant time-dependent changes in normalized decorrelation for both drugs. Based on the behavior observed in the decorrelation data, the fitting-based normalized decorrelation reaffirmed the longitudinal increase in decorrelation in response to both drug treatments. Additionally, the differentiated metric response was apparent in the normalized decorrelation where at 12 hours, oligomycin A treated spheroids appeared to reach a maxima while 2-DG consistently increased after 12 and 24 hours of treatment. Given that the fitting coefficients take into account the spheroids individually, the results in **Figure 24** appeared to follow a dose-time-response relationship more closely than the universal-fitting approach, with minor intra-drug differences between the two coefficients.

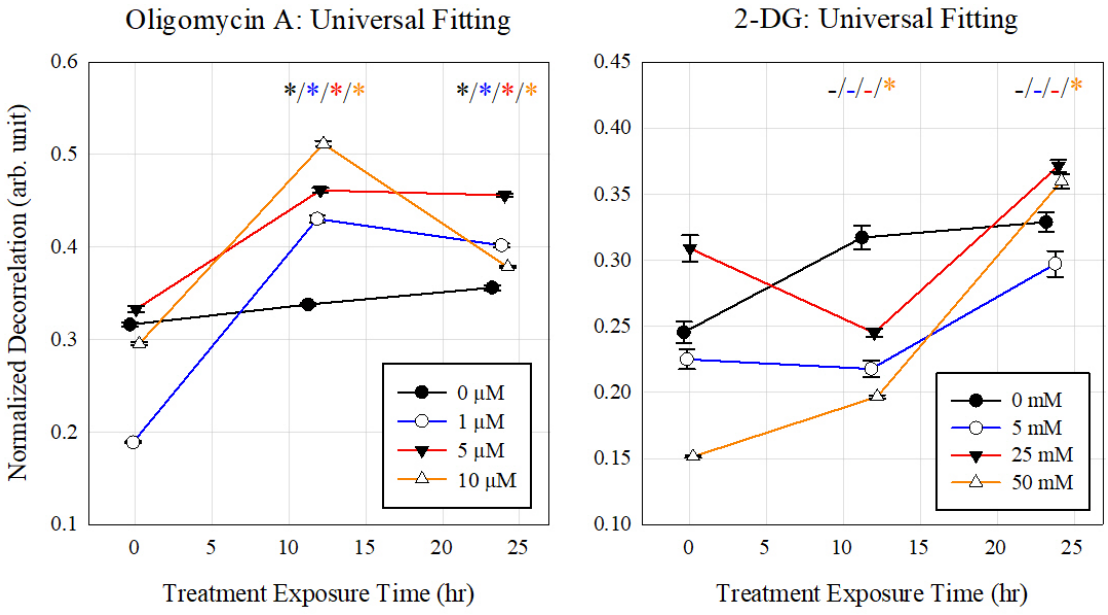


**Figure 23.** Universal fitting-based normalized decorrelation measurement plotted over time for both metabolism inhibitors. *p≤ 0.025.

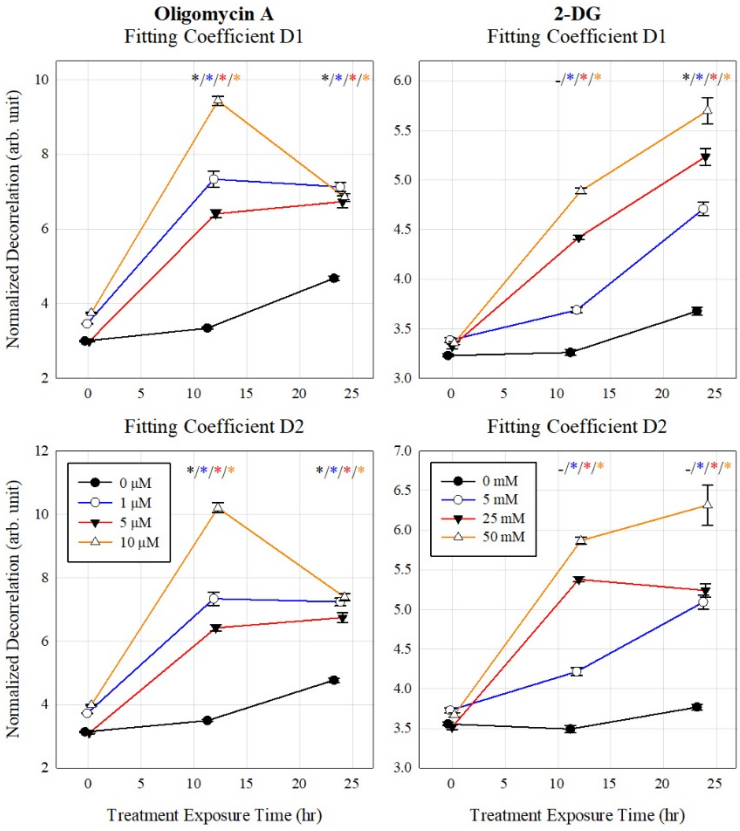


**Figure 24.** Individual spheroid fitting-based normalized decorrelation for fitting coefficient D1 and D2 over time for both metabolism inhibitors. *p≤ 0.025.

Autocorrelation-based normalized decorrelation was another investigated approach to obtaining a more true measurement of decorrelation. The decay, 2nd decay, complex shift, 2nd shift, doppler, and absolute doppler were measured as a potential means of capturing random and translational (directional) motions within the voxel. Significant time-dependent changes were observed for both the decay and complex shift metrics. The primary metrics would theoretically calculate the random motions that contributed to cellular dynamics as well as translational motion for complex shift. The secondary should account for and remove a noise component from the real motion. However, it is difficult to understand the relationship between the two and what exactly is being captured in the former calculation. As seen in **Figure 25**, the 2nd decay can be negative in practice; however, it is difficult to interpret such results at this time.

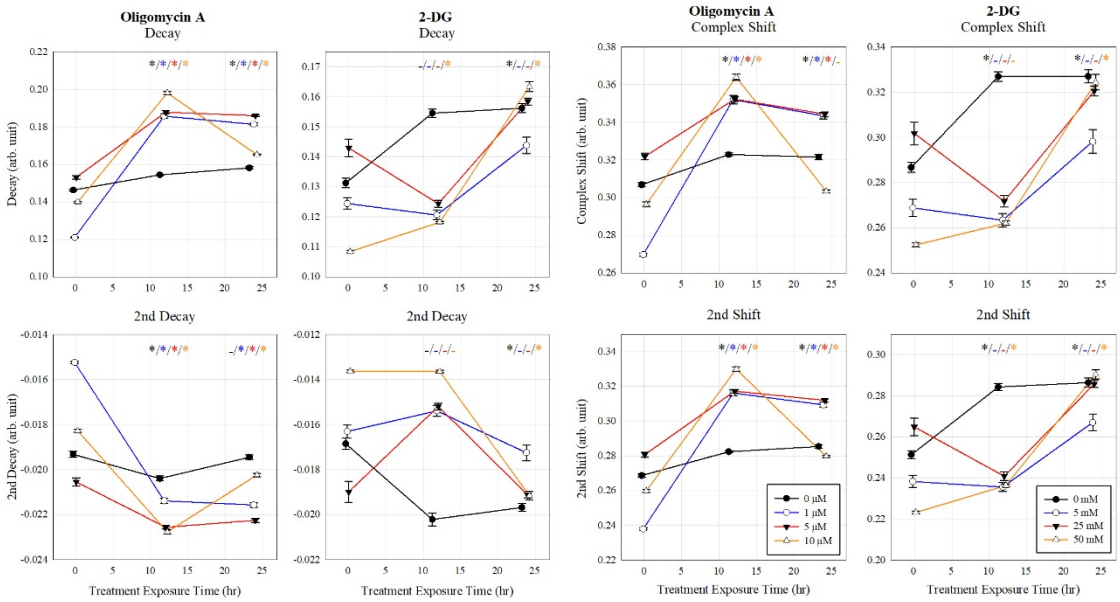


**Figure 25.** The decay and 2nd decay (left), and complex shift and 2nd shift (right) plotted over time as part of an autocorrelation-based approach to normalized decorrelation. *p≤ 0.025.

A higher doppler and absolute doppler measurement would theoretically signify more direction-consistent and translational motions, respectively. Interestingly, significant time-dependent increases and decreases in absolute doppler were observed for both drugs despite no significant findings for the doppler measurement. The relationship between doppler and absolute doppler is not fully realized at this time, as is the contribution of this autocorrelation-based metric on normalized decorrelation.

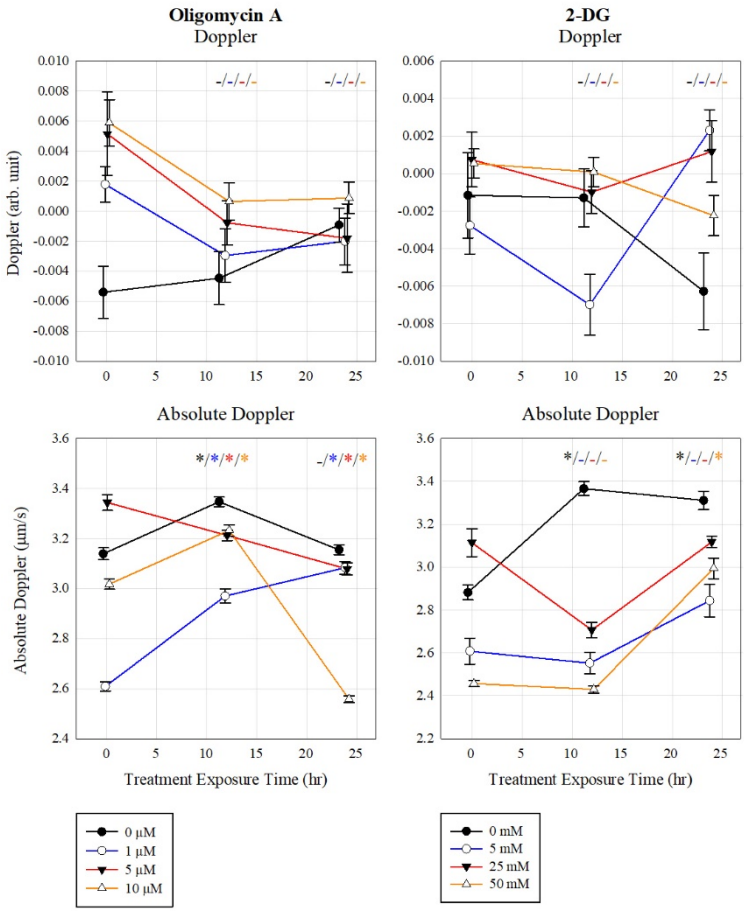


**Figure 26.** The doppler and absolute doppler plotted over time as part of an autocorrelation-based approach to normalized decorrelation. *p≤ 0.025.

### 4.3.8 Live/Dead Assay

Fluorescence images were acquired for varying concentrations of oligomycin A and 2-DG to visualize and quantify cellular viability as an end point assay after 24 hours of drug exposure. Both drugs appear to induce cell death and in a dose-dependent manner, as is apparent in the decrease in intensity of the green stain from lower to higher drug concentrations (**Fig. 23**).

Pixel analysis of the raw fluorescence images was conducted to further quantify these changes. The area and integrated density (area times the mean pixel intensity of the ROI) of live and dead cells were averaged over 10 neurospheroids. The percentage of live cells area was lower for higher concentrations of oligomycin A, and was higher for all three 2-DG treated groups

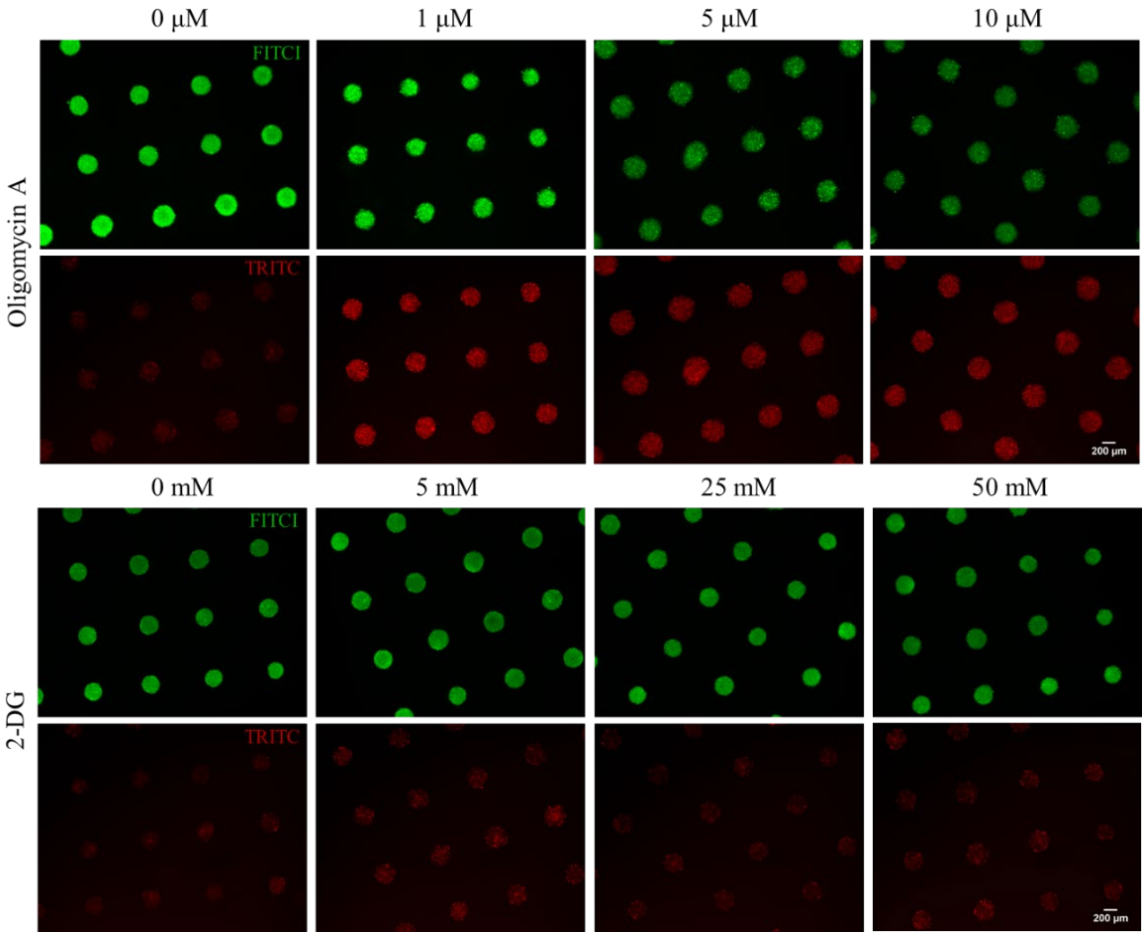


**Figure 27.** Live/dead cell viability fluorescence images acquired 24 hours after treatment exposure for varying concentrations of metabolism inhibitors. Green and red signify the live (FITC channel, calcein-AM stain) and dead cells (TRITC channel, ethidium homodimer-1), respectively.

relative to the sham (**Fig. 28**). Neurospheroids treated with oligomycin A exhibited a similar dead cell integrated density relative to sham but decreased for live cells at higher concentrations. 2-DG treated spheroids exhibited an increase in dead cell integrated density relative to sham despite a near constant live cell integrated density across all treatment groups.

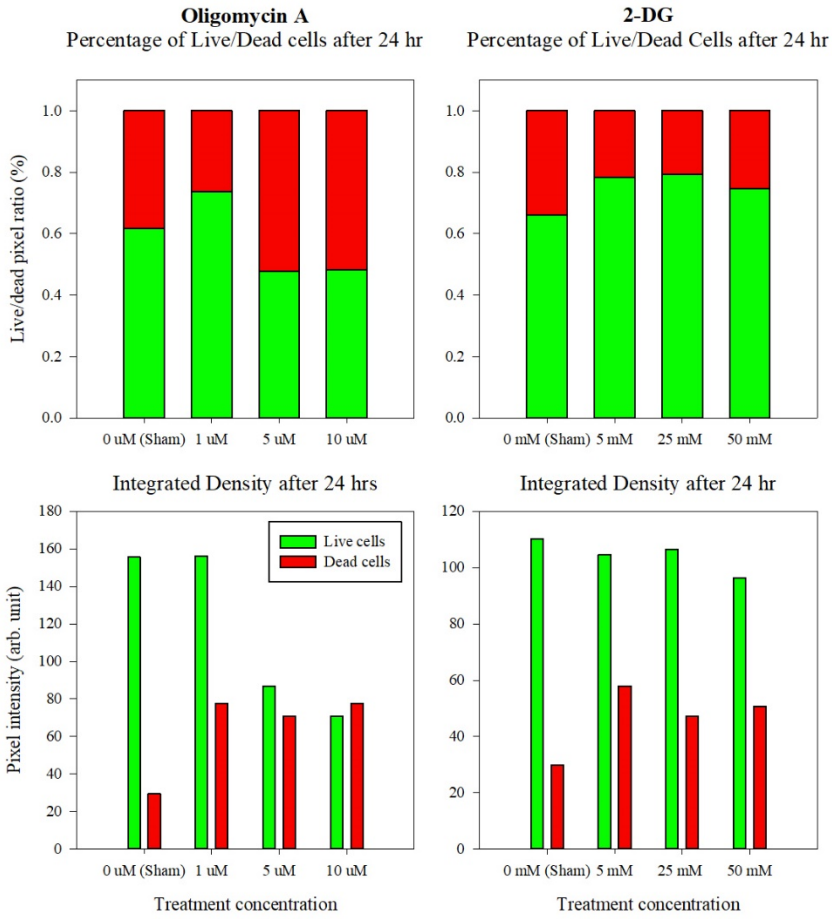


**Figure 28.** Pixel analysis of live/dead fluorescence images using area and integrated density to quantify cell viability.

### 4.3.9 2-DG depletes ATP levels

Cellular ATP levels were measured using a luminescence plate reader to determine the amount of metabolically active, live cells in a sample. Relative to the sham treatment, ATP present after 24 hours was significantly less in neurospheroids treated with 50 mM 2-DG.

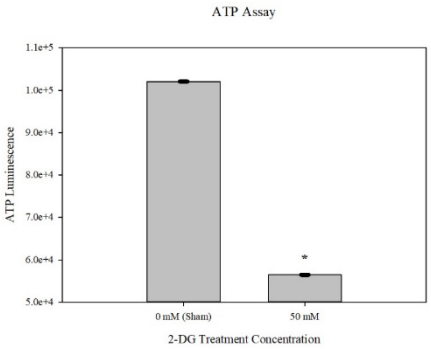


**Figure 29.** Luminescence plate reader of ATP levels for sham and 50 mM 2-DG treatment groups. *p≤ 0.05.

## 4.4 Discussion

A 3D neurospheroid model was used to assess cell viability longitudinally using a multi-metric approach coupled with parallel end point viability assays. It has been shown in neurospheroids that by DIV 7, non-functional capillaries disappear and complex neural networks with elongated neural process begin to form, and by DIV 10, the most stable tissue structure and synchronized neural activity has developed[69]. Therefore, assessment of cell viability in neurospheroids at DIV 10 was used to most aptly align with what the in vivo response may be.

Oligomycin A and 2-DG were chosen to selectively manipulate metabolism as both mitochondrial respiration and glycolysis are essential to matching the higher energy demands of cancerous cells; however, with the Warburg effect, an increase in glycolysis is observed in cancer cells regardless of oxygen availability. Regardless, the relative dependence tumors have on glycolysis and oxidative phosphorylation differs as do their responses to antimetabolites. By selectively disrupting these pathways, new approaches to cancer treatment are modulating energy production as a potential target[70]. In contriving the effects of two different metabolism inhibitors, significant time-dependent changes in viability-linked OCT metrics were detected at varying concentrations of each drug.

Assessing changes in spheroid geometry resulted in a significant increase in both volume and surface area, despite a decrease in SATVR after 24 hours for both drugs. An increase in volume and surface area may reflect spheroids becoming disaggregated as both drugs have been associated with triggering apoptosis and necrosis; however, 2-DG predominantly induces apoptotic death[71,72]. The volume and surface area appear to reach their maxima at 12 hours of exposure to oligomycin A whereas 2-DG treated groups continued to increase at 24 hours. This may be due to either a pathway-specific difference in the effect of anti-metabolism drugs or

simply because our tested concentration range of 2-DG was not as strong as that of oligomycin A. Future experiments could employ higher concentrations of 2-DG to test the latter hypothesis.

The brain as an entire organ relies almost exclusively on glucose as its main energy source, accounting for over half the entire body's resting state glucose consumption[73]. Neurons and neural function are complementary to glial cells and the overall brain yet opposite in energy supply as they rely on oxidative metabolism[74]. Since oligomycin A blocks oxidative phosphorylation, re-directed ATP production to glycolysis up-regulates the metabolic pathway. Thus, in a relatively short time scale, Oligomycin A may have had a more severe effect on neurons than glial cells. If the glial cells already predominantly utilizing glycolysis could not sufficiently compensate for the inhibition of mitochondrial respiration, the deficit may have affected the spheroid geometry and hindered proliferation. Likewise, since the spheroid geometry did not significantly change after 24 hours in the sham control, an increase in volume in the drug treated neurospheroids may not have resulted from tissue growth. Instead, it may reflect a more structurally disaggregated spheroid as a result of changes in cell viability which also may coincide with the increased SR.

SR may be a more salient measurement in assessing spheroid morphology as the roughness of the spheroid surface is not impacted by the variability in spheroid size. Both drugs significantly increased the SR of neurospheroids, aligning with what was visualized in the segmented spheroids (**Fig. 16**). In unperturbed growth conditions, the neurospheroids exhibited a spherical shape with a generally smooth surface. As tissue undergoes cell death, fragmentation and apoptotic bodies as a result of apoptosis and blebbing in necrosis may be contributing to the increase in roughness observed at the surface. If we assume the widely-accepted trend that the effect of the metabolism inhibitors should be more severe at higher concentrations and with longer exposure times, the volume and surface roughness seems to capture the same dose-

dependent effect metabolism inhibitors may have on neurospheroid geometry. Spheroid geometry metrics indicated that SR may have aligned more closely with the canonical dose and time-dependent relationship than volume (as there is no size dependence), and with an earlier onset of significant change for oligomycin A as shown in **Figure 17**, suggesting SR may be more sensitive to detecting certain processes underlying changes in viability.

Normalized to pre-treatment, different concentrations of oligomycin A and 2-DG presented varying longitudinal changes in backscattered light. Assuming that metabolic inhibition in the drug treated cohort directly triggered the cell death cascade to some degree, cells at various stages of apoptosis and necrosis warrants the differing backscattered light profiles. Neural progenitor cells treated with oligomycin A demonstrated compacted chromatin and ruptured membranes characteristic of apoptosis and necrosis[71]. Another study observed condensed chromatin and enhanced oxidative stress as a result of mitochondria damage in glioma spheroids treated with 2-DG[72]. These cytotoxic effects can alter OCT signal via changes in the morphology and/or density throughout the cell death process. However, the intensity result did not follow the expected trend that a change is greater at higher doses and after prolonged drug exposure. In the feasibility study, the mean intensity was "contaminated" by shifts in the optical focusing. Although we tried to minimize the focus shift in this neurospheroid experiment, overall the intensity was less robust than the other metrics.

The CoV was newly introduced as a sub-metric to investigate in this study. A dose-dependent increase in intensity signal heterogeneity for the oligomycin A treated cohort suggests that CoV may be more sensitive to detecting a certain process associated with cell death than the intensity. However, further investigation is fundamental prior to an appropriate, more conclusive interpretation of the CoV results.

ICM was assessed using decorrelation with three different time delays, wherein a shorter delay would theoretically detect components with faster ICM versus a longer time difference would be more sensitive to slower motions. The results of a 10 ms delay was used as there were no discernable differences between the three different delays, and showed an overall increase in OCT speckle for both drugs. Neurospheroids sensitized to cell death via metabolism inhibition may exhibit increased movement despite reduced energy supply. An increase in decorrelation could be attributed to mainly two types of increased movement, one being active (ICM) and the other passive (a result of byproducts). The latter may include the displacement of apoptotic bodies or leakage of cellular components through ruptured membranes in necrosis as well as the removal of these dysfunctional components during autophagy in order to conserve energy and reduce toxins. The former, however, is difficult to be explained regarding how the metabolism inhibition led to an increase in the active, ATP-consuming transport of intracellular organelles. There might be temporarily enhanced intracellular processes as a defense mechanism against the exogeneous metabolism inhibitors. But when considering the results that (i) the decorrelation increase was greatest in the spheroid shell, (ii) the volume significantly increased, and (iii) the surface became rougher, the increased passive movement of apoptosis/necrosis byproducts appears more reasonable. Compared to the geometry-based metrics (volume, surface area, and SR), the decorrelation change became significant earlier at 12 hours in response to 2-DG. This suggests that either the decorrelation metric is more sensitive, or the increased byproduct movement occurred earlier than the morphological change.

Newly introduced approaches to calculating normalized decorrelation were devised as potential ways of capturing true motility without the coupling effect of intensity. As such, more investigation into intra-metric relationships as well as how closely they account for the coupling effect of intensity with decorrelation are necessary prior to establishing any definite conclusions.

Based on the results presented, the fitting-based approach appeared to generate robust results, and likewise, affirmed the increase in cellular dynamics. Considering the intensity signal did not significantly increase in accordance with the increased decorrelation over time, these metrics were presumably not coupled together, further reinforcing the fitting-based normalized decorrelation results. The autocorrelation-based metrics were difficult to interpret at this time, and therefore were not as effective in this study.

In summary, OCT metrics of the whole neurospheroid indicate that the volume, surface area, and surface roughness increased after treatment of metabolism inhibitors. The decorrelation increased for both as well and was not due to the coupling effect of intensity. The multi-time difference data suggests that Oligomycin A and 2-DG impacted the neurospheroids differently as observed by the longitudinal onset of significant metric changes. When perturbed by metabolic inhibition, it is purported that the neurospheroids swelled and condensed, their surfaces became bumpier, and more fast-moving, fragmented constituents diffusing inside the spheroids increased their motions in response to changes in viability.

3D microtissue models allow for a more suitable investigation of tumor hypoxia and drug penetration relative to 2D cultures. Localized differences in metric values and longitudinal patterns were observed in the drug treated neurospheroids and may result from a drug concentration gradient as it diffuses towards the spheroid interior. Most notable were two observations: the core and shell region had the highest and lowest intensity values, respectively, and the core of 50 mM 2-DG treated spheroids exhibited a different longitudinal profile relative to other subregions. Tumor spheroids are characterized by actively dividing cells in the shell with quiescent and dead cells in the body and core[30]. Thus, the subregion difference in our data supports the technical feasibility of OCT to detect subregion-specific chemosensitivity when

applied to functional precision medicine initiatives. Furthermore, subregion metric patterns that diverge from the whole spheroid may reveal localized changes akin to what is observed in vivo.

End point assays were conducted using both drugs and confirmed a decrease in cell viability 24 hours after exposure. Upon visual inspection of live/dead fluorescence images, a higher amount of TRITC stain was apparent in the drug treated spheroids, relative to the sham (**Fig. 21**). Quantification of the live/dead stain further reinforced the decrease in viability for Oligomycin A as there was a decrease in the live cell area and integrated density for 5 μM and 10 μM treatment groups. Despite the live/dead assay showing an increased live cell pixel ratio for 2-DG treated spheroids relative to sham, the significant depletion in ATP as a result of 50 mM 2-DG may result from the concentrations not being strong enough to fully trigger death or because the inhibiting drug was specific to glial cells. Additionally, 2-DG mainly triggers apoptosis whereas the live/dead assay is sensitive to detecting necrosis and late stage apoptosis such that the dead stain may not have penetrated cells that were undergoing the earlier stages of apoptosis. Another possible explanation, as hypothesized by Khaitan et al., was that long-term glycolysis inhibition may lead to therapeutic resistance resulting from a pro-survival cell response. If 24 hours was sufficient enough to produce a pro-survival response, then this may be reflected in how 2-DG actually increased the ratio of live/dead pixels albeit with a drop in ATP levels. Of course, more biological replicates are crucial to statistically assess any significant results from the viability assays.

Compared to the feasibility study, this study has been improved upon in several ways. Firstly, the same imaging protocol was used throughout the entire OCT imaging process for all experiments, and most notably that the spheroids were refocused before every acquisition to avoid any spheroid shift bias. Secondly, the auto-segmentation feature was added to the Lee Lab code to reduce any variability associated with manually selecting spheroid ROI. The mini-

incubator housing was implemented into the neurospheroid study, which is a substantial improvement upon the heating pad and especially in allowing for a longer study time. A more methodical approach has been systemically applied to our functional precision medicine studies of cell viability, i.e. targeted drug selections were used in conjunction with parallel end point assays to leverage a more anticipated biological response. Two different drugs were used and serve as another point of comparison, and further support translational feasibility assessment. Parallel viability assays were incorporated into the study and also contributed to a greater understanding of the viability response. Lastly, several additional metrics and sub-metrics were tracked and analyzed as part of updates to the Lee Lab codes, allowing for more ways to probe the dynamics of longitudinal spheroid changes and in standard unit measurements (geometry) and in an intensity-level-independent manner (CoV and normalized decorrelation). Although additional analysis is essential in further understanding the subtleties of metric fluctuations as they relate to viability, increasing the potential parameters will only aid in further insight.

Taken altogether, several changes in metrics were observed as a result of viability changes; however, not all of the longitudinal trends were fully palatable at this point. The metabolism inhibitor analysis using neurospheroids only took into consideration a single biological replicate for each drug and requires more experimentation for a more thorough, valid analysis. *Unfortunately, our planned experiments with more biological replicates have been suspended by the university-wide lab shutdown due to COVID-19. As this study is still ongoing, those experiments will be resumed when COVID-19 is cleared and university research recommences.*

## 4.5 Conclusion

A functional imaging approach was used to assess changes in viability as a result of metabolic inhibition. Longitudinal, multi-metric tracking revealed significant time-dependent

changes in neurospheroids, resulting in a differentiated viability response between the two antimetabolites. Overall, an increase in spheroid surface roughness and decorrelation was observed in all treated groups, mostly in a canonical dose-time-response manner, but with certain distinction being observed between the two drugs. As oligomycin A and 2-DG both inhibit cellular metabolism but rely on different pathways, the observed distinction supports the technical feasibility of our multi-metric OCT approach being sensitive enough to distinguish between the separate pathways. End point viability assays confirmed a decrease in live cell area pixel ratio and cellular ATP levels for oligomycin A and 2-DG, respectively. Motivated by functional precision medicine, future studies using optical techniques could continue to refine 3D viability imaging, ultimately allowing for the generation of longitudinal dose response curves using PDOs to discern optimal cancer treatments tailored to the individual patient.

## References


[1] Bray F, Ferlay J, Soerjomataram I, Siegel RL, Torre LA, Jemal A. Global cancer statistics 2018: GLOBOCAN estimates of incidence and mortality worldwide for 36 cancers in 185 countries. *CA: A Cancer Journal for Clinicians*. 2018;68(6):394-424.

[2] American Cancer Society. Global Cancer Facts & Figures 4th Edition. Atlanta: American Cancer Society; 2018. cancer.org/content/dam/cancer-org/research/cancer-facts-and-statistics/global-cancer-facts-and-figures/global-cancer-facts-and-figures-4th-edition.pdf

[3] Li MC, Hertz R, Spencer DB. Effect of Methotrexate Therapy upon Choriocarcinoma and Chorioadenoma. *Proceedings of the Society for Experimental Biology and Medicine.* 1956;93(2):361-366.

[4] Sun J, Wei Q, Zhou Y, Wang J, Liu Q, Xu H. A systematic analysis of FDA-approved anticancer drugs. *BMC Systems Biology*. 2017;11(Suppl5):27-43.

[5] Morgan G, Ward R, Barton M. The contribution of cytotoxic chemotherapy to 5-year survival in adult malignancies. *Clinical Oncology*. 2004;16(8):549-60.

[6] Samson DJ, Seidenfeld J, Ziegler K, Aronson N. Chemotherapy Sensitivity and Resistance Assays: A Systemic Review. *Journal of Clinical Oncology*. 2004;22(17):3618-30.

[7] Schrag D, et al. American Society of Clinical Oncology Technology Assessment: chemotherapy sensitivity and resistance assays. *Journal of Clinical Oncology*. 2004;22(17):3631-3638.

[8] Burstein HJ, et al. American Society of Clinical Oncology Clinical Practice Guideline Update on the Use of Chemotherapy Sensitivity and Resistance Assays. *Journal of Clinical Oncology.* 2011;29(24):3328-30.

[9] "Fact Sheet: President Obama's Precision Medicine Initiative." *National Archives and Records Administration*, 30 Jan. 2015, obamawhitehouse.archives.gov/the-press-office/2015/01/30/fact-sheet-president-obama-s-precision-medicine-initiative.

[10] Zhang XD. Precision Medicine, Personalized Medicine, Omics and Big Data: Concepts and Relationships. *Pharmacogenomics and Pharmacoproteomics*. 2015;6(1).

[11] Mauro MJ, O'Dwyer ME, Druker BJ. STI571, a tyrosine kinase inhibitor for the treatment of chronic myelogenous leukemia: validating the promise of molecularly targeted therapy. *Cancer Chemotherapy and Pharmacology.* 2001;48(Suppl1):S77-S78.

[12] Dagher R, et al. Approval summary: imatinib mesylate in the treatment of metastatic and/or unresectable malignant gastrointestinal stromal tumors. *Clinical Cancer Research.* 2002;8(10):3034-38.

[13] Dienstmann R, Jang IS, Bot B, Friend S, Guinney J. Database of genomic biomarkers for cancer drugs and clinical targetability in solid tumors. *Cancer Discovery*. 2015;5(2):118-23.

[14] Roper N, Stensland KD, Hendricks R, Galsky MD. The landscape of precision cancer medicine clinical trials in the United States. *Cancer Treatment Reviews.* 2015;41(5):385-90.

[15] Prasad V, Fojo T, Brada M. Precision oncology: origins, optimism, and potential. The *Lancet Oncology.* 2016;17(2):PE81-PE86.

[16] Van't Veer LJ, et al. Gene expression profiling predicts clinical outcome of breast cancer. *Nature.* 2001;415(6871):530-6.

[17] Paez JG, et al. EGFR mutations in lung cancer: correlation with clinical response to gefitinib therapy. *Science.* 2004;304(5676):1497-500.

[18] Hauschild A, et al. Dabrafenib in BRAF-mutated metastatic melanoma: a multicentre, open-label, phase 3 randomised controlled trial. *The Lancet.* 2012;380(9839):358-65.

[19] Perez EA, et al. Four-Year Follow-Up of Trastuzumab Plus Adjuvant Chemotherapy for Operable Human Epidermal Growth Factor Receptor 2–Positive Breast Cancer: Joint Analysis of Data From NCCTG N9831 and NSABP B-31. *Journal of Clinical Oncology.* 2011;29(25):3366-73.

[20] Thorlacius S, et al. A single BRCA2 mutation in male and female breast cancer families from Iceland with varied cancer phenotypes. *Nature Genetics.* 1996;13(1):117-19.

[21] Letai A. Functional precision cancer medicine—moving beyond pure genomics. *Nature Medicine.* 2017;23(9):1028-35.

[22] Le Tourneau C, et al. Molecularly targeted therapy based on tumour molecular profiling versus conventional therapy for advanced cancer (SHIVA): a multicentre, open-label, proof-of-concept, randomised, controlled phase 2 trial. *The Lancet Oncology.* 2015;16(13):1324-34.

[23] West M, Ginsburg GS, Huang AT, Nevins JR. Embracing the complexity of genomic data for personalized medicine. *Genome Research.* 2006;16(5):559-66.

[24] Freimuth RR, et al. Implementing Genomic Clinical Decision Support for Drug-Based Precision Medicine. *CPT: Pharmacometrics & Systems Pharmacology.* 2017;6(3):153-5.

[25] Tsherniak A, et al. Defining a cancer dependency map. *Cell*. 2017;170(3):564-76.

[26] Pauli C, et al. Personalized In Vitro and In Vivo Cancer Models to Guide Precision Medicine. *Cancer Discovery*. 2017;7(5):462-77.

[27] He L, et al. Patient-Customized Drug Combination Prediction and Testing for T-cell Prolymphocytic Leukemia Patients. *Cancer Research.* 2018;78(9):2407-18.

[28] Duval K, et al. Modeling Physiological Events in 2D vs. 3D Cell Culture. *Physiology*. 2017;32(4):266-77.

[29] Phan N, et al. A simple high-throughput approach identifies actionable drug sensitivities in patient-derived tumor organoids. *Communications Biology*. 2019;2(78).

[30] Zanoni M, et al. 3D tumor spheroid models for in vitro therapeutic screening: a systematic approach to enhance the biological relevance of data obtained. *Scientific Reports*. 2016;6(19103).

[31] Delphine A, Burckel H, Josset E, Noel G. Three-Dimensional Cell Culture: A Breakthrough in Vivo. *International Journal of Molecular Sciences*. 2015;16(3):5517-27.

[32] Ghosh S, et al. Three-dimensional culture of melanoma cells profoundly affects gene expression profile: a high density oligonucleotide array study. *Journal of Cellular Physiology*. 2005;204(2):522-31.

[33] Yang H, Sun L, Liu M, Mao Y. Patient-derived organoids: a promising model for personalized cancer treatment. *Gastroenterology Report*. 2018;6(4):243-45.

[34] Vlachogiannis G, et al. Patient-derived organoids model treatment response of metastatic gastrointestinal cancers. *Science*. 2018;359(6378):920-6.

[35] Kelm JM, Timmins NE, Brown CJ, Fussenegger M, Nielsen LK. Method for generation of homogeneous multicellular tumor spheroids applicable to a wide variety of cell types. *Biotechnology and Bioengineering*. 2003;83(2):173-80.

[36] Sorenson AG, et al. Comparison of diameter and perimeter methods for tumor volume calculation. *Journal of Clinical Oncology*. 2001;19(2):551-7.

[37] Von Hoff DD, et al. A Southwest Oncology Group study on the use of a human tumor cloning assay for predicting response in patients with ovarian cancer. *Cancer*. 1991;67(1):20-7.

[38] Mehta G, Hsiao AY, Ingram M, Luker GD, Takayama S. Opportunities and Challenges for use of Tumor Spheroids as Models to Test Drug Delivery and Efficacy. *Journal of Controlled Release*. 2013;164(2):192-204.

[39] Piccinini F, Tesei A, Arienti C, Bevilacqua A. Cell Counting and Viability Assessment of 2D and 3D Cell Cultures: Expected Reliability of the Trypan Blue Assay. *Biological Procedures Online*. 2019;19(8).

[40] Bouma BE, et al. Evaluation of intracoronary stenting by intravascular optical coherence tomography. *Interventional Cardiology and Surgery*. 2002;89(3):317-20.

[41] Isenberg G, et al. Accuracy of endoscopic optical coherence tomography in the detection of dysplasia in Barrett's esophagus: a prospective, double-blinded study. *Gastrointestinal Endoscopy*. 2005;62(6):825-31.

[42] Huang D, et al. Optical coherence tomography. *Science*. 1991;254(5035):1178-81.

[43] Li B, et al. Impact of temporal resolution on estimating capillary RBC-flux with optical coherence tomography. *Journal of Biomedical Optics*. 2017;22(1).

[44] Gabriele ML, et al. Optical Coherence Tomography: History, Current Status, and Laboratory Work. *Investigate Ophthalmology & Visual Science.* 2011;52(5):2425-2436.

[45] Ross RJ, Thompson JS, Kim K, Bailey RA. Nuclear magnetic resonance imaging and evaluation of human breast tissue: preliminary clinical trials. *Radiology*. 1982;143(1):195-205.
[46] Fass L. Imaging and cancer: a review. *Molecular Oncology.* 2008;2(2):115-52.

[47] Wang, LV, Wu H. Biomedical Optics: Principles and Imaging. United States: Wiley. 2012.

[48] Van der Meek FJ, Faber DJ, Aalders MCG, Poot AA, Vermes I. Apoptosis- and necrosis-induced changes in light attenuation measured by optical coherence tomography. *Lasers in Medical Science.* 2010;25(2):259-67.

[49] Evans CL, Rizvi I, Hasan T, de Boer JF. In vitro ovarian tumor growth and treatment response dynamics visualized with time-lapse OCT imaging. *Optics Express.* 2010;17(11):8892-906.

[50] Duprez L, Wirawan E, Berghe TV, Vandenabeele P. Major cell death pathways at a glance. *Microbes and Infection*. 2009;11(13):1050-62.

[51] Jeong K, Turek JJ, Nolte DD. Volumetric motility-contrast imaging of tissue response to cytoskeletal anti-cancer drugs. *Optics Express*. 2007;15(21):14057-64.

[52] Farhat G, Czarnota GJ, Kolios MC, Yang VXD, Miriampillai A. Detecting apoptosis using dynamic light scattering with optical coherence tomography. *Journal of Biomedical Optics.* 2011;16(7).

[53] Farhat G, Yang VXD, Kolios MC, Czarnota GJ. Cell death monitoring using quantitative optical coherence tomography methods. *Biomedical Applications of Light Scattering V*. 2011;7097.

[54] Farhat G, Mariampillai A, Yang VXD, Czarnota GJ, Kolios MC. Optical coherence tomography speckle decorrelation for detecting cell death. *Biomedical Applications of Light Scattering V.* 2011;790710.

[55] Bagnaninchi PO, Drummond N, Holmes C, Daoud J, Tabrizian M. Two-dimensional and three-dimensional viability measurements of adult stem cells with optical coherence phase microscopy. *Journal of Biomedical Optics.* 2011;16(8):086003.

[56] Jung Y, Klein OJ, Wang H, Evans CL. Longitudinal, label-free, quantitative tracking of cell death and viability in a 3D tumor model with OCT. *Scientific Reports*. 2016;6:27017.

[57] Huang Y, et al. Optical Coherence Tomography Detects Necrotic Regions and Volumetrically Quantifies Multicellular Tumor Spheroids. *Cancer Research.* 2017;77(21):6011-20.

[58] Lee J, Wu W, Jiang JY, Zhu B, Boas DA. Dynamic light scattering optical coherence tomography. *Optics Express*. 2012;20(20):22262-77.

[59] Lee J, et al. Quantitative imaging of cerebral blood flow velocity and intracellular motility using dynamic light scattering–optical coherence tomography. *Journal of Cerebral Blood Flow & Metabolism.* 2013;33(6):819-25.

[60] Yang L, Yu X, Fuller AM, Troester MA, Oldenburg AL. Characterizing optical coherence tomography speckle fluctuation spectra of mammary organoids during suppression of intracellular motility. *Quantitative Imaging in Medicine and Surgery*. 2019.

[61] Yu X, Fuller AM, Blackmon R, Troester MA, Oldenburg AL. Quantification of the effects of toxicants on the intracellular kinetic energy and cross-sectional area of mammary epithelial organoids by OCT fluctuation spectroscopy. *Toxicology Sciences*. 2018;162(1):234-40.

[62] Warburg O. On the origin of cancer cells. *Science.* 1956;123(3191):309-14.

[63] Effect of alcohol on cellular membranes. *Annals of Emergency Medicine.* 1986;15(9):1013-8.

[64]Baker RC, Kramer RE. Cytotoxicity of short chain alcohols. *Annual Review of Pharmacology and Toxicology*. 1999;39:127-50.

[65] Castilla R, Gonzalez R, Fouad D, Fraga E, Muntane J. Dual effect of ethanol on cell death in primary culture of human and rat hepatocytes. *Alcohol and Alcoholism*. 2004;39(4):290-6.

[66] Castaneda F, Kinne RK. Short exposure to millimolar concentrations of ethanol induces apoptotic cell death in multicellular HepG2 spheroids. *Journal of Cancer Research and Clinical Oncology.* 2000;126(6):305-10.

[67] Kurose I, et al. Oxidative Stress-Mediated Apoptosis of Hepatocytes Exposed to Acute Ethanol Intoxication. *Hepatology.* 1997;25(2):368-78.

[68] Su LJ, et al. Reactive Oxygen Species-Induced Lipid Peroxidation in Apoptosis, Autophagy, and Ferroptosis. *Oxidative Medicine and Cellular Longevity.* 2019;2019:1-13.

[69] Dingle et al. Three-Dimensional Neural Spheroid Culture: An In Vitro Model for Cortical Studies. *Tissue Engineering: Part C, Methods.* 2015;21(12):1274-83.

[70] Russell S, Wojtkowiak J, Neilson, Gillies RJ. Metabolic profiling of healthy and cancerous tissues in 2D and 3D. *Scientific Reports*. 2017;7(15285).

[71] Lee Y, et al. Selective impairment on the proliferation of neural progenitor cells by oxidative phosphorylation disruption. *Neuroscience Letters*. 2013;535:134-9.

[72] Khaitan D, Chandna S, Dwarakanath SB. Short-term exposure of multicellular tumor spheroids of a human glioma cell line to the glycolytic inhibitor 2-deoxy-D-glucose is more toxic than continuous exposure. *Journal of Cancer Research Therapeutics.* 2009;5 Suppl 1: S67-73.

[73] Berg JM, Tymoczko JL, Stryer L. Biochemistry. 5th edition. New York: W H Freeman; 2002. Section 30.2, Each Organ Has a Unique Metabolic Profile. Available from: https://www.ncbi.nlm.nih.gov/books/NBK22436/

[74] Watts ME, Pocock R, Claudianos C. Brain Energy and Oxygen Metabolism: Emerging Role in Normal Function and Disease. *Frontiers in Molecular Neuroscience*. 2018;11.